

https://dspace.org/

An AB initio study of the guest atom rattling in thermoelectric Sn clathrates

Egbele, Peter Odion

2018

https://hdl.handle.net/10539/27217

Egbele, Peter Odion (2018) An AB initio study of the guest atom rattling in thermoelectric Sn clathrates, University of the Witwatersrand, Johannesburg, <http://hdl.handle.net/10539/27217>

Downloaded from a DSpace repository. https://dspace.org/



AN AB INITIO STUDY OF THE GUEST ATOM RATTLING IN THERMOELECTRIC Sn CLATHRATES

Presented by: PETER ODION EGBELE
(892222)

Supervised by: Prof Daniel P Joubert
Dr Elvis Shoko

Thesis submitted to the Faculty of Science
University of the Witwatersrand,
in fulfillment of the requirements for
the degree of Doctor of Philosophy (PhD)
School of physics,
University of the Witwatersrand,

Johannesburg.

2018

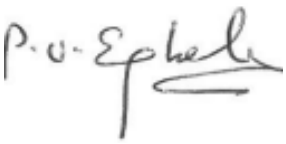
Abstract

Semiconducting compounds with a clathrate hydrate-type I crystal structure are of growing interest as potential thermoelectric materials. The need to maximize the potential of these materials has informed increasing research to gain understanding on what is responsible for the low thermal conductivity in these compounds. The lattice thermal conductivity of binary type-I Sn clathrates, $Cs_8Sn_{44}\square_2$, $Rb_8Sn_{44}\square_2$ and $K_8Sn_{44}\square_2$ was investigated using *ab initio* calculations based on density functional theory DFT. It is confirmed that vacancy formation in the stoichiometric compounds stabilizes the structure. In all the compounds the guest atoms interact with the framework and cannot be treated as weakly acting 'rattlers'. Using a fictitious Sn_{46} framework, it was shown that in the binary compounds the acoustic modes are suppressed to lower frequencies. This leads to a slight (35%) reduction of phonon group velocities in the acoustic modes compared to the framework. However the major cause of the reduction of the lattice thermal conductivities compared to a Sn_{46} framework, can be traced to the increase in the phonon-phonon scattering interactions which reduce the phonon lifetimes drastically from (175 ps to 25 ps). The phonon life times decrease over the whole frequency range and the relative life times decrease from $Cs_8Sn_{44}\square_2$ to $Rb_8Sn_{44}\square_2$ to $K_8Sn_{44}\square_2$. The relative thermal conductivities scale in the reverse order.

Despite the order of the values of the relative thermal conductivities, $Cs_8Sn_{44}\square_2$ is predicted to have the largest figure of merit, greater than 2 at room temperature.

DECLARATION

I declare that this Dissertation is my own, unaided work. Any work done by others has been acknowledged and referenced accordingly. It is being submitted for the Degree of Doctor of Philosophy at the University of the Witwatersrand, Johannesburg. It has not been submitted before for any degree or examination at any other University.



(Signature of the candidate)

27 July
_____day of _____2018

Acknowledgements

I would like to thank God the Almighty (The Lord Jesus Christ) for everything that he has done in my life and who made everything possible.

My profound gratitude goes to my supervisor, Prof. Daniel P. Joubert for his guidance, encouragement and support throughout this project. My co-supervisor, Dr Elvis Shoko for not giving up on me.

I am highly indebted to my wife and children for their support and encouragements.

I would like to thank Pastor and Pastor(Mrs) Obokhai of RCCG Ambassadors Church, South Africa for prayers and financial support.

I would like to thank Drs' Abdusallam, Dongho, and George Manyali who started me of in DFT calculations and confussion.

I would also like to acknowledge the financial support provided by the University of the Witwatersrand, Johannesburg South Africa.

I acknowledge the Centre for High Performance Computing (CHPC) for providing the computational resources to perform some of the calculations in this dissertation.

I would not fail to acknowledge my colleagues Marriam Chepkwoech, Elkana Rugut, Ibrahim Alli, Mahmoud Ahmed, Kossi Amouzovi, Abdu Barde, Aya, and Ali for all the wonderful discussions and sharing of thoughts.

Finally, I thank my families and inlaws, and Church and friends in South Africa.

Contents

Abstract i

Declaration ii

Acknowledgements iii

1 Introduction 1

1.1 Motivation . . . 5

1.2 Aim and Dissertation outline . . . 6

2 Literature Review 7

2.1 Clathrates as cage materials . . . 7

2.2 Thermoelectricity and Power generation in type-I Clathrates . . . 11

3 Theoretical Framework 13

3.1 Equation of state . . . 13

3.2 Cage size and vacancy formation . . . 14

3.3 Cohesive energy . . . 15

3.4 *Ab initio* Molecular Dynamics . . . 15

3.5 Transport Theory . . . 17

3.6 Thermodynamic Properties . . . 17

4 Computational Details 20

4.1 Geometry Optimization and Structural Properties . . . 20

4.2 Electronic Density of States . . . 21

4.3 Electronic Bandgap with mBJ Functional . . . 22

4.4 Lattice Dynamics . . . 22

4.5 Molecular Dynamics Simulation . . . 23

5 Results and Discussion **25**

5.1 Equilibrium and Structural properties . . . 26
5.2 Result for $A_8Sn_{44}\square_2$ . . . 27
5.3 Volume and Vacancy Formation . . . 29
5.4 Phonon Bandstructure and Density of States . . . 31
5.5 Grüneisen parameters . . . 44
5.6 Electronic Structure . . . 45
5.7 Anisotropic Behaviour and Effective Carrier Masses . . . 52
5.8 Seebeck Coefficient . . . 54
5.9 Lattice Thermal Conductivity . . . 57
5.10 Electronic Thermal Conductivity . . . 66
5.11 Thermoelectric Power Factor . . . 68
5.12 *Figure of Merit* . . . 70

6 Summary and Conclusion **73**

A Density Functional Theory **75**

B VASP **87**

C Boltzmann's Equation for Transport **91**

D Phonon Calculations **93**

References **107**

List of Figures

1.1 A diagramatic illustration of Peltier effect generator and Seebeck effect generator. 2

1.2 Type-I clathrates polyhedra. 5

2.1 Source Myles [1]) Type-I clathrates polyhedra showing 20- and 24- atom cages with guest atoms 8

4.1 Special K-path considered [2] 23

5.1 Structure showing covalently-bonded framework atoms forming a polyhedra with regular or distorted pentagonal and hexagonal faces, housing guest atoms (a) A_8Sn_{46} (A = Cs, Rb and K) (b) $A_8Sn_{44}\square_2$ (A = Cs, Rb and K) (Green spheres = Cs, Rb or K atoms, small silvery spheres = Sn atoms). 29

5.2 Source: [3] (a)Tetrahedral bonds of framework atoms, and (b) guests in dodecahedral and tetrakaidecahedral cages for type-I clathrates. 30

5.3 Plots of (left) Calculated phonon band dispersion for $K_8Sn_{44}\square_2$ along high symmetry directions (refer to the Brillouin zone in Figure (4.1) (right) Guest atom (K) contribution to the total density of states TDOS. 31

5.4 Plots of (left) Calculated phonon band dispersion for $Rb_8Sn_{44}\square_2$ along high symmetry directions (refer to the Brillouin zone in Figure (4.1)) (right) Guest atom (Rb) contribution to the total density of states TDOS. 32

5.5 Plots of (left) Calculated phonon band dispersion for $Cs_8Sn_{44}\square_2$ along high symmetry directions (refer to the Brillouin zone in Figure (4.1).) (right) Guest atom (Cs) contribution to the total density of states TDOS. 33

5.6 Projected density of states for the stoichiometric system K_8Sn_{46} (a) and for the vacancy system $K_8Sn_{44}\square_2$ (b). Densities of states are projected onto the atoms at the two inequivalent K guest atom sites and onto the three inequivalent Sn sites for K_8Sn_{46}, and onto the corresponding atoms sites for $K_8Sn_{44}\square_2$. 34

5.7 Projected density of states for the stoichiometric system Rb_8Sn_{46} (a) and for the vacancy system $Rb_8Sn_{44}\square_2$ (b). Densities of states are projected onto the atoms at the two inequivalent Rb guest atom sites and onto the three inequivalent Sn sites for Rb_8Sn_{46}, and onto the corresponding atoms sites for $Rb_8Sn_{44}\square_2$. 34

5.8 Projected density of states for the stoichiometric system Cs_8Sn_{46} (a) and for the vacancy system $Cs_8Sn_{44}\square_2$ (b). Densities of states are projected onto the atoms at the two inequivalent Cs guest atom sites and onto the three inequivalent Sn sites for Cs_8Sn_{46}, and onto the corresponding atoms sites for $Cs_8Sn_{44}\square_2$. 35

5.9 Cumulated projected density of states for the fictitious Sn_{46} framework. 36

5.10 Relaxed atomic configuration around the vacancy created by removing a Sn atom from a Wyckoff c site in the lower hexagonal ring in Figure (5.2). The small dark sphere indicates the approximate position where the Sn framework atom was removed. All atoms within a radius of about 5 Å from the vacancy centre are shown. 38

5.11 $K_8Sn_{44}\square_2$: Projected density of states for atoms near the first vacancy. (a) Individual atoms. (b) Cumulative projected density of states for K and Sn atoms near the vacancy. 39

5.12 $Rb_8Sn_{44}\square_2$: Projected density of states for atoms near the first vacancy. (a) Individual atoms. (b) Cumulative projected density of states for Rb and Sn atoms near the vacancy. 39

5.13 $Cs_8Sn_{44}\square_2$: Projected density of states for atoms near the first vacancy. (a) Individual atoms. (b) Cumulative projected density of states for Cs and Sn atoms near the vacancy. 40

5.14 Relaxed atomic configuration around the vacancy created by removing a Sn atom from a Wyckoff c site in the middle hexagonal ring in Figure (5.2). The small dark sphere indicates the approximate position where the Sn framework atom was removed. All atoms within a radius of about 5 Åfrom the vacancy centre are shown. 40

5.15 MD phonon spectra for K_8Sn_{44}. (a) Three main peaks located at about 4.7, 7.5, and 11.2 meV showing some evidence of splitting in the lower peak. (b) Site spectra of the K atoms at a- and d-sites, showing a strong peak of 11.3 meV at the a-site and two main peaks of 4.7 and 7.5 meV at the d-site. 41

5.16 Directional site spectra for K_8Sn_{44}. 42

5.17 Estimated potential mean force at the a- and d-sites. 43

5.18 Plot of the Gruneisen parameter with respect to frequency for (a)K in $K_8Sn_{44}\square_2$ (b) Rb in $Rb_8Sn_{44}\square_2$ and (c) Cs in $Cs_8Sn_{44}\square_2$. 44

5.19 Band structure from a conventional first-principles calculations for $K_8Sn_{44}\square_2$ along different high-symmetry directions (refer to the Brillouin zone in Figure (4.1)). 46

5.20 Band structure from a conventional first-principles calculations for $Rb_8Sn_{44}\square_2$ along different high-symmetry directions (refer to the Brillouin zone in Figure (4.1)). 46

5.21 Band structure from a conventional first-principles calculations for $Cs_8Sn_{44}\square_2$ along different high-symmetry directions (refer to the Brillouin zone in Figure (4.1). 47

5.22 The total (TDOS) and projected density of states show the contribution of guest atoms Cs in $Cs_8Sn_{44}\square_2$. The origin of energy is the Fermi energy which is shown by a *thin dot line i.e* top of VB is set to zero. 48

5.23 The total (TDOS) and projected density of state show the contribution of guest atoms Rb in $Rb_8Sn_{44}\square_2$. The origin of energy is the Fermi energy which is shown by a *thin dot line i.e* top of VB is set to zero. 49

5.24 The total (TDOS) and projected density of states show the contribution of guest atoms K in $K_8Sn_{44}\square_2$. The origin of energy is the Fermi energy which is shown by a *thin dot line i.e* top of VB is set to zero. 49

5.25 Fermi surface plot for $K_8Sn_{44}\square_2$ at an isosurface value of 0.1 eV and 0.2 eV above (below) conduction (valence) band edge. 50

5.26 Fermi surface plot for $Rb_8Sn_{44}\square_2$ at an isosurface value of 0.20 eV and 0.28 eV above (below) conduction (valence) band edge. 51

5.27 Fermi surface plot for $Rb_8Sn_{44}\square_2$ at an isosurface value of 0.17 eV and 0.23 eV above (below) conduction (valence) band edge. 52

5.28 Seebeck coefficient for $K_8Sn_{44}\square_2$. 55

5.29 Seebeck coefficient for $Rb_8Sn_{44}\square_2$. 55

5.30 Seebeck coefficient for $Cs_8Sn_{44}\square_2$. 56

5.31 Average cumulative lattice thermal conductivity for $A_8Sn_{44}\square_2$, (A = Cs, Rb, K) and the fictitious framework Sn_{46} structure as a function of frequency at 300 K. 58

5.32 The magnitude of the group velocities, v_g, for $A_8Sn_{44}\square_2$, (A = Cs, Rb, K) and the framework Sn_{46} as a function of frequency. 59

5.33 Modal relaxation times, τ_λ, for $A_8Sn_{44}\square_2$, (A = Cs, Rb, K) and the framework Sn_{46} as a function of frequency at 300 K. 61

5.34 Plots of lattice thermal conductivity κ_l as a function of frequency at 300 K indicating major contribution to κ_l between 0 THz and 0.7 THz for (a) $K_8Sn_{44}\square_2$ (b) κ_l as a function of temperature with insert showing materials anisotropic factor plotted against temperature displaying the region of stability. 63

5.35 Plots of lattice thermal conductivity κ_l as a function of frequency at 300 K indicating major contribution to κ_l between 0 THz and 0.5 THz for (a) $Rb_8Sn_{44}\square_2$ (b) κ_l as a function of temperature with insert showing materials anisotropic factor plotted against temperature displaying the region of stability. 63

5.36 Plots of lattice thermal conductivity κ_l as a function of frequency at 300 K indicating major contribution to κ_l between 0 - 0.5 THz and 1 - 0.5 THz for (a) $Cs_8Sn_{44}\square_2$ (b) κ_l as a function of temperature with insert showing materials anisotropic factor plotted against temperature displaying the region of stability. 64

5.37 Plots of derivative of lattice thermal conductivity vibrations superimposed on the pDOS for (a)$K_8Sn_{44}\square_2$ (b) $Rb_8Sn_{44}\square_2$ as a function of frequency. 65

5.38 Plots of derivative of lattice thermal conductivity vibrations superimposed on the pDOS for $Cs_8Sn_{44}\square_2$ as a function of frequency. 65

5.39 κ_e and σ plotted as functions of the chemical potential for different temperatures. The origin of μ shifted to zero 66

5.40 κ_e and σ plotted as functions of the chemical potential for different temperatures. The origin of μ shifted to zero 67

5.41 κ_e and σ plotted as functions of the chemical potential for different temperatures. The origin of μ shifted to zero 67

5.42 Variation of Power factor with respect to chemical potential at the top of the valence band as a function of temperature for $K_8Sn_{44}\square_2$. The origin of μ shifted to zero 68

5.43 Variation of Power factor with respect to chemical potential at the top of the valence band as a function of temperature for $Rb_8Sn_{44}\square_2$. The origin of μ shifted to zero 69

5.44 Variation of Power factor with respect to chemical potential at the top of the valence band as a function of temperature for $Cs_8Sn_{44}\square_2$. The origin of μ shifted to zero 69

5.45 Plots of figure of merit (ZT) as a function of chemical potential for $K_8Sn_{44}\square_2$ showing anisotropic behaviour. The origin of μ shifted to zero 70

5.46 Plots of figure of merit (ZT) as a function of chemical potential for $Rb_8Sn_{44}\square_2$ showing anisotropic behaviour. The origin of μ shifted to zero 71

5.47 Plots of figure of merit (ZT) as a function of chemical potential showing anisotropic behaviour. The origin of μ shifted to zero 71

5.48 Plots of Calculated ZT for Cs_8Sn_{44}, Rb_8Sn_{44} and K_8Sn_{44} at varying temperatures for (a)n-type x-direction (b)n-type y-direction (c)p-type x-direction (d)p-type y-direction . . 72

D.1 Work flow of phonon calculation [4] 94

List of Tables

2.1 ZT values of some type-I clathrates. 11

5.1 Structural parameters for the cubic A_8Sn_{46} compounds using different exchange-correlation functionals. 27

5.2 Structural parameters for the cubic $A_8Sn_{44}\square_2$ compounds using different exchange correlation functionals. 29

5.3 Calculated Grüneisen parameter at different temperatures. 45

5.4 Calculated m_e^* and m_h^* effective masses in electron rest-mass units in the x-, y- and z-directions for $A_8Sn_{44}\square_2$. 54

5.5 Extracted Seebeck Coefficient (S) for chemical potential at the top of the valence band of 5.62, 5.08 and 5.33 eV for $Cs_8Sn_{44}\square_2$, $Rb_8Sn_{44}\square_2$ and $K_8Sn_{44}\square_2$ respectively at calculated temperatures in the x- and y-directions. 57

5.6 Extracted Seebeck Coefficient (S) for a chemical potential at the bottom of the conduction band of 5.62, 5.08 and 5.33 eV for $Cs_8Sn_{44}\square_2$, $Rb_8Sn_{44}\square_2$ and $K_8Sn_{44}\square_2$ respectively at calculated temperatures in the x- and y-directions. 57

5.7 Dimensionless figure of merit (ZT) calculated at varying temperatures for n-type in the x- and y-directions for the three compounds 71

1

Introduction

Of interest in the past decades has been the need for a device or material that can be used to capture and convert waste heat to useful energy. Materials that are capable of converting heat energy into electrical energy are called thermoelectric (TE) materials. The phenomenon by which either a temperature difference creates an electric potential or an electric potential creates a temperature difference is called the thermoelectric effect [5]. These reversible effects were discovered separately by Seebeck [6] and Peltier [7] respectively. These separate discoveries are called Seebeck and Peltier effects respectively in honour of the scientists. The Seebeck effect is a phenomenon that describes how a temperature difference creates charge flow, while the Peltier effect on the other hand, illustrates how an electrical current can create a heat flow.

Studies also showed that for small temperature differences the voltage produced between the hot and cold ends of a single conducting rod is proportional to the temperature difference between the two ends. The proportionality constant S is now known as the Seebeck coefficient and is defined as [8]:

$$S = \frac{\delta V}{\delta T} \tag{1.0.1}$$

where δT is the temperature difference between the two ends of a material and δV is the thermoelectric voltage generated. Thus S is a measure of the magnitude of an induced thermoelectric voltage in response to a temperature difference across the material. The magnitude is very small as stated earlier due to the fact that the voltage generated is quite small. However, S is temperature dependent. We know that in semiconductors the kinetic energy of the charge carriers is strongly temperature-dependent while in metals the temperature effect is less strong [8]. The thermoelectric potential of a materisal is captured by its figure of merit defined by Maham *et al.* [9, 10] as

$$Z = \frac{\sigma S^2}{\kappa_{tot}} \tag{1.0.2}$$

where Z has the dimension of inverse temperature. σ is the electrical conductivity, S is the Seebeck coefficient and κ_{tot} is the total thermal conductivity, given by the sum of lattice as well as electronic contributions. The efficiency of the thermoelectric conversion is defined by the dimensionless figure of merit given by

$$ZT = \frac{\sigma S^2 T}{\kappa_{tot}}. \tag{1.0.3}$$

The low Seebeck coefficient and large electronic contribution to thermal conductivity in metals lead to their classification as poor thermoelectric materials, so σ and κ_{tot} will both be large. Insulators,

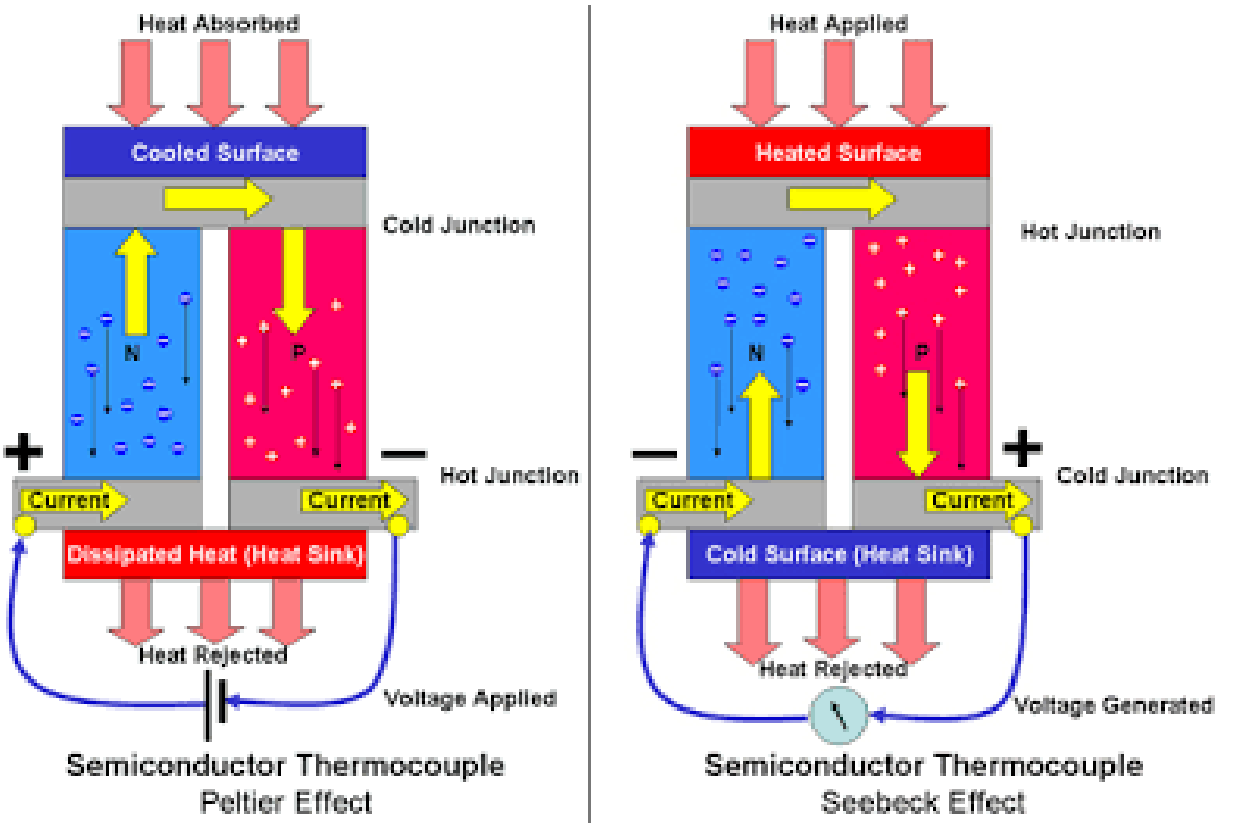


Figure 1.1: A diagramatic illustration of Peltier effect generator and Seebeck effect generator.

however, have high Seebeck coefficients and small electronic contributions to the thermal conductivity. Their charge densities are low and therefore their electrical conductivities are low, leading to a small thermoelectric effect. The best thermoelectric materials are semiconductors with an electronic density around 10^{19} /cm^3 [11]. Semiconducting materials are used to make thermocouples which can be used to generate electricity using the Seebeck effect or as cooling devices using the Peltier effect, as illustrated on Figure (1.1). Since the voltage generated by the thermocouple is very small, many coupled thermocouples will be required to make a practical thermoelectric generator. Thermolectric devices, have therefore, unlocked a potential for another source of electricity generation. For well over a century, thermocouples were being made from metallic conductors but having efficiencies barely above 3%. The use of semiconductors as thermoelectric generators has shot up this generator efficiencies to about 5% and Peltier cooling from ambient to below 0 ^{o}C has also been achieved [12].

Incorporating the Carnot limit (i.e Carnot efficiency) which specifies limits on the maximum efficiency that any heat engine can obtain, we can write the performance of thermoelectric materials as

$$\eta = \eta_{carnot} \frac{\sqrt{1 - ZT} - 1}{\sqrt{1 + ZT} + \frac{T_c}{T_H}} \tag{1.0.4}$$

where η, η_{carnot} , T$_C$ and T$_H$ represents actual efficiency, maximum efficiency, temperature of the cold reservoir and temperature of the hot reservoir respectively. For high efficiency it is required that η takes values above 100% at the temperature difference of 300 K. Thus, thermoelectric materials satisfying the relation $ZT > 1$ are thought to be especially efficient in practical applications. The Carnot limit, however, depends solely on the temperature difference between the reservoirs. Hence,

the performance, ZT, of TE materials can be easily obtained from the Seebeck coefficient S(V/K), the electrical conductivity $\sigma(\Omega\text{m})^1$, and the thermal conductivity κ (W/(Km)^1). For proper judgement the usefulness of TE materials for electricity generation as well as for heating and cooling can be characterised by ZT. The efficiency of a thermocouple depends on the fundamental properties of the thermoelectric materials used in its construction and the only way to improve it is to develop new materials with a higher figure of merit. Despite more than 180 years of experimenting with a myriad of different materials, typical thermoelectric conversion efficiencies are still only around 3% and efficiencies above 10% are yet to be achieved. The best efficiencies achieved to date in spacecraft applications are around 7% to 8%, similar to the solar absorption efficiency of amorphous Silicon (Si) solar cells, but inferior to the 24% achieved by solar cells using exotic materials [13].

In their investigation of metals, Wiedemann and Franz [8] discovered that in metals, thermal conductivity, κ, and electrical conductivity, σ, are linearly proportional. Lorentz [14] summarized the findings in a law referred to as the Wiedemann-Franz-Lorenz law:

$$\kappa_e = L_o T \sigma, \tag{1.0.5}$$

where the quantity L is the Lorentz number and T is the absolute temperature. The Lorentz number was theoretically derived by Sommerfeld [15] using the Fermi-Dirac distribution function of degenerate metals:

$$L_o = \frac{\pi^2}{3}\left(\frac{k_B}{e}\right)^2 = 2.444 \times 10^{-8} W\Omega K^{-2} \tag{1.0.6}$$

where k_B is the Boltzmann constant, and e is the electronic charge. This relation, (1.0.6), can be derived from the free-electron model:

$$\sigma = \frac{ne^2\tau_{el}}{m_e^*} \tag{1.0.7}$$

where τ_{el} is the average collision time of the electrons, n is the number of electrons, per volume and m_e^* is the effective mass of an electron. The electronic thermal conductivity κ_e is given by the relation:

$$\kappa_e = \frac{1}{3} C_e \upsilon_F l_e = \frac{\pi n {k_B}^2 T \tau_{el}}{3 m_e^*} \tag{1.0.8}$$

where C_e is the specific heat of the electrons, υ_F is their Fermi velocity and l_e is the mean free path of the electron. Thus,

$$\frac{\kappa_e}{\sigma} = \frac{\pi^2}{3}\left(\frac{k_B}{e}\right)^2 T = L_o T \tag{1.0.9}$$

The mean free path l_e can be reduced by collisions with impurities and phonons in impure metals, in disordered alloys or semiconductors. Equation (1.0.9) has been obtained from the average collision-time approximation for free electrons in addition to the assumptions that only electrons carry heat. Hence the Wiedemann-Franz law is only valid for cases in which the elastic scattering of electrons dominates. Close examination of equations (1.0.5) and (1.0.9) suggests that the experimental observation of the thermal conductivity κ_{tot} by Wiedemann and Franz in (1.0.9) must represent the total thermal conductivity κ_{tot} and the phonon contribution to heat transport. We note that the thermal conductivity is related to the transfer of heat through a material is by both electrons and quantized vibrations of the lattice called phonons and it is given by the relation $\kappa_{tot} = \kappa_l + \kappa_e$ where κ_l and κ_e are the lattice and electronic contributions respectively. We observe also that in order to optimize the ZT value in (1.0.3), separating the electronic contribution from the phonon part is key to obtaining a TE material of high ZT value, which is the main objective of this work.

1.0.1 Phonon-Glass electron-Crystal Concept

Materials under investigation as thermoelectrics by research groups around the world include clathrates [16, 17], skutterudites [18], half-heusler alloys [19], and complex chalcogenides [20]. Thermoelectric clathrates hold significant promise for TE applications and have over the years witnessed interest largely driven by the development of the "phonon-glass electron-crystal" (PGEC) concept coined by Slack in 1995 [17]. The figure of merit, Eq. (1.0.6), shows that it is desirable to have a high electrical but low thermal conductivity. The PGEC concept suggests that a good TE material should have the electronic properties of a crystalline material, large σ, and the thermal properties of a glass material, low thermal conductivity.

Thermal conductivity is related to the transfer of heat through a material by the electrons and the lattice. The figure of merit, ZT, is important because the power factor, $S^2\sigma$, can be optimized in TE clathrate materials as a function of carrier concentration through doping, to give a large ZT. However, any increase in the power factor will also lead to increase in k_e, as we can see from the Weidemann-Franz law, thereby lowering ZT. This dilemma, created by the need to increase ZT by increasing the power factor and lowering the thermal conductivity at the same time, has led to the search for a material with a high power factor and a low k_l. Most of the research area as it relates to TE materials are focused now on how to reduce the lattice part of the thermal conductivity to a minimum [21].

This work will investigate how the guest atom reduces the thermal conductivity in type-I Tin (Sn) clathrates

1.0.2 Semiconducting clathrates

There are over 120 inorganic compounds with clathrate structures. Semiconducting clathrates crystalise in three structural types, often denoted by Roman numerals: type-I, type-II and type-III. The distribution over the structural types is however non-uniform. The type-I clathrates compounds, for example, have almost 100 or more in existence. For a comprehensive summary of clathrate structures refer to the work of Kaltzoglou [22]. Thermoelectric clathrates are covalently bonded open-frameworks of host atoms interconnected by directional bonds in such a way that some volume is left empty and thus available to incorporate guest atoms [23]. Most TE studies of clathrates have concerned the type-I clathrate structure [24] and this study will focus on the type-I Sn structure with encaged K, Rb and Cs as guest atoms. The clathrate type-I is composed of two types of polyhedra *viz* pentagonal dodecahedra (5 sided polyhedron with 12 flat surfaces) and tetrakaidecahedra (5 sided polyhedron with 14 flat surfaces) framework atoms. The polyhedra are covalently bonded to each other by shared faces. They are packed in a cubic arrangement, with eight polyhedra per cubic unit cell, two small dodecahedra and six larger tetrakaidecahedra [24]. The prototypical type-I Sn clathrates have a simple cubic lattice structure (space group $Pm\bar{3}n$, No. 223) which has 46 framework atoms and 8 encapsulated guests (two in dodecahedral and six in tetrakaidecahedral cages). Figure (1.2) shows the polyhedra forming units of A_8Sn_{46-x} (A= K, Rb, Cs, x = 0,2). We shall be investigating specifically the three binary clathrate compounds A_8Sn_{46-x} where (A= K, Rb, Cs,) and (x = 0,2).

The design of optimized TE clathrate materials requires an indepth understanding of the lattice dynamics of the clathrate compounds, especially as it relates to the lowering of the thermal conductivity. However, to date, there has not been consensus among researchers on what is responsible for the lowering of the thermal conductivity in clathrate materials. Two schools of thought that emerge have consistently based their arguments on both theoretical and experimental studies which usually make certain assumptions. It

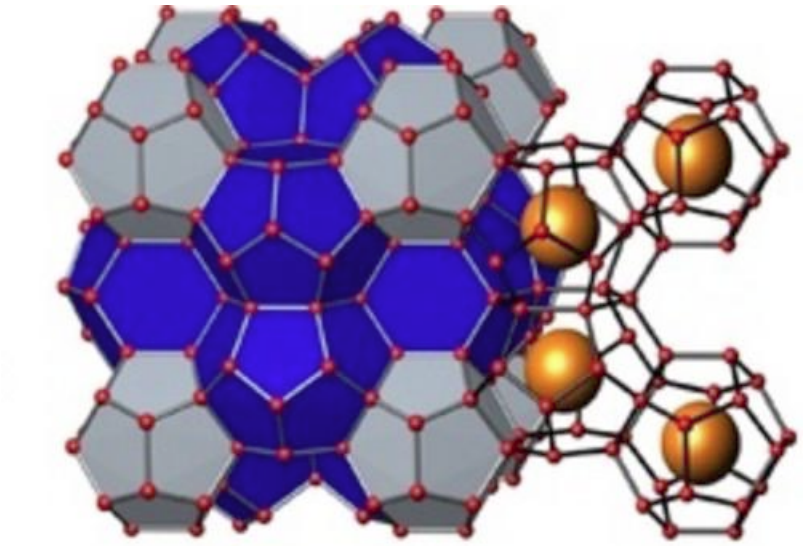


Figure 1.2: Type-I clathrates polyhedra.

is generally assumed that the guest atoms in clathrates act as rattlers and essentially induce a disordered lattice dynamics referred to as phonon glass [17]. Koza et al. [18] in their investigation of $LaFe_4Sb_{12}$ and $CeFe_4Sb_{12}$ reported a temperature-independent lattice dynamics with well-defined phase relations between guest and host, which they reported was indicative of a quasi-harmonic coupling between guest and the host lattice. This is in disagreement with the phonon-glass model based on individual rattling of the guest atoms. Also, Christensen *et al.* [25], related the phonon life times to the low thermal conductivity. They reported that in a PGEC material, the electrons move through crystalline energy bands, while the crystalline phonons are scattered by a set of loosely bound scatterers, called rattlers, to produce a short phonon mean free path which mimics an amorphous material [26]. Their results for $Ba_8Ga_16Ge_{30}$ shows evidence of localized mode coupling, which agrees with the theoretically predicted avoided crossing of the rattler modes and the acoustic-phonon branches. However in an investigation on the concept of rattling behaviour, Hermann *et al.* [27] suggested that rattling behaviour is associated with a weak bonding of the guest to the occupied nanocages, introducing the possibility of an independent, non-correlated vibration of the guest. With this assumption, they characterized an independent rattling mode to fit into their investigation. The purpose of this study is, to investigate the fundamental mechanisms of thermal conductivity as these relates to the dynamics of the rattlers in clathrate materials. Specifically, how do the rattling atoms reduce the lattice thermal conductivity in type-I Sn clathrates?

1.1 Motivation

Demand for higher performance high temperature thermoelectric materials is on the increase due to depleting fossil fuels and increasing effort to reduce green house gas emissions [5]. The clathrate materials are of interest because they are semiconductors with adjustable band gaps[16]. Also, of the group-14 elements, Si, Ge, and Sn, studies show that the larger framework cavities in Sn clathrates compared with the others, favor the rattling of the guest atoms more, and, hence, decreases the lattice contribution to the thermal conductivity [28, 29, 30]. These characteristics mean that they have potential to be developed into high efficiency TE materials, primarily because of their low thermal conductivity.

Current research effort is aimed at raising the current efficiency of TE figure of merit ZT, and have materials that have the capacity to operate in new and broader temperature ranges [5].

There is a need for detailed analysis of the trajectories of the guest atoms inside the cages formed by clathrate compounds, in order to asses the rattling characteristics of the compound. Calculating simulated elemental spectra, atomic root-mean square displacements, and Pearson coefficients in order to determine atomic dynamical correlation will enable us to asses the diffusive motion of the atoms for proper understanding of the rattler effects. The quantitative study of the rattler effect such as phonon life times can be achieved through molecular dynamics (MD) simulation [31], which may add significantly to our understanding of the mechanism of thermal conductivity. Lattice dynamics calculations will be performed and the results used to plot phonon dispersion curves as well as estimate phonon group velocities. The phonon dispersion curves will give indications of any avoided crossing between the localized modes of the rattler and the acoustic phonons of the cage. Such information may clarify the nature of any dynamical interactions that may exist between the rattler and the cage, and, thus, provide answers to our research question.

1.2 Aim and Dissertation outline

Our aim is to investigate how the guest atoms reduce the thermal conductivity in type-I Sn clathrates. A combination of *ab initio* MD and lattice dynamics will be used to study the normalized phonon spectra of type-I Sn clathrates. The tasks involved in this work are outlined below:

- We start our calculation by first carrying out a geometry optimization of structures of the compounds A_8Sn_{46-x} (A= K, Rb, Cs,) and (x = 0,2), using four (DFT) exchange correlational functionals.
- We then proceed to calculate the electronic and phonon band structures, using the most suitable exchange functional.
- The lattice thermal conductivity calculations are performed using the Linearized Boltzmann Transport Equation (LBTE) approach under the single-mode relaxation time (SMRT) method [32, 4].
- The calculations of the thermoelectric properties will follow in order to determine the suitability of our system for thermoelectric applications.
- From the lattice dynamics calculations, the group velocity, spectrum of the phonons and, most importantly, the phonon dispersion relation of the avoided crossing can be studied.
- Phonon dispersion curves would now be plotted and an analysis of the rattling metal obtained.

.

The dissertation is organised as follows: In chapter 2, we review clathrate materials and discuss their classification. In chapter 3, the theoretical framework on which this work is based is discussed. In chapter 4, we discuss the various methods employed in this work that facilitated the results presented and, finally, we discuss the results and limitations of our work in chapter 5. Chapter 6 is the summary of my work and expectations for future work.

2

Literature Review

This chapter provides an in-depth description of the crystal structures of clathrates. The formation of the clathrate compound and defects in the framework are discussed. Finally, a table of the highest thermoelectric efficiency factor ZT, for type-I clathrates so far achieved, is presented.

2.1 Clathrates as cage materials

Type I clathrates have experienced a surge in interest within recent years due to their promising thermoelectric properties especially caused by a very low thermal conductivity. Clathrates are classified among a group of inorganic materials called cage compounds. The structural characteristics of this group has been summarised in extended reviews [33, 34]. Of interest is the intermetallic clathrates which have framework formed predominantly by four connected atoms. The arrangements of the atoms in clathrates form three-dimensional polyhedron bearing large cavities often referred to as 'cages' with $20-$ atom dodecahedron, $24-$ atom tetrakaidecahedron, $26-$ atom pentakaidecahedron and $28-$ atom hexakaidecahedron vertices. In the simple cubic structure, binary type-I clathrate general formula is given by A_8Sn_{46-x} , where A is a metal. There are 46 framework atoms in each unit cell, two small 20-atom cages (pentagonal dodecahedra), and six large 24-atom cages (tetrakaidecahedra) Figure (2.1). These solids are isostructural with gas hydrates such as $8Cl_246(H_2O)$ [35]. The metal atoms can be trapped in the pentagonal dodecahedra and in the tetrakaidecahedra. In A_8Sn_{46-x} (x = 0,2), however, the number of metal atoms (usually alkali-metal and alkaline-earth metal) in these compounds varies depending on their size. If the metal atom is too big, only the larger cages are occupied and the small ones are empty. When all the available cavities are occupied, the type-I clathrate has the ideal formula A_8Sn_{46}, offering eight sites per unit cell for guest atoms. For intermetallic type-I clathrates of A_8Sn_{46-x}, the composition results from the fact that each framework atom is shared by four polyhedral cages. Using the formalism adopted by Reny and Horie [36, 37], the content of the unit cell is two ASn_{20} and six ASn_{24} which gives A_8Sn_{46}. It was reported by Baitinger *et al.* [38] that in-spite of the very clear structural pattern based on four-connected atoms within the frameworks, clathrates seldom have completely ordered crystal structures. Also, it is possible to have different crystallographic disorder and defects in the framework and in the cages.

This work, however, is limited to binary type-I clathrates, where the formation of vacancies is only possible at certain positions where there is allowance for the adjustment of the total electronic balance-Zintl-Klemm concept as discussed in subsection (2.1.3). Since the first report of the non-defect structure

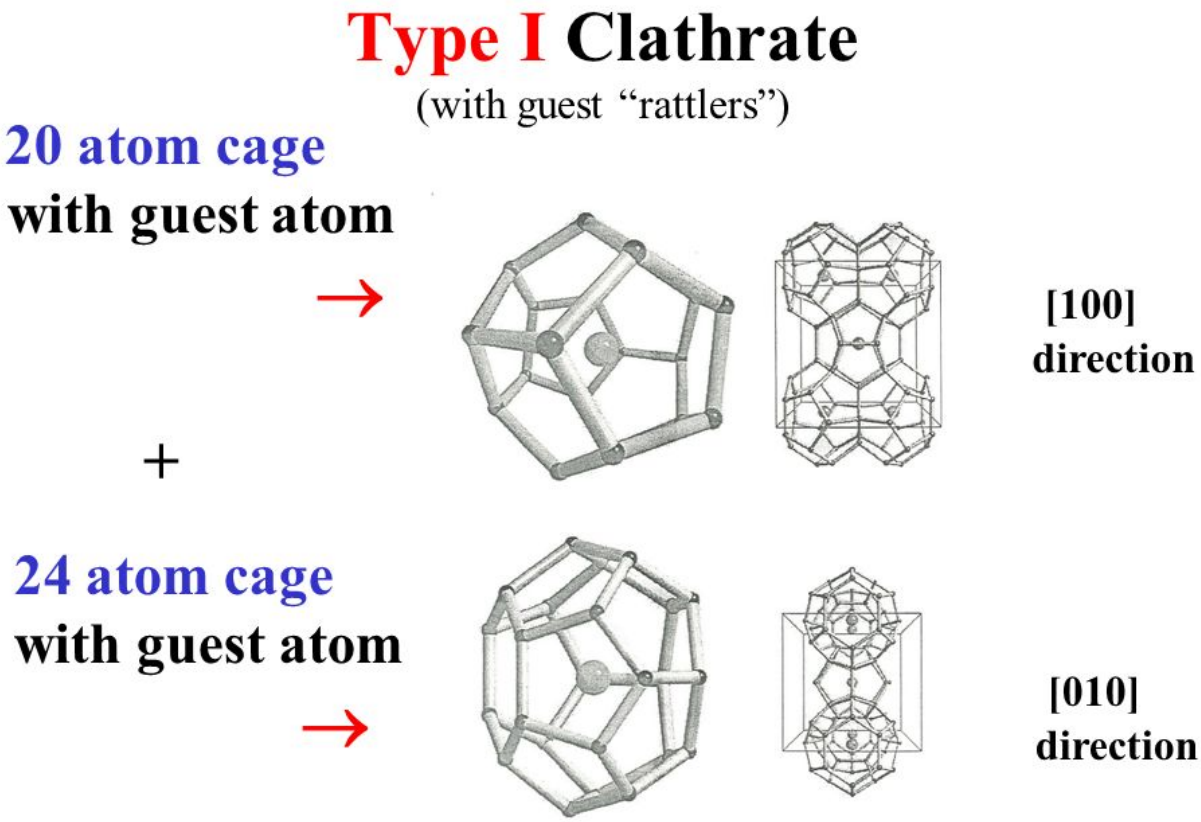


Figure 2.1: Source Myles [1]) Type-I clathrates polyhedra showing 20- and 24- atom cages with guest atoms

K_8Sn_{46} [39], the exact composition and structure of the type-I tin clathrates was brought into question [40, 41].

2.1.1 Classification of semiconducting clathrates

All known hydrates crystallise in seven structural types, which differ in the type of polyhedra formed in the framework and the mode of their arrangements in the three-dimensional structure [42]. Of the seven structural types; semiconducting clathrates crystallise only in three, which are denoted by Roman numerals: type-I clathrate, type-II clathrate and type-III clathrates [42]. In all cases the ratio of the cavity size in the host framework to the size of the guest molecules or atoms is significant in the formation of a clathrate structure. Almost 100 type-I clathrate compounds are known. About 10 compounds have the type-II clathrate structure, while only a few type-III clathrate compounds have been synthesized. We can also classify clathrates according to the formal charge of the framework *viz*, polyanionic, polycationic and neutral charge clathrates [43, 44].

2.1.2 The PGEC Concept

The "phonon-glass electron-crystal" concept was first coined by Slack [17] as a summary of ideas discussed in references [45, 46]. Generally, materials that have no periodic arrangement of atoms are glasses and amorphous materials, and are known to show the lowest thermal conductivities. Takabatake *et al.* [3] stated in their review that Ioffe in the 1930s, noted that semiconductor thermoelements are more practical than the materials employed at that time. Ioffe then proposed a design concept that is to reduce the phonon thermal conductivity by forming semiconducting mixed crystals with narrow band gaps composed of heavy elements [46]. One of the very first material that was designed to fit this concept was the Skutterudite compounds [47]. The crystal structure of the Skutterudite contains voids/fillers trapped in anharmonic potentials but capable of vibrating with large amplitudes [48]. Morelli *et al.* [49] reported that guest atoms have a strong influence on the phonon thermal conductivity, while Dong *et al.* [26] in their paper revealed that all the voids need not be occupied in order to achieve a maximum reduction in phonon thermal conductivity. Type-I clathrate compounds were reported by Nolas *et al.* [16] to be good candidates for high-efficiency thermoelectric material. Sales *et al.* [50] introduced the term "rattler" and "rattling" meaning guest atoms and the anharmonic motion of the rattlers respectively. Tse *et al.* [51] noted in their paper on clathrate hydrates, that some rattler elements undergoing anharmonic motion in cages, lower the phonon thermal conductivity. However, they opined [51] that the coupling between guest modes and acoustic phonons arising from networked cages leads to the glass-like behaviour in the thermal conductivity of clathrate hydrates. Slack *et al.* [17] first drew attention to the "rattling" of atoms entrapped inside clathrate polyhedra as being responsible for lowering of the thermal conductivity. Shoko *et al.* [52] defined rattling dynamics as a local, low-frequency, and anharmonic thermal vibration of a guest atom that is weakly bound to its surrounding atoms that form an oversized atomic cage and has been reported to be a factor in the lowering of the thermal conductivity in clathrates [53]. More than a decade ago, Slack [17, 54] proposed that the encapsulated atoms undergo displacements inside the cage, and further stated that the cage atoms make the largest contribution to the Seebeck coefficient and the electrical conductivity. This proposal opened a new window in the study of clathrate materials and has continued to generate interest among researchers. It is believed that the localized vibrations of the guest metal atoms resonantly scatter lattice phonons [55]. It is a unique feature of these clathrates, that the encapsulated metal, while effectively donating its valence electrons to the framework, is not strongly ionic [56]. This is true because the effective Bohr radius of the valence s electrons of the guest overlaps strongly with the framework of the clathrate. Thus, while the thermal motion of the metal helps to lower the thermal conductivity, it is not expected to seriously affect the electrical conductivity, which occurs through the framework. Thus, clathrates serve as a typical example that describes the concept of a phonon glass electron crystal [54, 17] and as such, are promising thermoelectric materials.

2.1.3 The Zintl-Klemm Concept

The Zintl-Klemm concept (ZKC), mentioned previously is a combination of a valence electron counting rule and a set of structure- chemical considerations. A Zintl phase is the product of a reaction between group 1 or group 2 elements, and post transition metal or metalloids from group 13, 14, 15 or 16 [57] of the periodic table. Zintl phases were named for the German chemist Eduard Zintl who investigated them in the 1930s [58]. The term "Zintl Phases" was first used by Laves in 1941 [59]. Application of the Zintl-Klemm concept has been used for understanding the structure and composition and defects in the crystal structure of binary tin clathrates-I of alkaline metals according to the formula $A_8E_{44}\square_2$ [40, 60]. Baitinger *et al.* in [38] described the Zintl -Klemm concept succinctly starting from the

simplest crystal structure built of four-bonded atoms in diamond. Each carbon atom has four shortest distances to its neighbours. Each atom has four valence electrons, which allows interpretation of all the short contacts as two center-two electron$(2c-2e)$ bonds. In a similar clathrate-I compound Na_8Si_{46}, the unit cell of the compound has 92 short contacts within the framework, comparable with the sum of the covalent radii of the participating atoms (d(Si-Si) $= 2.292 - 2.381$ Å, $2r_{cov}$(Si) $= 2.34$ Å) [61]. Also, 184 shortest contacts between the guest and the framework atoms are larger than the sum of the corresponding atomic radii (d(Na-Si) $= 3.269 - 3.358$ Å in the pentagon dodecahedron and (d(Na-Si) $= 3.432 - 3.944$ Å in the tetrakaidecahedron, r_{at}(Si) + r_{at}(Na) $= 1.17 + 1.53 = 2.70$ Å [61]). This shows that the available 92 valence electrons would not be sufficient to form $(2c-2e)$ bonds between the Na and the surrounding Si atoms in the Si_{20} and Si_{24} cages. To apply this Zintl-Klemm concept to clathrates, only the bonds within the framework are considered as $(2c-2e)$ bonds. The average number of valence electrons per framework atom is four and each atom obtains a formal charge. It should be easy to see the interaction between guest and the framework as charge transfer from this perspective. This suggests that in the anionic clathrates, the guest cations deliver their valence electrons to the framework; while the reverse is the case for cationic clathrates, were the guest anions accept excess electrons from the framework. Considering a complete host framework, we can write:

$Cs_8Sn_{46} = [Cs^{1+}]_8[(4b)Sn^0]_{46} \times 8e^-$,

where $4b$ stands for four-bonded atom. For a balanced chemical equation, the excess electrons can be compensated for by introducing two defects from the framework atoms. That is, the eight neighbouring tin atoms will then be three-bonded:

$Cs_8Sn_{44}\square_2 = [Cs^{1+}]_8[(4b)Sn^0]_{36}[(3b)Sn^{1-}]_8 \times 0e^-$,

where $3b$ stands for three-bonded atom. This gives a balanced chemical equation. Baitinger *et al.* [38] showed that beside the chemical composition and structural features, the Zintl-Klemm concept of electron balance can be connected to the electronic density of states (DOS). However, one of the shortcomings of the Zintl-Klemm concept is that it could not sufficiently discuss the guest-framework interactions, because, by definition it is restricted only to the coulomb forces caused by charge transfer. Recently, the electron localizability approach based on electron density and electron localizability indicator was developed for proper description of chemical bonding in intermetallic compounds [62]. With this approach, the quantum theory of atoms in molecules (QTAIM) has been used to describe the shapes of the electron density [63].

2.1.4 Type-I clathrate polyhedra

The type-I clathrate structure is composed of pentagonal dodecahedra 5^{12} and larger 14-face tetrakaidecahedra $5^{12}6^2$. The unit cell contains 46 atoms in the framework and has 2 small and 6 large cavities called "cages". Most type-I clathrate structure compounds crystallise in a cubic structure (space group $Pm\bar{3}n$, No. 223), with 46 framework atoms occupying three Wyckoff sites, *viz.*, $6c$, $16i$ and $24k$. Site symmetry is used for characterization of the structure and for the study of local properties. Saiga et al. [64] reported experimental structural, transport, and thermal properties of carrier-tuned $Ba_8Ga_{16}Sn_{30}$ (n) single crystals with the type-1 clathrate structure (β) phase, demonstrating that the compound is a unique thermoelectric clathrate material and that both the structure type and the carrier type are tunable. Also, Saramat *et al.* [65] reported p-type $Ba_8Ga_{16}Ge_{30x}$ (x = 0.95, 1.00, 1.05, 1.10), these type-I clathrates with different Germanium contents were synthesized by combining melt method with spark plasma sintering (SPS). The effects of Germanium content on electrical transport properties have been investigated, with result showing that all samples exhibit p-type conduction. A maximum power

factor value of 0.35 $\times$ 10^3 W m^1 K^2 was obtained at 550 K. Similar theoretical calculations by Kono *et al.* [66] for thermoelectric properties of type-I and type-VIII of $Ba_8Ga_{16}Sn_{30}$ (n) and (p) reveals a figure of merit 1.1 and 0.7 at 700 K and 500 K respectively. DFT calculations by Møllnitz *et al.* of K_8Sn_{44} [67] also reported ZT values of 0.08 and 0.05 at 650 K and 800 K respectively. In Table (2.1), various type-I clathrate compounds along with their highest ZT values are presented. It is noted from Table (2.1), that n-type materials have higher figure of merit compared to p-type of the same chemical compositions e.g. $Ba_8Ga_{16}Sn_{30}$ (n-type = 1.45, p-type = 0.7). Also compounds with Sn framework have higher figure of merit compared to the Ge framework compounds of the same compositions e.g. $Ba_8Ga_{16}Sn_{30}$ (Sn framework = 1.45, Ge framework = 1.35), even though the temperature of the Ge framework compound is higher. The stoichiometric compounds are observed to have a lower figure of merit e.g. K_8Sn_{46} = 0.05, while $K_8Sn_{44}\square_2$ = 1.1. Although there is no clear trend in variation of figure of merit with temperature on these table, it is noted in most of the works sited that the figure of merit peaks at the the temperatures quoted and start droping afterwards.

Table 2.1: ZT values of some type-I clathrates.

Compounds (type)	ZT	T(K)
$Ba_8Ga_{16}Sn_{30}$ (n) [64]	1.45	500
$Ba_8Ga_{16}Ge_{30}$ (n) [65]	1.35	900
$Ba_8Ni_{0.31}Zn_{0.52}Ga_{13.06}Ge_{32.2}$ (n) [68]	1.2	1000
$Ba_{7.5}Yb_{0.5}Ga_{16}Ge_{30}$ (n) [69]	1.09	950
$Ba_8Ga_{10}In_6Ge_{30}$ (n) [70]	1.03	943
$Ba_8Ni_{0.32}Ga_{13.63}Ge_{31.71}$ (n) [71]	0.94	1000
$Ba_8Ni_{0.22}Zn_{7.22}Ge_{37.12}Sn_{1.44}$ (n) [72]	0.9	830
$Ba_8Ga_{16}Si_{30}$ (n) [73]	0.87	873
$Ba_8Zn_{7.66}Ge_{36.55}Sn_{1.79}$ (n) [74]	0.82	850
$Sr_8Ga_{15.5}In_{0.5}Ge_{30}$ (n) [75]	0.72	800
$Ba_8Ga_{16}Al_3Ge_{27}$ (p) [76]	0.61	763
$Ba_8Cu_{5.1}Ge_{40.2}Sn_{0.7}$ (n) [77]	0.6	773
$Ba_8Cu_5Ge_{41}$ (n) [68]	0.4	390
$Ba_8Cu_6Si_{17}Ge_{23}$ (n) [78]	0.31	520
$Ba_8Al_{16}Ge_{30}$ (n) [79]	0.24	800
K_8Sn_{44} [67]	0.08	650
K_8Sn_{46} [67]	0.05	800
$Ba_8Ga_{16}Sn_{30}$ (n) [66]	1.1	700
$Ba_8Ga_{16}Sn_{30}$ (p) [66]	0.7	500

2.2 Thermoelectricity and Power generation in type-I Clathrates

The search for alternative energy from fossil fuel is a continuous search. Amongst the numerous materials discovered for alternative energy, is the class of materials called thermoelectric materials that can capture and convert waste heat to useful energy. Clathrate materials stands out within the subset of these group of materials because of their unique features. Clathrates compounds combine low, glass-like thermal conductivity with high electrical conductivity and Seebeck coefficient, signatures of prospective thermoelectric materials [16]. Recent years have witnessed appreciable progress in enhancing thermoelectric efficiency of clathrates through various strategies like, phonon engineering approaches,

introduction of rare earth guests and formation of complex superstructures. With advances in research, new compositions of clathrates have emerged, that allow combination of reasonably high thermoelectric efficiency displaying high values of figure of merit, making them competitionally viable as alternate source of electricity generation. Among the competitive new materials, one advantageous property of clathrates is that their crystal structure, especially, the non dependence of forming host and guest substructures, creates opportunity for tuning of the charge carrier transport almost separately from phonon transport [80]. Clathrate thermoelctric materials are said to be useful in applications such as imaging (magnetic resonance), space craft, study of the photo-behaviour of organic mixtures and solar cells amongst others. The discovery of earth aboundat materials as clathrates, it is hoped, will greatly enhance its exploration for commercial production.

3

Theoretical Framework

This chapter establishes the theoretical framework of this work. Our goal is to probe the lattice and electronic structure of clathrate-I Sn binary compounds computationally. *Ab initio* or first-principles methods have emerged in the last three decades as a powerful tool to examine the properties of matter at the microscopic scale. These approaches are used to derive macroscopic observables under the controlled conditions of a computational experiment, and with predictive power rooted in the quantum-mechanical description of interacting atoms and electrons. The theoretical background describing the structural and electronic properties of our material is centred on the popular Density Functional Theory (DFT). Density-functional theory has become the *de facto* method of choice in computational materials science, due to its combination of reasonable scaling with system size, and good accuracy in reproducing most ground state properties. Such an electronic-structure approach can then be combined with classical molecular dynamics to provide an accurate description of thermodynamic properties of our compounds.

In this chapter only a brief outline of some of the techniques used are given. A short description of DFT is given on Appendix A and a description of the main DFT code, the Vienna *ab initio* Simulation Program, VASP, used in the work is given in Appendix B. Boltzman transport equations are briefly discussed in Appendix and some comments on phonon calculations appear in Appendix C and D.

Molecular dynamics is used to probe the atomic lattice in order to be able to answer part of our research question. Hence we start our discussion with the theory governing *ab initio* Molecular dynamics.

3.1 Equation of state

The equation of state (EOS) of solids describes the relationship between thermodynamic variables of compressed solids, and is applied in investigating thermodynamic properties of materials [81].
Many, semi-emperical relations have been proposed to describe the EOS [82]. In this work, we used the Murnaghan-Birch equation of state [83]. Suppose the energy of a compressed system is described as a Taylor series,

$$E(f) = a + bf + cf^2 + \dots \tag{3.1.1}$$

where f is a finite strain given by

$$f = \frac{1}{2}\left[\left(\frac{V_0}{V}\right)^{2/3} - 1\right] \tag{3.1.2}$$

The pressure and bulk modulus are respectively defined as

$$P = -\frac{\partial E}{\partial f} \cdot \frac{\partial f}{\partial V}, \tag{3.1.3}$$

$$B = -V\left(\frac{\partial P}{\partial f} \cdot \frac{\partial f}{\partial V}\right) \tag{3.1.4}$$

The second order of (3.1.3) gives

$$P = \frac{3B_0}{2}\left[\left(\frac{V_0}{V}\right)^{7/3} - \left(\frac{V_0}{V}\right)^{5/2}\right] \tag{3.1.5}$$

In above equations V_0 is the equilibrium volume of the system, and B_0 is the isothermal bulk modulus. The third order shows increased accuracy over the Murnaghan equation of state and has a relatively simple analytical form

$$P = \frac{3B_0}{2}\left[\left(\frac{V_0}{V}\right)^{7/3} - \left(\frac{V_0}{V}\right)^{5/3}\right]\left[1 + \frac{3}{4}(B_0^{'} - 4)\left(\left(\frac{V_0}{V}\right)^{2/3} - 1\right)\right] \tag{3.1.6}$$

Here $B_0^{'}$ is the bulk modulus derivative. The energy is obtained by integration of the pressure

$$E = E_0 + \frac{9V_0B_0}{16}\left\{\left[\left(\frac{V_0}{V}\right)^{2/3} - 1\right]^3 B_0^{'} + \left[\left(\frac{V_0}{V}\right)^{2/3} - 1\right]^2\left[6 - 4\left(\frac{V_0}{V}\right)^{2/3}\right]\right\} \tag{3.1.7}$$

Using data from the GGA in the PBE parametrization and Thatchenko-Scheffer (vdW-TS) calculations, we fitted the total energy versus the volume to the third order Murnaghan-Birch EOS, and, thus, deduced the equilibrum ground state properties of the system, namely, lattice constant (a), bulk modulus B_0 and pressure derivative of the bulk modulus ($B_0^{'}$), for details see reference [84].

3.2 Cage size and vacancy formation

Two preconditions for the formation of clathrate structure are, (1) the presence of a host environment built from cross-linked tetrafunctional units, and (2) the ability of the corresponding guest types to occupy the cavities (cages) in the framework formed. According to the results of X-ray and neutron diffraction studies, the guest atoms show very large displacement parameters in Sn cages, compared to other group-14 elements. Since there is no strict bond between the framework and the guest, from the relaxed structure, the bond length of Sn-Sn and A-Sn (A= Cs, Rb and K) were determined. In a study by Kaltzoglou *et al.* [85], a fine grasp of the lattice defects and phase transitions in clathrate-I compounds play a decisive role in the understanding of the stannide clathrates structure. It has been reported that one vacancy per six-membered ring is favoured over two such vacancies per ring [86, 67]. Crystallographic disorder and complexity of the crystal structure of clathrates has been extensively reported in literature [38, 87]. Of interest to this work is the formation of vacancies in these compounds which was reported allows for the adjustment of the total electronic balance -Zintl Kleim.The Zintl-Kleim concept allows complete understanding of the composition and defect in the binary type-I Sn clathrate, further details Section (2.1.3). The packing of the polyhendron framework creates two type of cages, a large cage formed by the tetrakaidecahedra (12 pentagonal and 2 hexagonal faces) and a smaller cage from the pentagonal dodecahedra rings.

3.3 Cohesive energy

The cohesive energy of a solid is defined as the energy required for separating the condensed material into isolated free atoms. For molybdenum chalcogenides $M_mX_n(M_m = Mo_m, X_n = S_n)$, the cohesive energy is given by

$$E_{coh}^{M_mX_n} = \frac{E_{solid}^{M_mX_n} - Z \times (mE_{atom}^{M_m} + nE_{atom}^{X_n})}{Z \times (m+n)}, \tag{3.3.1}$$

where Z is the number of M_mX_n per unit cell, $E_{atom}^{M_m}$ and $E_{atom}^{X_n}$ are the energies of the spin-polarized non-spherical isolated M and X atoms in its electronic ground state. These energies are computed by placing a free atom in a big orthorhombic unit cell. such that every atom is surronded by at least 15%. $E_{solid}^{M_mX_n}$ are the bulk cohesive energies with respect to spherical non spin-polarized reference atoms, and $m, n = 1, 2$ are the stoichiometric weights. The cohesive energy will be obtained from the fit to a Murnaghan-Birch third order equation of state and will be used to deduce the structural parameters and to predict the stability of the structures.

3.3.1 Formation Energy

The formation energy is defined as the heat of formation per atom of the structure under consideration. Let us consider that the solid M_mX_n result from the interaction between the molybdenum (solid) M_m and the gaseouse chalcogenide X_2 through the chemical reaction [88]

$$mM^{solid} + \frac{n}{2}X_2^{solid} \rightleftharpoons M_mX_n^{solid}. \tag{3.3.2}$$

To compare the relative stabilities of the various structures, we define the formation energy as

$$E_f(M_mX_n^{solid}) = E_{coh}(M_mX_n^{solid}) - \frac{mE_{coh}(M^m) + \frac{n}{2}E_{coh}(X_2^{gas})}{m+n} \tag{3.3.3}$$

where $m, n = 1, 2$ are the stoichiometric weights and $E_{coh}(M_mX_n^{solid})$ is the cohesive energy per atom as described in (3.3.1), and $E_{coh}(M^{solid})$ and $E_{coh}(X_2^{gas})$ are the ground state cohesive energy of M^{solid} and X_2^{gas} respectively.

3.4 Ab initio Molecular Dynamics

One of the important elements in an *ab initio* molecular dynamics (AIMD) calculation is the representation of the electronic structure. The ability of MD calculations to describe physical systems depends on the accuracy of the inter-particle interaction potentials. In this work, we obtain the interparticle interactives from DFT. DFT is one of the most widely used methods for *ab initio* calculations and analysis of the structure and properties of material [89]. For an extensive review of the AIMD method, see references [89, 90]. DFT formulates the many-electron problem in terms of the electron density $n(\mathbf{r})$, rather than in terms of the many-body wave function. Nevertheless, accurate expressions for the energy in terms of the density $n(\mathbf{r})$ were not available. In 1965, Kohn and Sham [91] took a major step towards quantitative modelling of electronic structure, by introducing an orbital method by which the energy is expressed in terms of a set of n occupied single-particle orbitals $\Psi_1\ (\mathbf{r}) \cdots \Psi_n(\mathbf{r})$ and the N

nuclear positions, $R_1, \cdots R_N$, and takes the form:

$$E\left[(\Psi),(\mathbf{R})\right] = -\frac{1}{2}\sum_{i=1}^{n} dr\Psi_i^*(\mathbf{r})\nabla^2\Psi_i(\mathbf{r}) + \frac{1}{2}\int\int dr'\frac{n(\mathbf{r})\,n(\mathbf{r}')}{\mid \mathbf{r}-\mathbf{r}' \mid} + E_{xc}[n] + \int dr V_{ext}(\mathbf{R}_1\cdots\mathbf{R}_N)\,n(\mathbf{r}) \tag{3.4.1}$$

where the density $n(\mathbf{r})$ is related to the orbitals, and the orbitals are required to be mutually orthonormal. In the equation 3.4.1 above, the functional $E_{xc}[n]$ of the density, called the exchange-correlation functional, is unknown and must be approximated for. The local density approximation LDA can be employed for exchange energy:

$$E_x^{LDA}[n] = -\frac{3q^2}{4}\left(\frac{3}{\pi}\right)^{\frac{1}{3}}\int d^3r n(r)^{\frac{4}{3}} \tag{3.4.2}$$

where q is charge on an electron. This approximation though it has proved useful and reasonably accurate in many systems, could not be used for systems in which the spatial variation of the density is too rapid. The functional was then improved by including the dependence on the density and, thus, gradient. The exchange correlation energy can be written as:

$$E_{xc}^{GGA}[n_\uparrow, n_\downarrow] = \int d^3r n(r)\epsilon_{xc}^{GGA}(n_\uparrow(\mathbf{r}), n_\downarrow(\mathbf{r}), \nabla n(\mathbf{r})) \tag{3.4.3}$$

This approximation is known as the generalized gradient approximation (GGA). Two important works that discusses the formulation of the projector Augmented Wave (PAW) potential method used for the implimentation of DFT in the VASP code can be found in references [92] and [93].

3.4.1 Strategy For Combining Electronic Structure with Molecular Dynamics

The ability of MD calculations to describe physical systems depends on accuracy of the inter-particle interaction potentials. One strategy for combining electronic structure with molecular dynamics is by performing the following steps:

- Choose a given set of initial nuclear positions $\mathbf{R}_1, \cdots, \mathbf{R}_N$. Minimize the energy functional in eq. (3.4.1) to obtain the ground state density $n_0(\mathbf{r})$ and corresponding orbitals $\Psi_1^{(0)}(\mathbf{r}), \cdots, \Psi_n^{(0)}(\mathbf{r})$.
- The forces between the nuclei as given by the Hellman-Feynman theorem is :

$$F_I = -\frac{\partial}{\partial R_I}E\left[\left\{\Psi^{(0)}\right\},\{R\}\right] \tag{3.4.4}$$

- These forces are then fed into a numerical integration procedure together with a set of initial velocities for the nuclei and a step of molecular dynamics is carried out yielding a new set of positions and velocities.
- At the new nuclear positions, the energy functional is obtained and used to perform another step of molecuar dynamics (MD) propagation.
- This procedure is repeated until an entire trajectory has been generated.

.

3.5 Transport Theory

In order to obtain the transport coefficients σ, κ and S, one has to solve the transport equations (C.0.1). Two approaches to solving the transport equation as it pertains to our clathrate system are the Green-Kubo theory [94] and the semi-classical Boltzmann transport theory [95]. The former relates transport coefficients to correlation functions of the current or heat flux, while the latter treats effects of various scattering mechanisms on transport properties in terms of relaxation times. The Boltzmann transport theory has proven its validity [96, 97] in numerous applications where calculated transport coefficients can be readily compared with experimental results.

In this work we present thermal property calculations, with BoltzWann code [32] to evaluate electron transport properties in a semiclassical formalism using a maximally-localized wannier function (MLWF) basis to interpolate first-principles plane-wave (PW) results [98, 99]. The Boltzmann transport equation and derivation can be found in references [100] and [101]. In this work, the transport properties of A_8Sn_{46-n} (n = 0,2) were studied by solving the Boltzmann transport equation (BTE) within the relaxation time approximation (RTA). Under this approximation, the Cartesian components of the electrical conductivity, Seebeck coefficient and electronic thermal conductivity are obtained from:

$$\sigma_{i,j}(\mu, \mathsf{T}) = e^2 \int \left(-\frac{\partial f_0(\varepsilon, \mathsf{T})}{\partial \varepsilon}\right) \sum_{i,j}(\varepsilon) d\varepsilon \tag{3.5.1}$$

$$(\sigma \mathsf{S})_{i,j}(\mu, \mathsf{T}) = \frac{e}{\mathsf{T}} \int \left(-\frac{\partial f_0(\varepsilon, T)}{\partial \varepsilon}\right) (\varepsilon - \mu) \sum_{i,j}(\varepsilon) d\varepsilon \tag{3.5.2}$$

$$(\kappa_e)_{i,j}(\mu, \mathsf{T}) = \frac{1}{\mathsf{T}} \int \left(-\frac{\partial f_0(\varepsilon, \mathsf{T})}{\partial \varepsilon}\right) (\varepsilon - \mu)^2 \sum_{i,j}(\varepsilon) d\varepsilon \tag{3.5.3}$$

In equation (3.5.1)-(3.5.3), $f_0(\varepsilon, \mathsf{T})$ is the Fermi-Dirac distribution function, e and T are, respectively, the electron charge and the temperature and $\sum_{i,j}(\varepsilon)$ is the transport distribution function, defined as:

$$\sum_{i,j}(\varepsilon) = \frac{1}{V} \sum_{n,\vec{k}} \nu_i(n, \vec{k}) \nu_j(n, \vec{k}) \tau(n, \vec{k}) \delta_{\varepsilon - \varepsilon_{n,\vec{k}}} \tag{3.5.4}$$

where V is the volume of the solid, $\varepsilon_{n,\vec{k}}$ is the energy of an electron in the $n-th$ band at wave vector $\vec{k}$, $\nu_i(n, \vec{k})$ is the $i-th$ component of its velocity and the summation is over all bands and over the entire Brillouin Zone (BZ). $\tau(n, \vec{k})$ the relaxation time for electrons, depends on the electron state for each dispersing mechanism as well as on temperature. The transport coefficients were calculated with the BoltzWann post-processing code [32] included in the Wannier90 package [102]. For comparison with experiments, average values of the $\hat{\sigma}$, $\hat{S}$ and $\hat{\kappa_e}$ tensors were calculated as one third of the traces of the corresponding matrices.

3.6 Thermodynamic Properties

Phonon transport properties

A phonon is a quantized mode of vibration occurring in a rigid crystal lattice such as atomic lattice of a solid. Phonons play an important role in many of the physical properties of solids suchas thermal

and electrical conductivity. In addition, vibrational properties of a crystal determine a wide range of macroscopic behaviour i.e specific heat, sound velocity and infrared and Raman absorption [103]. The problem of lattice dynamics is to find the normal modes of vibration of a crystal. It seeks to calculate the energies (or frequencies, ω) of the phonons as a function of their wave vector. Even if the total energy of a structure can be minimized, its stability cannot be assured hence phonon calculation is done to provide a rigorous test for stability of a given structure.

Using an *ab initio* approach, we can calculate the vibrational frequencies of a material using either a linear response method or a finite displacement method. The mathematical theory involved is presented in Apendix D. A high thermal conductivity is required in order to remove any accumulated heat in thermoeletric devices, a mechanism associated with phonon-phonon scattering [104]. Phonon-phonon scattering is an intrinsic scattering mechanism that dominates the behaviour of the lattice thermal conductivity, κ_l, for semiconductors [105].

It is well known that the application of a material is closely related to its thermal transport properties. At equilibrium, a crystal is dynamically stable if its potential energy always increases against any combinations of atomic displacements. When an atom in a crystal is displaced, the forces on all atoms in the crystal change. Analysis of the forces associated with a systematic set of displacements provides a series of phonon frequencies. In the harmonic approximation, this is equivalent to the condition that all phonons have real or positive frequencies. Very low-frequency modes can be associated with phase transformations. The presence of negative or imaginary frequencies indicates dynamical instabilities, hence phonon dispersion curves can also help us gauge dynamical stability of a material [4].

3.6.1 Electrical and Electronic transport properties

It is desirable for thermoelectric materials to have high valley degeneracy in a very sharp band structure [106]. To calculate the Band structure, a self-consistent calculation run was performed to get the charge density, and then fixing the charge density, thereafter a non-self consistent run at desired K-path (see Figure (4.1)) is performed to get the band structure. For an extensive literature the reader is directed to [107, 92, 93]. The DFT calculated bands are in many cases found to be in qualitative agreement with experimentally measured bands, in particular, the band shape is typically well reproduced by DFT. The bandgaps may be underestimated or overestimated depending on the exchange correlation functional. It has been reported that DFT seems to systematically underestimate by about 30-40% the band gap in insulators and semiconductors [108]. The central problem in DFT is how to treat the exchange-correlation energy with a view to correctly calculating the material properties. In principle, if the exact exchange-correlation energy is known, the exact ground state energy and density of the particle can be found accurately. Armed with this knowledge we used different functionals, including the modified BeckeJohnson meta-GGA exhange functional (mBJ) [109, 110]. These semi-empirical meta GGA functional has been constructed to give accurate band structure of insulators and semiconductors and had been used in this work to obtain accurate bandgaps for these compounds. Further insight into the electronic structure is gained by plotting the Fermi surface of the compounds.

3.6.2 Femi Surface

The Fermi surface separates occupied electronic states from empty ones. Fermi surfaces are important for characterizing and predicting the thermal, electrical, magnetic, and optical properties of crystalline metals and semiconductors. They are closely related to the atomic lattice, which is the underlying

feature of all crystalline solids, and to energy band theory, which describes how electrons are distributed in such materials. According to band theory, electrons in a solid lie within either valence bands, where they are bound into position, or conduction bands at higher energy, where they are free to move. Each electron has a specific energy within a band, which can be related to its momentum [111]. At absolute zero (-273.15 ^{o}C, or -459.67 ^{o}F), however, the energy may not exceed a value called the Fermi energy, which therefore divides allowed electronic states from those that cannot be occupied. To represent this, physicists imagine an abstract three-dimensional momentum space where the coordinate axes are the x, y, and z components of momentum. Then the Fermi energy defines a volume in momentum space whose surface (the Fermi surface) separates occupied electronic states within the volume from empty ones without it [112]. Various experimental techniques are used to determine the Fermi surface in a given material, for instance, measurements of electronic behaviour in a magnetic field. The shape of the Fermi surface reflects the arrangement of atoms within a solid and is thus a guide to the properties of the material. The Fermi surface is crucial in determining electrical, magnetic, and other properties and how they depend on direction within the crystal because at temperatures above absolute zero these electrons are raised above the Fermi energy and become free to move.

4

Computational Details

In this chapter, the methodology used in our calculation is explained. The Vienna Ab initio Simulation Package (VASP) [113] has been used to perform calculations of the structural and electronic properties of the binary compounds A_8Sn_{46-n} (n = 0,2) (A = K, Rb, Cs). The projector-augmented wave formalism (PAW) implemented in the package was used to represent the valence electrons [93]. For all calculations that are related to the structural and electronic properties, four separate approximations were used for the exchange correlation functions, viz.: the local density approximation (LDA) [114], the Perdew, Burke, and Ernzehof (GGA-PBE)[115], the modified GGA-PBE for solids (PBEsol) [116] and the modified BeckeJohnson meta-GGA functional [109]. In order to capture the dispersion interaction between atoms, absent from typical DFT functionals, the Thatchenko-Scheffer method (vdW-TS) [117] was used. We have used a kinetic energy cutoff of 500 eV for the plane wave basis set, and the energy convergence criterion was chosen to be 10^{-6} eV. The Hellmann-Feynman forces on each ion were less than 0.02 eV $\mathring{A}^{-1}$ and the Brillouin zones of the unit cells were represented by the Monkhorst-Pack special k-point scheme using $4 \times 4 \times 4$ grid meshes for our compounds. The Boltzmann's transport equations will also be discussed as a bridge connecting calculated electronic structure to the thermoelectric transport properties of a material. How we combine *ab initio* MD and lattice dynamics to study the normalized phonon total density of state of the type-I clathrate, will also be resolved. I shall also explain how phonon dispersion relations have been calculated from its lattice dynamics.

4.1 Geometry Optimization and Structural Properties

The exchange-correlation energy (XC) is a fundamental issue in density functional theory (DFT). It is normally approximated in the form of local density approximation [LDA] or generalized gradient approximation [GGA] with Perdew-Burke-Ernzerhof [PBE] version of GGA being the most commonly used. The chronic over-binding of the LDA [118] which has been shown to lead to underestimation of equilibrium properties by about 1%, can be overcome by using the PBE functional even though it usually overestimates equilibrium properties by about the same amount [119]. The structural, electronic and phonon band structures for A_8Sn_{46-n} for (n = 0,2), have been calculated with first principles methods.These optimized equilibrium structures are the starting points for our calculations of the vibrational modes of these compounds. For the molecular dynamics calculation we did an equilibration test by using the experimental structural parameters. For further details, see section (4.5).

4.2 Electronic Density of States

It is possible nowadays to study the energetics and the electronic structure of many-electron systems by performing fully *ab initio* computations, that is, by solving the quantum-mechanical equations for the system under consideration without any use of empirical parameters, for a meaningful comparison with experiment or even for accurate predictions of quantities not yet accessible experimentally. Among the existing *ab initio* schemes, the local-density approximation (LDA) to density-functional theory (DFT) [120] has proven to yield reliable results, at an acceptable computational cost, the electronic ground-state properties of complex crystalline systems [121]. Within DFT, the many-body problem of interacting electrons is reduced to a system of single particle Schrødinger equations [114], which must be solved self-consistently (SCF, for self-consistent-field). Electron-electron interactions are fully included by adding to the Hartree potential an exchange-correlation term, which is a functional of the charge density. In the LDA, this functional [114] is reduced to a function of the local charge density which has been calculated accurately and interpolated using a parametrized form [122]

Within the semiclassical model we assume that we know the electronic structure of metal, which determines the energy band as a function of the wave vector. The aim of the model is to relate the band structure to the transport properties. A useful concept in analyzing the band structure of solids is the density of states as a function of the energy [123]. The density of states $N(E)dE$, defined as the number of states per volume Ω of the solid in the range E and E+dE [124], was analysed for our compounds. We used the rigid band approximation theory to describe the electronic structure. We compared the electronic band structure of the compounds to the hypothetical pure Sn_{46}, by looking at the band profiles. A comparison of the total density of states (DOS) and the partial density of states (PDOS) of the compounds was again carried out by analysing their profiles.

We extend our discussion of the electron dynamics in these compounds by looking at the electron effective mass m^*. The mass m^* is inversely proportional to the curvature of the band. The effective mass of electron m_e^* was calculated from the band structure near the conduction band minimum. The diagonal elements of the effective mass tensor m_e^* for the electrons near the conduction band bottom are calculated using the following relation:

$$\frac{1}{m^*_{i,j}} = \frac{\partial^2 E(k)}{\hbar^2 \partial(k_i k_j)} \tag{4.2.1}$$

For the diagonal elements, we have:

$$\frac{1}{(m_e^*)_{xx}} = \frac{\partial^2 E(k)}{\hbar^2 \partial(k_{xx}^2)} \tag{4.2.2}$$

, similar to

$$\frac{1}{(m_e^*)_{yy}} = \frac{\partial^2 E(k)}{\hbar^2 \partial(k_{yy}^2)} \tag{4.2.3}$$

and

$$\frac{1}{(m_e^*)_{zz}} = \frac{\partial^2 E(k)}{\hbar^2 \partial(k_{zz}^2)} \tag{4.2.4}$$

Therefore, the effective mass of the electron is evaluated by fitting the electronic band structure near the bottom to a parabolic function [125, 126].

4.3 Electronic Bandgap with mBJ Functional

Bandgap is a crucial property of semiconducting materials for it is related to the optical and electronic characteristics. However precise determination of band gaps using DFT calculations is still challenging. The modified BeckeJohnson meta-GGA exhange functional [110] (TB09) is a semi-empirical functional constructed for giving an accurate band structure of insulators and semiconductors. It is not possible to generate transferable pseudo-potentials since it only works for solids and not for atoms (it is not size consistent). In this work we used the mBJ to improve the band gaps calculated [109, 110].

4.4 Lattice Dynamics

Traditionally, phonon dispersion relations have been calculated by lattice dynamics. This involves proposing an analytic model for the interactions between atoms, evaluating the force constants between atoms, constructing the dynamical matrix at a given point in the Brillouin zone and diagonalizing it. In the *ab initio* method the analytic model is replaced by a full quantum mechanical electronic structure calculation of a supercell of N atoms. A wide variety of physical properties of solids can be investigated from their lattice-dynamical behaviour. Since the electron states around the Fermi level have an important effect on the thermoelectric (TE) properties of the binary clathrates, we proceed to calculating the phonon total and partial density of states for our compounds. Heat is carried by phonons and electrons in type-I Sn clathrates, so that $\kappa_{tot} = \kappa_l + \kappa_e$, where κ_l and κ_e are the phonon and electron contributions, respectively. It has been reported that in metals or degenerately-doped semiconductors, κ_e is the dominant heat carrier due to large concentration of free carriers [127]. We used the phonopy code [4] to evaluate these claims and other properties of interest. Steps in our calculation are presented in references [100] and [101]. Further analysis of the vibrational bands were carried out, by assigning the phonon modes to irreducible representations of their space-group type. We then analysed the phonon eigenvector, which has information of the symmetry of the mode, and then examined the character of the modes and details of their symmetry from the irreducible representations.

4.4.1 Transport properties

Presented in this work is thermal property calculations, with a BoltzWann code [32] to evaluate electron transport properties in a semiclassical formalism using a maximally-localized wannier function (MLWF) basis to interpolate first-principles plane-wave (PW) results. Thermal and electrical transport are currently being intensively studied in the literature, as their evaluation is critical to the thermoelectric efficiency of a material [98, 99]. We first perform a self-consistent first principles calculation on the system in order to obtain a set of Bloch energy bands [92, 93] from which maximally-localised wannier functions are then constructed. Calculation of the Bloch states $|u_{nk}\rangle$, where u_{nk} is the set of Bloch functions obtained at each k-point, is performed using density functional theory in the LDA approximation [114]. We computed Bloch states and the overlaps from ground state density and the maximally-localised Wannier functions (MLWF) on a $4 \times 4 \times 4$ mesh [102].

MLWF's are calculated using wannier90 program [102] and the band structure is plotted along the $\Gamma - X - S - Y - \Gamma - Z - U - R - T - Z - Y - T - U - X - S - R$ path. The conduction band is separated from the valence band by an (LDA) band gap of $\approx$ 0.1 eV. In order to obtain wannier functions (WFs) that are able to reproduce the lowest-energy conduction states as well as disentagling the valence band, we proceed as follows; We note that only a few energy $k_B T$ around the Fermi energy

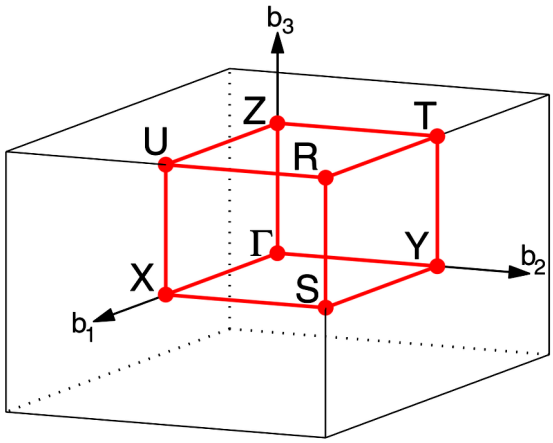


Figure 4.1: Special K-path considered [2]

are relevant for transport properties, hence we carefully selected the relevant bands when calculating the WFs. We also choose a frozen energy window E_{froz} roughly above the bottom of the conduction band, which is sufficient for our calculations. We thereafter calculated the MLWFs using interactive minimization algorithm of Wannier90 [102], employing atom-centred Gaussian-type orbitals with the number of Wannier and bands for the calculation set at a reasonable number of bands [102]. Once the MLWFs are obtained, we then proceed to using them as a basis set to interpolate band velocities and calculate the transport properties using the BoltzWann code [32]. The bands were interpolated on a $40 \times 40 \times 40$ mesh and the transport distribution function (TDF) calculated using a relaxation time of 10 fs for the system. (TDF is the single function that describes the interplay among the three key thermoelectric components of electyrical conductivity, thermopower and thermal conductivity). The relaxation time of 10 fs was chosen from experimental results of Ge-based clathrates [128]. We could safely use this value as our system contains a group 14 element (Sn) which is common to all the binary systems studied in this work. This simple time approximation is often adopted in all first-principles calculations and often turns out to be a good approximation for bulk materials [129, 130].

In calculating the transport properties, the Fermi-Dirac function $f_0(\varepsilon, \mathrm{T})$ is required (see Equations (3.5.1)-(3.5.3)). This function depends on the chemical potential μ. The position of chemical potential (μ) plays an important role with regard to the transport properties. The position of μ in the band structure determines which electrons in the valence or conduction band take part in the electronic transport (4.2), commonly used as a criterion for noting both the conductivity and the Seebeck coefficient.

4.5 Molecular Dynamics Simulation

The combination of *ab initio* MD and lattice dynamics will be used to study the normalized phonon total density of state of the type-I clathrate. We start our calculation by performing an equilibration test for the compounds, $A_8Sn_{44}\square_2$) (A = Cs, Rb and K). The low temperature phase has been reported to have high ordering of vacancies and as such we would need supercells to correctly describe the system with the ordered vacancies. The experimental configuration of the compound was used to eliminate any discrepancy in our simulation. Molecular dynamics (MD) simulations were then performed at the temperatures which match those of [30] inelastic neutron scattering (INS) data, used for the validation

of my simulations. All simulations, the NVT and NVE at 36000 steps at room temperature, were ran for approximately 36ps with a time step of 1fs, initially and latter increased to 60ps. Most of the simulation could not be completed up to 60ps and so my analysis was limited to 36ps. The MD spectra was then calculated using nMOLDYN [131] a MD simulations analysis programme designed for decomposition of neutron scattering spectra, while the magnitude spectra was obtained from the fast Fourier transform (FFT) of the trajectories. Decomposing the spectra is necessary because, we would then be able to asses the dynamics of the individual atoms of the compound separately. I then calculated the MD trajectories to obtain the simulated elemental spectra and vibrational frequencies in order to determine atomic dynamical correlations, as adopted elsewhere [90, 132]. The lattice dynamics calculations were then finally done to obtain the spectrum of the phonons and most importantly the phonon dispersion relation of the avoided crossing. The phonon dispersion curves were then plotted and the analysis of the rattling metal obtained is reported in subsection (5.4.3).

5

Results and Discussion

In this chapter we present the results of our calculations. Bandstructure calculations for the fully stoichiometric cubic A_8Sn_{46} (A = K,Rb or Cs) compounds show that they are metallic at the DFT level. We found that the guest atoms in the ideal cubic stoichiometric compounds Rb_8Sn_{46} and K_8Sn_{46} are dynamically unstable and all three stoichiometric compounds are stabilised by vacancy formation. We used the stoichiometric compounds for reference only in our structural analysis of the vacancy compounds.

The $A_8Sn_{44}\square_2$ (A = K,Rb or Cs) clathrates are small gap semiconductors and we investigated their structural, dynamic and electronic properties in details. According to experimental studies by Kaltzoglou *et al.* [85, 133] $Cs_8Sn_{44}\square_2$ and $Rb_8Sn_{44}\square_2$ have cubic symmetry (space group $Ia\bar{3}d$, Z=8) at room temperature. The structure adopts a $2 \times 2 \times 2$ type-I clathrate superstructure with vacancies in the Sn framework. For $Cs_8Sn_{44}\square_2$ and $Rb_8Sn_{44}\square_2$ there are reversible order-disorder phase transitions to a primitive cubic structure (space group $Pm\bar{3}n$, $Z = 1$) with a random distribution of vacancies at about 353 K and 363 K, respectively. In the low temperature phase the vacancies show long range order with the vacancies distributed along the 4_1 screw axis. Earlier reports [134, 21, 135, 133] suggested that the low and high temperature structures formed in space group $Pm\bar{3}n$ with a random distribution of vacancies around the 4_2 screw axis. However, Kaltzoglou *et al.* [85, 133] argue that the low temperature phase of $Cs_8Sn_{44}\square_2$ and $Rb_8Sn_{44}\square_2$ is stabilised by a higher ordering of the vacancies. In both phases the basic underlying conventional type-I clathrate structural units are retained. Computational resources constrained us to do our calculations for the $A_8Sn_{44}\square_2$ compounds in primitive cubic structures ($Z = 1$) at absolute zero and not at the correct experimental temperature. A $2 \times 2 \times 2$ superstructure ($Z = 8$) requires a large unit cell with 416 atoms (and 8 vacancies), a challenge beyond our available computational resources. The fully ordered structure that satisfies the composition of an electron precise Zintl phase used in our calculations, as described in subsection 2.1.3, is therefore hypothetical. It was noted that $Na_8Sn_{44}\square_2$ and $Li_8Sn_{44}\square_2$ compounds have not been synthesized, hence, I have restricted the calculations to these three $A_8Sn_{44}\square_2$ (A = K,Rb or Cs) known stable compounds.

The rest of the chapter is structured as follows: We start our investigation by optimising the lattice geometry using four separate exchange-correlation functionals, LDA, PBE, PBEsol and vdW-TS. Where available, we compare our results with experimental data and other calculations. We find that LDA works well for the type-I clathrates we are interested in and we use LDA for the rest of our calculations.

We then calculated the Phonon Bandstructure and Density of states. Detailed analysis of the phonon spectra of the A_8Sn_{46} and $A_8Sn_{44}\square_2$ compounds was carried out and carefully reported. We report

vacancy formation energies and confirm that vacancy formation stabilises the clathrate compounds. Next we report an analysis of the vibrational properties of the compounds.

Mode Grüneisen parameters at different temperatures are also presented and analysed. We performed lattice thermal conductivity and electronic transport properties calculations which are combined in thermoelectric figures of merit.

The electronic Bandstructures and densities of states of the compounds are also reported and results of the Fermi surfaces are equally presented to gain understanding on the electronic properties.

Anisotropic behaviour and effective carrier masses of this class of materials were again investigated and reported here. Finally, the thermoelectric properties of these compounds are reported starting with the Seebeck coefficients, followed by the lattice thermal conductivity and the electronic thermal conductivity. The calculated figures of merit of the three compounds, a signature of thermoelectric materials are also reported.

5.1 Equilibrium and Structural properties

5.1.1 Result for A_8Sn_{46}

For completeness, and to evaluate the performance of different exchange-correlation functionals for the clathrate compounds, we performed structural optimizations for the full stoichiometric type-I clathrate compounds, A_8Sn_{46} (A = K,Rb or Cs). In each calculation, we chose the experimentally reported structure [134] as our initial guess, and then minimized the total energy by allowing a full relaxation of the ionic positions, the cell shape, and the cell volume. These compounds crystallise in a cubic structure (space group $Pm3\bar{n}$) [41, 136] with the alkali atoms residing in the polyhedral cavities formed by the tetrahedrally bonded network of Sn atoms. The $Pm3\bar{n}$ cubic system is a high symmetry system with 48 rotation operations and therefore a computationally friendly system to work with. We optimised the ionic positions and the lattice geometry, yielding theoretical estimated lattice constants as presented in Table (5.1). The structural parameters obtained are compared with experiment [41, 136] and theory [67, 86] where available. Structural parameters from LDA compared well with previous studies [86]. The LDA values also compare well with experimental results for Cs_8Sn_{46}. All the considered exchange-correlation functionals overestimate the lattice constant for Cs_8Sn_{46} and K_8Sn_{46} relative to experiments. This is in agreement with previous LDA results [86] and consistent with theoretical results for other compounds reported in the literature [137, 138]. Similarly, our result for the lattice constatnt shows expected accuracy with the PBE functional, i.e., 0.08% and 5.5% difference, in comparison with previous theoretical studies and experimental results for K_8Sn_{46}). PBEsol gives a better estimate than PBE as expected [116], as, unlike other functionals, it recovers the exact condition of the gradient expansion for solids. PBEsol, however, is not expected to give good atomization energies [119]. There were no experimental data available to compare our results for Rb_8Sn_{46}.

The vdW-TS method takes into account variations in van der Waal's energy contributions of atoms due to their local chemical environment and are able to account for long range dispersion forces. From our results vdW-TS gives a better estimate of the volume compared to PBE and its modified version PBEsol as seen in Table 5.1. Of interest for our purpose is the cohesive energy which is negative for all the functionals used, suggesting that the compound may be stable enough to perform molecular dynamics calculations in order to gain insight into what may be responsible for the reported low thermal conductivity of the vacancy systems. However, the initial configuration we used in the structural energy

minimisation procedure is cubic (space group Pm3$\bar{n}$) and the forces on the guest atoms at the centres of the cages are zero due to symmetry. During the numerical relaxation, forces on atoms are used to locate the minimum energy configuration. Also, the guest atoms remain at the centers of the cages for the stoichiometric compounds. We shall examine the potentials that the "encaged" atoms experience in more detail in Section 5.4.3.

Table 5.1: Structural parameters for the cubic A_8Sn_{46} compounds using different exchange-correlation functionals.

Compound	Functional	a(Å)	V_0 (Å^3 /atom)	B_0 (GPa)	B_0'	E_{coh}(eV/atom)
Cs_8Sn_{46}	LDA	12.34	34.81	35.06	3.74	-3.56
	PBE	12.75	38.28	28.49	3.88	-2.98
	PBEsol	12.49	36.05	32.75	3.52	-3.34
	vdW-TS	12.37	35.06	44.53	4.5	-3.57
	LDA(others) [86]	12.37	34.60	29.03	3.70	-9.80
	Experiment [41]	12.14	32.77	-	-	-
Rb_8Sn_{46}	LDA	12.28	34.28	29.07	4.00	-2.96
	PBE	12.69	37.90	26.41	4.40	-2.96
	PBEsol	12.44	35.69	31.21	2.92	-1.23
	vdW-TS	-	-	-	-	-
K_8Sn_{46}	LDA	12.26	34.11	32.33	3.95	-3.47
	PBE	12.65	37.53	29.69	3.50	-2.95
	PBEsol	12.41	35.39	29.50	3.34	-1.18
	vdW-TS	12.11	32.89	47.41	4.63	-1.75
	Experiment [67]	12.03	-	-	-	-
	PBE(others) [136]	12.03	-	-	-	-

5.2 Result for $A_8Sn_{44}\square_2$

The $A_8Sn_{44}\square_2$ clathrates have been structurally characterized as temperature dependent clathrate hydrates [36]. As discussed in the introduction to this chapter, the low and high temperature modifications of $A_8Sn_{44}\square_2$ [85, 133, 53] crystallise in cubic structures with the alkali atoms residing in the polyhedral cavities formed by the tetrahedrally bonded network of Sn atoms. Vacancies are formed at the Wyckoff 6c sites. Both phases have the underlying Pm$\bar{3}$n symmetry of the full stoichiometric compound, but the vacancies form a $2 \times 2 \times 2$ superstructure at room temperature and at high temperatures the vacancies are randomly distributed. Constraints on computational resources prevented us from examining the low temperature $2 \times 2 \times 2$ superstructure and the random nature of the vacancies at high temperatures.

In the A_8Sn_{46} prototype structure the Sn atoms occupy $6c$ $(\frac{1}{4}, 0, \frac{1}{2})$, $24k$ $(0, y_k, z_k)$ and $16i$ (x_i, x_i, x_i) while the guest atoms occupy $6d$ and $2a$ sites [86, 85, 133, 53]. Experimental data [134, 85, 133, 53] suggest that two vacancies per unit cell are formed in the framework at the $6c$ sites. The $6c$ sites are at the vertices shared by two hexagons which are perpendicular to each other, as can partly be seen in Fig. (5.2). In the high temperature phase the vacancies are randomly distributed [86, 85, 133, 53]

and the structure is not periodic. In order to make a computational study of the vacancy systems feasible, we follow the suggestion by Myles*et al.* [86] and fix the vacancies at two of the $6c$ sites in an ordered structure. Within the ordered structure assumption, there are only two non-equivalent vacancy pair configurations. One configuration places the vacancy pair on the same hexagonal $6c$ ring, and the second configuration places the two vacancies on different hexagonal rings. The most stable configuration is the second, which corresponds to vacancies created by removing one Sn atom from the lower hexagonal ring shown in Fig. (5.2)b and one from the middle hexagonal ring.

The introduction of vacancies reduces the symmetry of the system dramatically from $Pm3\bar{n}$ to $Ama\bar{2}$, and the number of symmetry operations from 48 to 4. Combined with a 'large' volume unit cell, this is a computationally demanding system to work with.

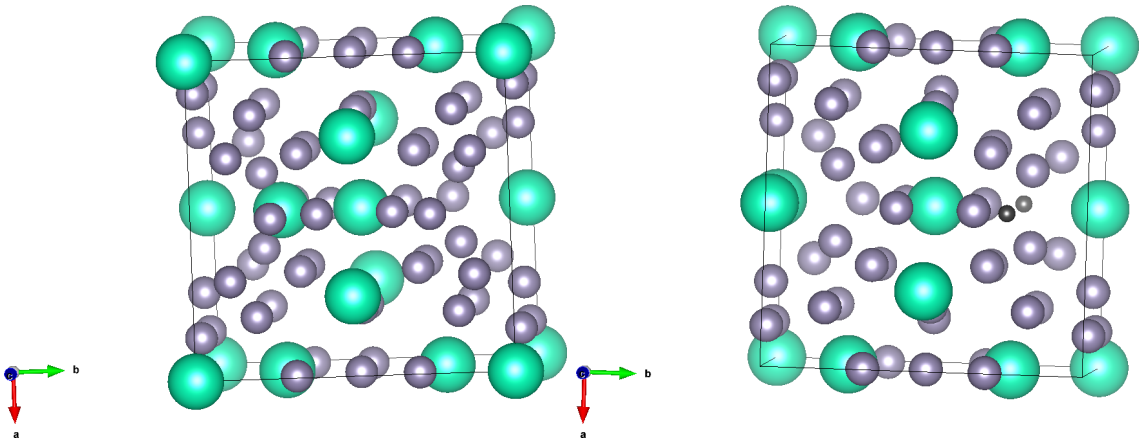
In order to obtain relaxed structures, we optimised the ionic positions and the lattice geometry, yielding theoretical structural parameters similar to the experimental high temperature phase as revealed in Table (5.2). We performed calculations on $A_8Sn_{44}\square_2$ using three exchange-correlation functionals. Results from LDA functional compared well with previous LDA studies [86] (between 0.5% and 1.4% difference from previous LDA studies). LDA also compares well with experimental results for $Cs_8Sn_{44}\square_2$. We expect LDA to underestimate the lattice constant when compared with experiment and PBE to overestimate it [116]. This is exactly what we found for the systems where experimental data are available for comparison. We however note that the LDA tends to underestimate the lattice constant of $A_8Sn_{44}\square_2$ as compared to overestimation in A_8Sn_{46} compounds. These behaviour of the LDA could be attributed to the partial occupancies of the framework in $A_8Sn_{44}\square_2$ [85, 139]. PBEsol gives lattice constants somewhere between the LDA and PBE values. Our PBE results are comparable to other PBE calculations [67]. The difference in values may be due to the artifacts of the calculations performed. We note that PBEsol [116] gives a better prediction when compared to the experimental data for the three compounds: 1775 $Å^3$ (1789 $Å^3$) [86] for $Cs_8Sn_{44}\square_2$, 1759 $Å^3$ (1750 $Å^3$) for $Rb_8Sn_{44}\square_2$ [134], and 1743 $Å^3$ (1741 $Å^3$) [134] for $K_8Sn_{44}\square_2$.

Recall that our calculations are done at absolute zero and that comparison with experiment is not strictly justified when we are interested in high temperature phases. In addition, we use an approximate configuration for the structures of interest. Our results suggest, however, that we have reasonable structural parameters for further studies. We need energetically stable equilibrium configurations for phonon and lattice thermal conductivity studies and our optimised structures will be used in the calculations reported in the rest of this chapter.

Of particular interest for our purpose is the cohesive energy which is sufficiently negative for all the functionals used, suggesting that the compounds may be stable enough to perform molecular dynamics calculations in order to gain insight into the dynamics of the atoms in the system.

LDA gives the highest magnitude of the cohesive energy for the three approximations we tested. Based on this, we chose LDA for the rest of our calculations.

Representative relaxed structure of the compounds are shown in Figure 5.1.



(a) (b)

Figure 5.1: Structure showing covalently-bonded framework atoms forming a polyhedra with regular or distorted pentagonal and hexagonal faces, housing guest atoms (a) A_8Sn_{46} (A = Cs, Rb and K) (b) $A_8Sn_{44}\square_2$ (A = Cs, Rb and K) (Green spheres = Cs, Rb or K atoms, small silvery spheres = Sn atoms).

Table 5.2: Structural parameters for the cubic $A_8Sn_{44}\square_2$ compounds using different exchange correlation functionals.

Compound	Functional	a(Å)	V_0 (Å^3 /atom)	B_0 (GPa)	$B_0^{'}$	E_{coh}(eV/atom)
Cs_8Sn_{44}	LDA	11.97	33.01	37.61	5.73	-3.57
	PBE	12.40	36.68	23.90	5.65	-2.97
	PBEsol	12.11	34.14	32.08	4.91	-1.27
	LDA(others) [86]	12.03	33.56	32.40	5.90	-
	Experiment [85]	12.14		-	-	-
Rb_8Sn_{44}	LDA	11.94	32.75	35.56	7.07	-3.49
	PBE	12.34	36.14	26.15	6.79	-2.95
	PBEsol	12.06	33.82	29.76	5.72	-1.23
	Experiment [134]	12.05	-	-	-	-
K_8Sn_{44}	LDA	11.89	32.36	32.55	8.48	-3.48
	PBE	12.27	35.56	27.04	5.20	-2.95
	PBEsol	12.03	33.51	32.84	7.97	-3.37
	Experiment [134]	12.03	-	-	-	-
	PBE(others) [67]	12.59	-	-	-	-

5.3 Volume and Vacancy Formation

Volume expansion is observed on the substitution of the guest atoms in binary type-I Sn clathrates in this study, showing volume change in this order Cs > Rb > K from comparing Tables (5.1) and (5.2). The local bonding in the stoichiometric structures is tetrahedral, similar to that in the diamond structure. It should, however, be noted that the structures contain pentagonal rings of atoms, which makes the way in which constituent parts are interrelated or arranged quite different from that of the diamond structure. In the compounds studied, the guest atoms, Cs, Rb and K, occupy two sites as shown in Figure (5.2)(b): the Wyckoff $2a$ sites in the dodecahedra and the 6d sites in the tetrakaidecahedrons.

The Sn framework atoms in $A_8Sn_{44}\square_2$ occupies three crystallographic sites $6c$, $16i$, and $24k$. The $6c$ sites are bound to four $24k$ sites; the $16i$ sites, to three $24k$ sites and one $16i$ site; and the $24k$ sites, to one $6c$ site, two $16i$ sites,and one $24k$ site as shown in Figure (5.2)a. In the vacancy structures the ideal tetrahedral bonding is distorted around the vacancies.

Our focus is on the vacancy structure which, from experiment, is a semiconductor with narrow bandgap. Using the Zintl-Kleim concept, we summarize the concept of the two principles *viz.* (i) that a full charge transfer takes place between anionic and cationic and (ii) that an electron octet is realized by each atom. We proceed as follows: Given that the compounds $A_8Sn_{44}\square_2$ (A=Cs, Rb and K) has two framework

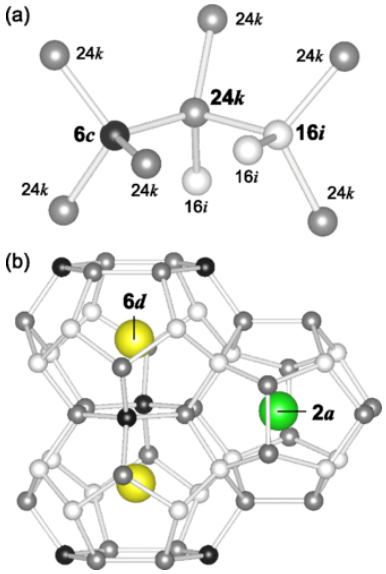


Figure 5.2: Source: [3] (a)Tetrahedral bonds of framework atoms, and (b) guests in dodecahedral and tetrakaidecahedral cages for type-I clathrates.

vacancies at the $6c$ site, each surrounded by four Sn atoms. These vacancies are located in different hexagonal rings (one in the lower hexagonal ring in Fig. (5.2) and a second in the middle hexagonal ring), with the separation ≈ 0.6123 Å of the lattice constant. The total energy of vacancy formation for the clathrates is calculated as shown below. According to the Zintl concept subsection (2.1.3), the framework atom Sn, should be electroneutral in the absence of guest atoms. In this work, the removal of a Sn atom compensates four excess electrons. We therefore created $d = \frac{8n}{4}$ vacancies in the Sn framework following the order in reference [134]. The energetics of the reaction is given by

$$Cs_8Sn_{46} \equiv Cs_8Sn_{44}\square_2 + 2Sn_\alpha, \tag{5.3.1}$$

Taking the total energy of vacancy formation of the vacancy in A_8Sn_{46} as E_v, we have

$$2E_v = (44+8)E^0(Cs_8Sn_{44}\square_2) + 2E^0(Sn_\alpha) - (46+8)E^0(Cs_8Sn_{46}). \tag{5.3.2}$$

where E^0 ($Cs_8Sn_{44}\square_2$), E^0 (Cs_8Sn_{46}) and E^0 (Sn_α) are, the binding energies for $Cs_8Sn_{44}\square_2$, Cs_8Sn_{46} and elemental Sn (Sn_α) respectively. We find that E_v is equal to -1.18, -1.26 and -1.27 eV/vacancy for $Cs_8Sn_{44}\square_2$, $Rb_8Sn_{44}\square_2$ and $K_8Sn_{44}\square_2$, respectively. The negative value indicates that the vacancy formation is favourable for the compounds from A_8Sn_{46} to $A_8Sn_{44}\square_2$ (A = Cs, Rb and K) and shows that vacancy formation stabilises the ordered vacancy structure, consistent with the experimental observation that vacancy formation stabilises the synthesised structures [135]. The role that the vacancies play in tuning the properties of these compounds is further investigated in our study of the vibrational dispersion relation and is covered in the next section.

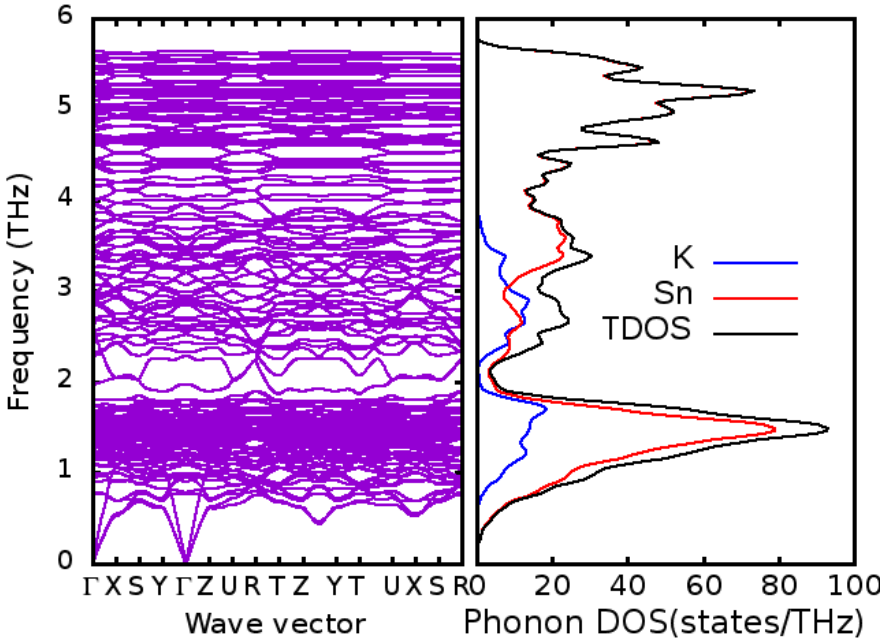


Figure 5.3: Plots of (left) Calculated phonon band dispersion for $K_8Sn_{44}\square_2$ along high symmetry directions (refer to the Brillouin zone in Figure (4.1) (right) Guest atom (K) contribution to the total density of states TDOS.

5.4 Phonon Bandstructure and Density of States

As noted in the introduction, Tse *et al.* [55] calculated the phonon band structure for Cs_8Sn_{46}, which, in the absence of a similar calculation for Cs_8Sn_{44}, has provided the starting point for interpreting the experimental phonon properties of Cs_8Sn_{44} and similar compounds [30].

In this section we discuss the calculated phonon dispersion relation and the phonon partial density of states for the vacancy structures. The unit cell of the fictitious ordered compound is cubic, but with a low symmetry. There are 52 atoms and two vacancies per unit cell. We used a finite displacement method to calculate the phonon band structure. The reader is refered to Appendix D and [96, 140, 141] for details on the method used.

The phonon bandstructures of the three studied compounds are presented in Figures (5.3), (5.4) and (5.5) for $K_8Sn_{44}\square_2$, $Rb_8Sn_{44}\square_2$ and $Cs_8Sn_{44}\square_2$ respectively. The acoustic modes go to zero at the Γ point, while all the other phonon dispersion curves remain positive throughout the Brillouin zone. This confirms that the $A_8Sn_{44}\square_2$ compounds are dynamically stable. Several flat bands can be clearly identified in the low frequency region near 1 THz and 2 THz for $K_8Sn_{44}\square_2$, 0.5 THz and 2 THz for $Rb_8Sn_{44}\square_2$ and 0.5 THz and 2 THz for $Cs_8Sn_{44}\square_2$ often indicative of the optical phonon branches.

Also from Figures (5.3), (5.4) and (5.5) we note that, although occasionally the acoustic branches cut across the flat, localised, bands, there are strong interactions between the phonon bands leading to the deflection of the acoustic branches at several places. Similarly we observe two high density regions for the three compounds. The phonon dispersion curves show several flat optical vibrational bands above the acoustic phonon branches in the region between 1 THz and 2 THz and at the top of the optical bands in the region between 5 THz and 6 THz for $K_8Sn_{44}\square_2$, between the 1 THz and 2 THz and at the

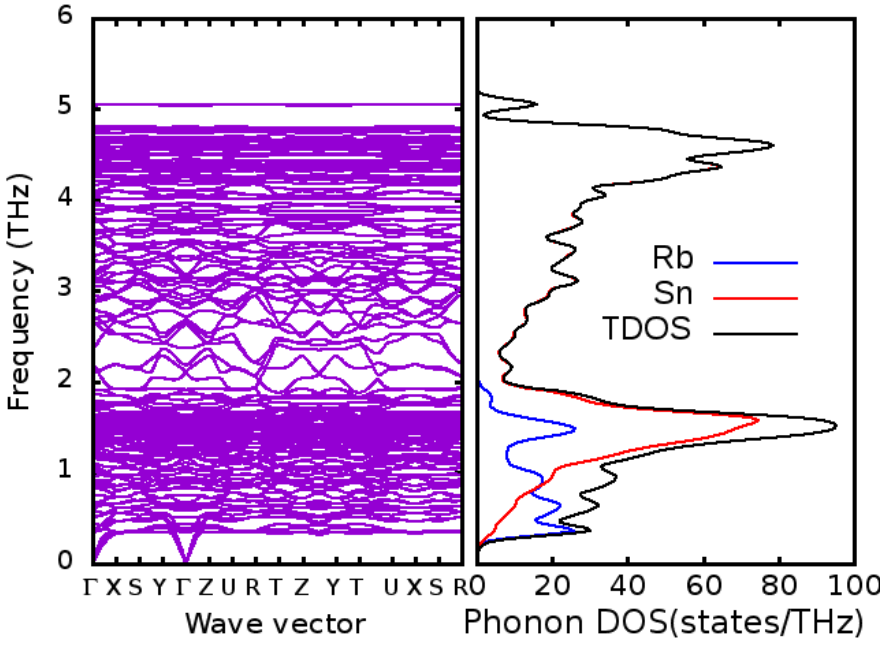


Figure 5.4: Plots of (left) Calculated phonon band dispersion for $Rb_8Sn_{44}\square_2$ along high symmetry directions (refer to the Brillouin zone in Figure (4.1)) (right) Guest atom (Rb) contribution to the total density of states TDOS.

top of the optical bands in the region between 4 THz and 5 THz for $Rb_8Sn_{44}\square_2$ and between the 1 THz and 2 THz and at the top of the optical bands in the region between 4 THz and 6 THz for $Cs_8Sn_{44}\square_2$. The presence of a significant optical mode is indicative of low thermal conductivity according to heat transport theory [8, 142, 143].

The structure of the low-energy optical modes we obtained is similar to that reported for Cs_8Sn_{46} by Tse et al. [55], with slight variation. In particular, Tse *et al.* [55] reported a lowest optical mode at 1.9 THz (at the Γ point) which was strongly dispersive in the X M R Γ direction indicative of strong coupling to the cage modes. They predicted even stronger bonding between the Cs guest atoms and the eight three-bonded Sn atoms sharing the two vacancy sites in the $Cs_8Sn_{44}\square_2$ unit cell. Our report shows lowest optical modes between 1 THz and 2 Thz, but more strongly dispersive for $K_8Sn_{44}\square_2$.

The acoustic mode cut-off, taken as the highest frequency of the lowest phonon band at each point in the reciprocal Brillouin zone, for $K_8Sn_{46}\square_2$, $Rb_8Sn_{44}\square_2$ and $Cs_8Sn_{44}\square_2$ are approximately 0.61 THz, 0.34 THz and 0.55 THz, respectively. For $Rb_8Sn_{44}\square_2$ and $Cs_8Sn_{44}\square_2$ there is a sharp peak in the vibrational density of states projected onto the guest atoms at the acoustic mode cut-off, with some guest atom density of states in the lower frequency acoustic mode region. For $K_8Sn_{46}\square_2$ there is no meaningful guest atom DOS in the whole of the acoustic region. This suggests that the guest atoms couple to the acoustic modes for $Rb_8Sn_{44}\square_2$ and $Cs_8Sn_{44}\square_2$, but there is negligible contribution to the acoustic modes by the guest atom in $K_8Sn_{44}\square_2$.

For all three compounds, the guest atom modes overlap in frequency with the lower peak in the optical mode spectrum of the framework.

The acoustic mode cut-off for the pristine Sn framework only, is about 1.3 THz. The introduction of the vacancy-guest atom complexes therefore have a significant effect on the suppression of the acoustic

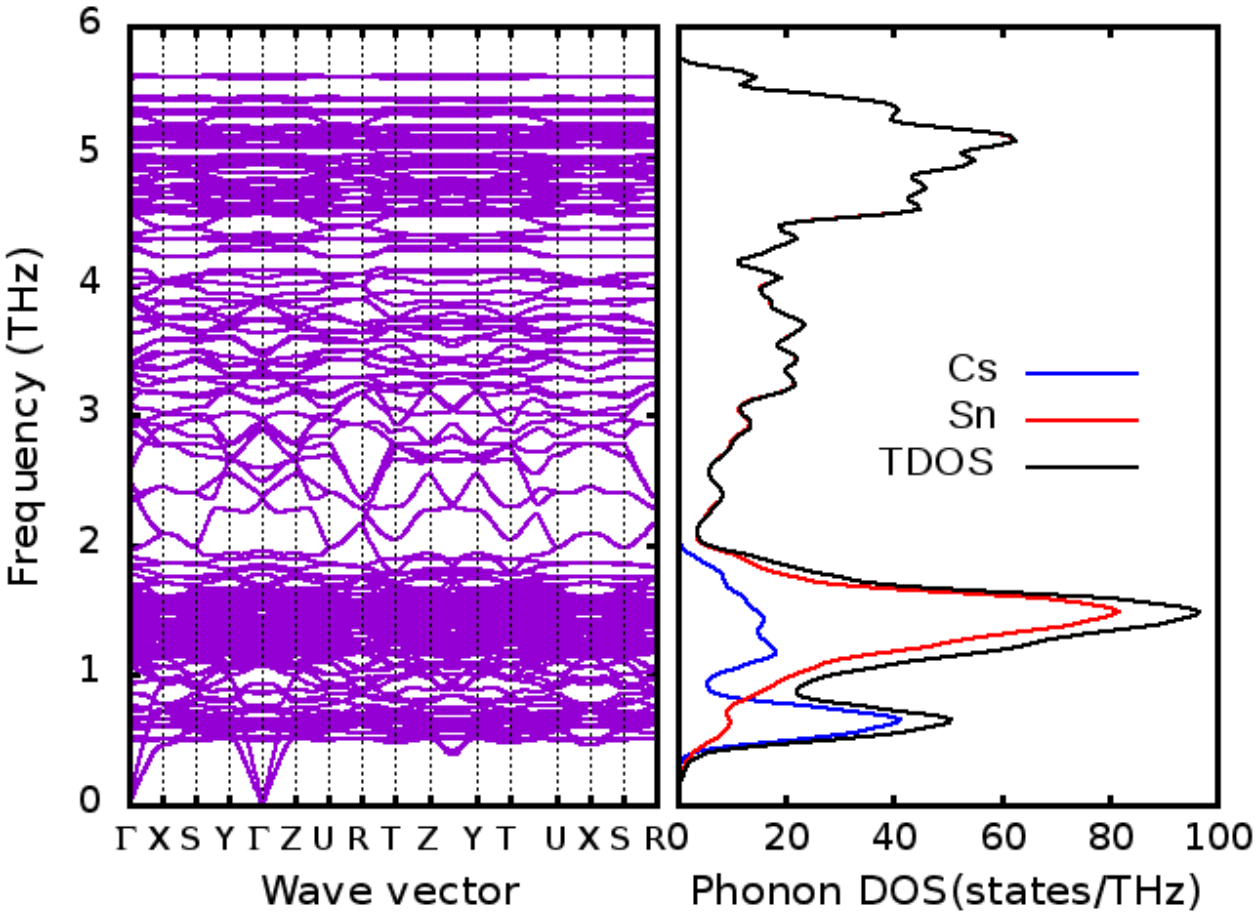


Figure 5.5: Plots of (left) Calculated phonon band dispersion for $Cs_8Sn_{44}\square_2$ along high symmetry directions (refer to the Brillouin zone in Figure (4.1).) (right) Guest atom (Cs) contribution to the total density of states TDOS.

modes to lower frequencies.

5.4.1 Detailed analysis of the phonon spectra of the A_8Sn_{46} and $A_8Sn_{44}\square_2$ compounds

In order to develop further understanding of the effect of the introduction of vacancies on the dynamic stability of the vacancy compounds, we did a comparative analysis of the A_8Sn_{46} and $A_8Sn_{44}\square_2$ (A = Cs, Rb, K) phonon spectra. Our calculations show that the stoichiometric A_8Sn_{46} compounds are dynamically unstable. In all the phonon spectra we find imaginary eigenfrequencies which cannot be accounted for by numerical inaccuracies of the calculations. It is not unusual in phonon calculations to find negative eigenvalues of the dynamical matrix [4], which are a consequence of numerical errors, or which may be associated with the limited range over which interactions between atoms are taken into account, something we are forced to do given limited computational resources. We have already pointed out that the introduction of vacancies stabilise the A_8Sn_{46} compounds energetically, but, in addition, we find that the A_8Sn_{46} compounds are inherently unstable against small vibrations. This is especially relevant for K_8Sn_{46} and Rb_8Sn_{46} and less so for Cs_8Sn_{46}. The instability seems to be driven by the

guest atoms.

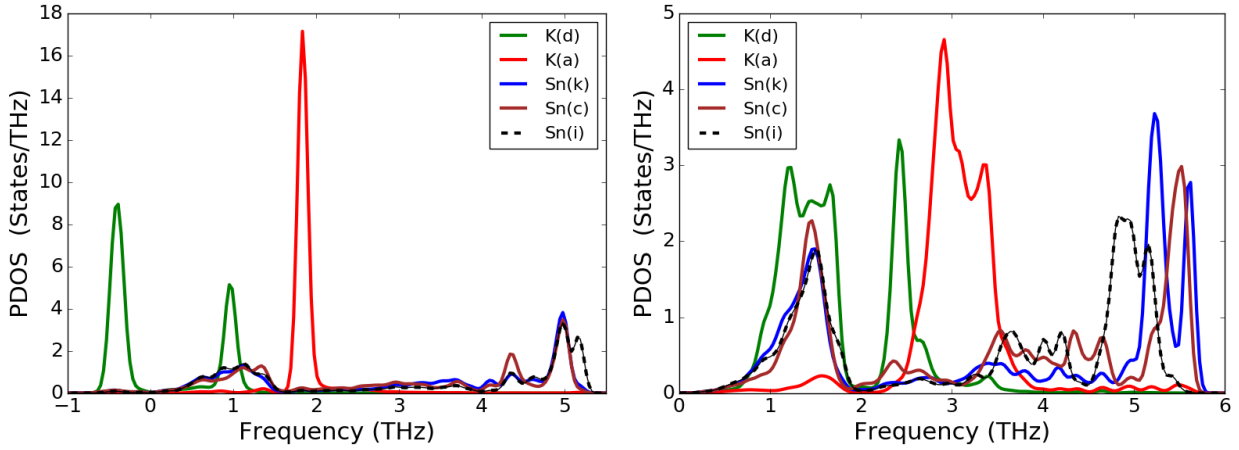


Figure 5.6: Projected density of states for the stoichiometric system K_8Sn_{46} (a) and for the vacancy system $K_8Sn_{44}\square_2$ (b). Densities of states are projected onto the atoms at the two inequivalent K guest atom sites and onto the three inequivalent Sn sites for K_8Sn_{46}, and onto the corresponding atoms sites for $K_8Sn_{44}\square_2$.

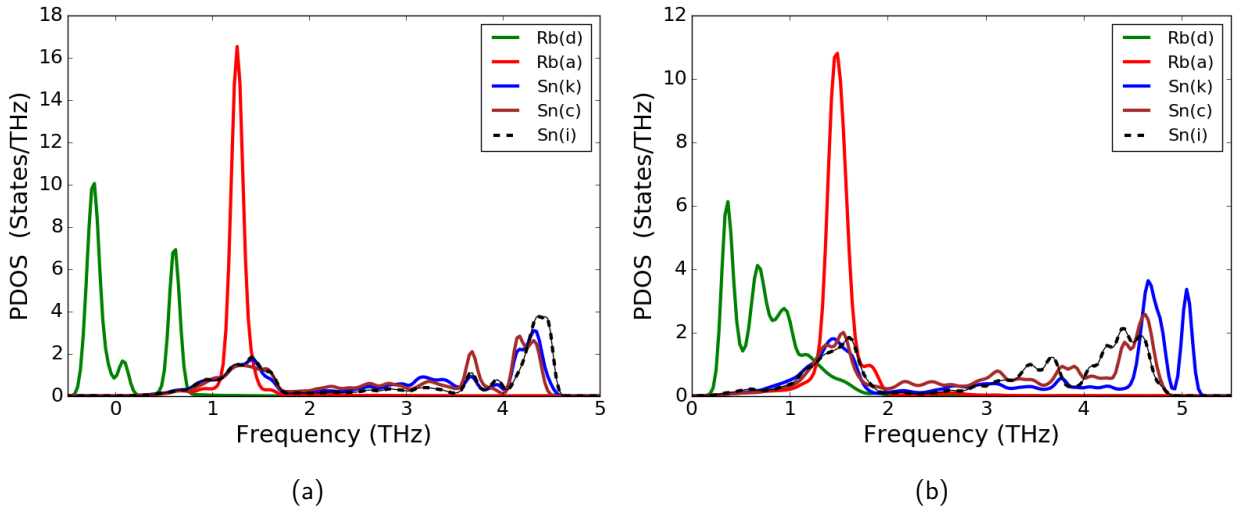
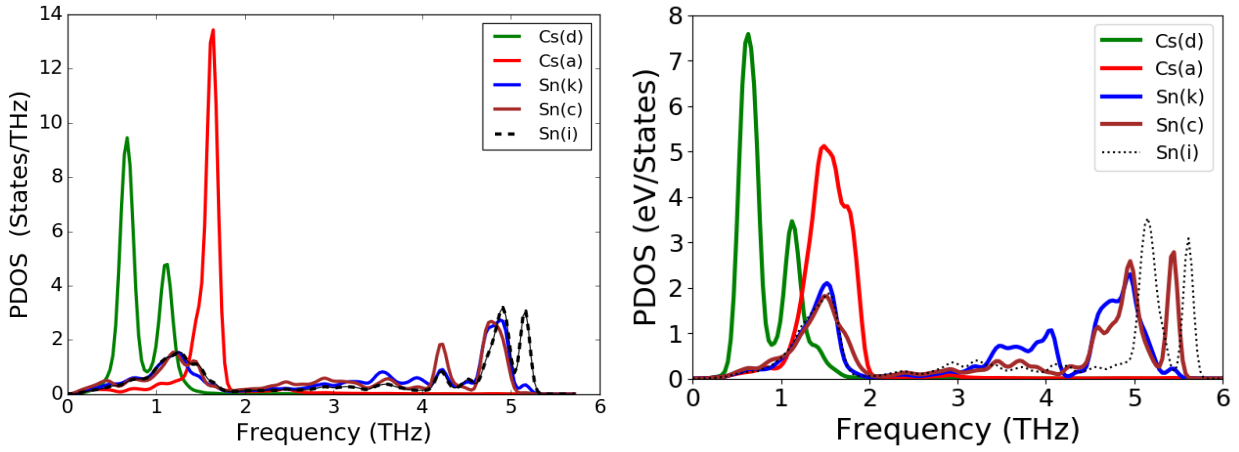


Figure 5.7: Projected density of states for the stoichiometric system Rb_8Sn_{46} (a) and for the vacancy system $Rb_8Sn_{44}\square_2$ (b). Densities of states are projected onto the atoms at the two inequivalent Rb guest atom sites and onto the three inequivalent Sn sites for Rb_8Sn_{46}, and onto the corresponding atoms sites for $Rb_8Sn_{44}\square_2$.

In Figs. (5.6), (5.7) and (5.8) we plot the site projected density of states (pDOS) for fictitious A_8Sn_{46} and the $A_8Sn_{44}\square_2$ vacancy compounds. In each of the figures we show representative pDOS at the two inequivalent guest atom sites, Wyckoff a and d sites, and the three inequivalent framework atomic sites, c, i and k-sites as shown in Fig.(5.2). For the vacancy compounds we show the projected density of states on the equivalent atoms, which have, of course, moved relative to the original positions and relative to each other. The vacancy system has a reduced symmetry and hence many more inequivalent



(a) (b)

Figure 5.8: Projected density of states for the stoichiometric system Cs_8Sn_{46} (a) and for the vacancy system $Cs_8Sn_{44}\square_2$ (b). Densities of states are projected onto the atoms at the two inequivalent Cs guest atom sites and onto the three inequivalent Sn sites for Cs_8Sn_{46}, and onto the corresponding atoms sites for $Cs_8Sn_{44}\square_2$.

sites, but here we are interested in a representative comparison for the current discussion.

For each of the three stoichiometric systems we see a finite density of states below zero THz. This becomes more pronounced as we go from Cs_8Sn_{46} to Rb_8Sn_{46} to K_8Sn_{46}. It is not visible for Cs_8Sn_{46} on the scale of Fig. (5.8) and may be attributable to numerical errors. The Sn pDOS make marginal contributions to the pDOS in the negative frequency range and the contribution is within numerical error, which suggest that the framework may be dynamically stable without the introduction of the guest atom. For comparison we calculated the phonon structure of the fictitious Sn_{46} framework in the cubic type I-clathrate structure [86]. Our LDA calculation gives a dynamically stable cubic equilibrium structure with lattice parameter of 12.026 Å, comparable to the lattice parameters for the encaged compounds. We show the cumulated Sn projected density of states of the three vacancy compounds and the cumulated projected density of states of the Sn_{46} framework in Fig. (5.9). The phonon structure of Sn_{46} has two distinct regions where the density of states peak, the lower peak at $\approx$ 1.2 THz and another peak at about 5.1 THz. This general structure is also found in the framework phonon spectrum of the vacancy compounds. In the lower frequency region, the shape of the peak is almost retained with little increase in width and some reduction of the height of the peak. In the higher frequency region above $\approx$ 4.5 THz, the effect of the guest atoms and vacancies on the Sn phonon structure is more pronounced, with a shift of the peak frequencies and a different weight distribution. In the lower frequency region the interaction of the Sn atoms with the guest atoms and vacancies has a less pronounced effect on the framework phonon spectrum than that in the higher frequency region.

For all three compounds, the pDOS of the guest atoms in the stoichiometric compounds show two narrow peaks at the d-sites and a single narrow peak at the a-site. The d-sites are at the centre of the larger tetrakaidecahedral cages and the c-sites at the centre of the smaller dodecahedral cages. All the peaks for the guest atoms in the tetrakaidecahedral cages move to increasingly lower frequencies as we go from Cs_8Sn_{46} to Rb_8Sn_{46} to K_8Sn_{46}. The lowest peak in the pDOS for K_8Sn_{46} is near -0.4 THz while for Rb_8Sn_{46} lies at approximately -0.2 THz. On the other hand, for Cs_8Sn_{46} all the peaks in the guest atom phonon-spectrum are positive. The peak at the a-site, in the smaller dodecahedral

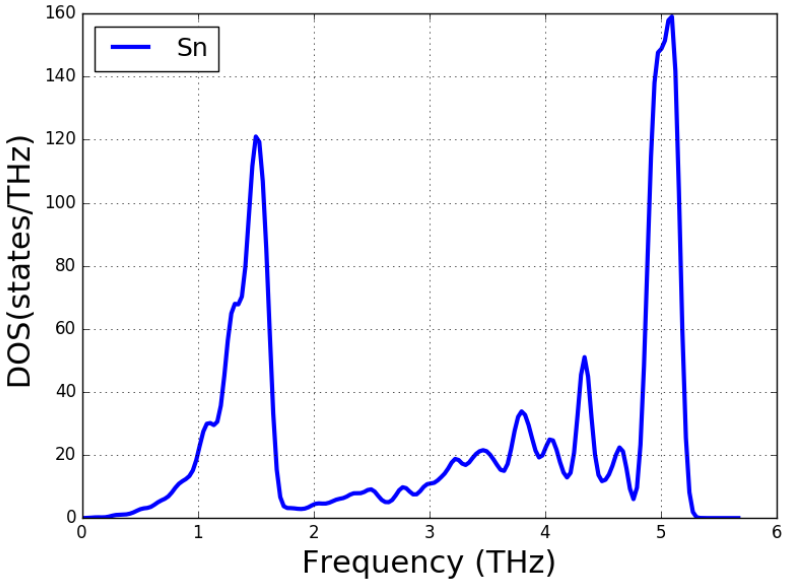


Figure 5.9: Cumulated projected density of states for the fictitious Sn_{46} framework.

cage, is at a positive frequency for all the compounds considered. The two peaks in the pDOS, Figs. (5.6), (5.7) and (5.8), of the guest atoms at the d-sites reflect the different potentials experienced by the guest atom for motion in the horizontal plane, perpendicular to the six-fold axis shown in Fig. (5.2) and in the vertical direction along the six-fold axis. The lower frequency peak is dominated by motion in the horizontal plane and the higher frequency peak by motion along the six-fold axis as can be seen from directional projected densities of states. This is confirmed in subsection 5.4.3. The ratio of the heights of the peaks are about 2 to 1, which reflects the contribution from two modes in the plane and one mode perpendicular to the plane. The a-sites are in a more spherically symmetric environment and the distinction in energy associated with motion in different directions is less pronounced.

The negative frequencies for the guest atoms suggests that for K_8Sn_{46} and Rb_8Sn_{46} the framework does not provide a sufficiently strong potential to fix the guest atoms at the d-site, the centre of dodecahedral cage. By symmetry the force at the centre of the cages is zero, but the negative frequencies indicate that this is a labile equilibrium position. We have not investigated if it is possible to move the K and Rb atoms to stable positions in the dodecahedral cage since experiment [144, 85], and our calculations, suggests that the stoichiometric compounds are stabilised by the formation of vacancies.

In Figs. (5.6), (5.7) and (5.8) (b), which show the pDOS for the vacancy compounds projected onto equivalent atoms used for the stoichiometric systems, we see no significant contributions at negative frequencies. In other words, the pDOS show that the vacancy compounds are dynamically stable, confirmed by the phonon dispersions shown in Figs. (5.3), (5.4) and (5.5). The framework pDOS span ranges, decrease with increasing atomic mass of the guest atoms, which can be attributed to an increase in the volume or the corresponding increase in the average bond length between the Sn atoms. For all three compounds the structure of the framework pDOS is similar, though the details are different. In each case the main features of the Sn_{46} framework phonon spectrum is retained with a peak in the low frequency region with peaks at about 1.5 THz and a high density of states above about 4.5 THz. The significant changes are in the guest atom pDOS. Here we note that the overlap of the host and guest atom pDOS and the reduction in peak height and more diffuse distribution of the guest atom pDOS

suggest that, in comparison with what happens in the fictitious stoichiometric system, the coupling between the guest atom and the host has increased. This is especially pertinent for $K_8Sn_{44}\square_2$.

The pDOS at the a-sites for $Cs_8Sn_{44}\square_2$ and $Rb_8Sn_{44}\square_2$ overlap with the lower framework peak while the pDOS at the d-sites are concentrated below the lower Sn peak. There is little contribution from the guest atoms to the phonon spectrum above the lower peak in the framework spectrum. In contrast, for $K_8Sn_{44}\square_2$ the lower energy mode of the d-site guest atoms spectrum overlaps with the lower peak of the Sn framework, with an indication of splitting in this mode. The second, higher energy mode at the d-site lies above the lower fequency feature of the Sn phonon spectrum. The a-site guest atom contribution is a wide peak with a clear suggestion of splitting in this mode. This suggests that the distortion of the cages, compared to the stoichiometric compounds, are more pronounced for $K_8Sn_{44}\square_2$ than for the other two vacancy compounds.

We follow Shoko *et al.* [52] and define 'rattlers' as guest atoms loosely bound to the framework. If the encaged atoms were 'rattlers' and resonant phonon scattering were important for the suppression of the lattice thermal conductivity, we would expect, in the harmonic approximation, a sharp peak in the vibrational density of states of the guest atoms [145, 146]. Resonance scattering of the acoustic phonons would require a resonator with a low frequency in the acoustic mode frequency range. For $Cs_8Sn_{44}\square_2$, Fig. (5.8), the phonon spectrum of the guest modes at the d-site remains sharp and similar to the corresponding modes in stoichiometric compound, with the peak positions almost identical. There is a minor feature in the Sn spectrum which indicates interaction between the lower guest atoms mode and the framework. The lower mode at the d-site has a peak at 0.6 THz, above the onset of the flat optical modes. The guest mode at the c-site shows a more significant change: the sharp peak for the stoichiometric compound, becomes a broad peak centred on the lower peak in the Sn spectrum. The centre of the guest mode at the a-site remains at about the same position, but the Sn peak moves upward to coincide with the peak in the guest mode. The increase in the width of a-site feature in the guest mode suggests that there is interaction between the framework and the Cs atoms at the d-site. The guest atoms at the d-sites may have some features of a 'rattler', but this is not the case for the Cs atoms at the a-sites.

For $Rb_8Sn_{44}\square_2$, Fig. (5.7), that relative change in the guest atom vibrational spectrum is more pronounced for the d-site spectra. Here the two peak feature changes to a broad feature with three peaks. Three peaks are also visible for the stoichiometric systems, suggesting that the anisotropy of the tetrakaidecahedral cage has a more pronounced influence in this case, compared to the C_8Sn_{46} and K_8Sn_{46} compounds. There is a slight increase in the width of the guest atom peak at the a-site with the peak position moving to slightly higher frequency, consistent with a decrease in volume. The phonon spectrum suggests that for this system it is also not possible to consider the guest atoms as 'rattlers'.

For $K_8Sn_{44}\square_2$, Fig. (5.6), that relative change in the guest atom vibrational spectrum is significant for all three modes. The centre of the lower frequency mode at the d-sites moves from a negative frequency to about 1.5 THz, and a width that coincides with the width of the lower frequency feature in the framework spectrum. This suggests significant interaction between the guest atoms at the d-sites and the framework. The upper peak for the guest atom at the d-site shifts upward by about 1.3 THz and broadens, also suggesting interaction with the Sn atoms. The feature for the guest atoms at the centre of the dodecahedral cages, shifts upward and broadens significantly, with clear evidence of splitting. This also indicates interaction between the guest and framework atoms. The phonon spectra for the K guest atoms shows significant interaction with the framework and the guest atoms cannot be considered 'rattlers'.

5.4.2 Vacancies

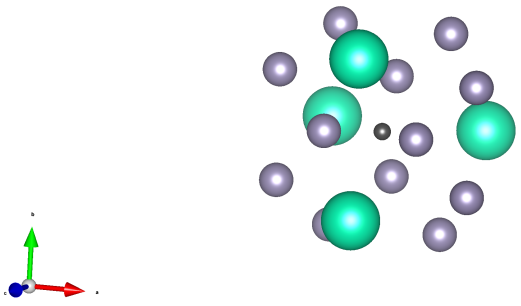


Figure 5.10: Relaxed atomic configuration around the vacancy created by removing a Sn atom from a Wyckoff c site in the lower hexagonal ring in Figure (5.2). The small dark sphere indicates the approximate position where the Sn framework atom was removed. All atoms within a radius of about 5 Å from the vacancy centre are shown.

In Fig. (5.10) we show a representative relaxed structure around the vacancy created in the lower hexagonal ring shown in Fig. (5.2). In all three compounds the configuration is similar and we show only one structure here. There are four original d-site guest atom within a radius of about 5 Å from the 'centre' of the vacancy. The vacancy destroys the local symmetry as can be seen from the different positions of the peaks in the pDOS signals of the guest atoms, Figs. (5.13) (a), (5.12) (a) and (5.11) (a). The information is summarised in Figs. (5.13) (b), (5.12) (b) and (5.11) (b). The overlap of the pDOS dispersions for the K- and Sn- sites for $K_8Sn_{44}\square_2$ below 3 THz, Fig. (5.11), suggests significant coupling between the framework and the guest atoms. In contrast, for $Cs_8Sn_{44}\square_2$ and $Rb_8Sn_{44}\square_2$, the guest atoms show peaks in their pDOS below the regions where the pDOS of the framework shows significant contributions in the low frequency range, below 2 Hz. The peak heights relative to the peaks heights in the pDOS of the framework atoms and the position of the peaks, suggest that the interactions between the guest atoms and the frameworks atoms is more pronounced for $K_8Sn_{44}\square_2$ than for the other two compounds. As noted before, the framework pDOS are similar for all three compounds, with two major regions of contribution centred between 1- 2 THz and 4 - 6 THz. This suggest that the framework atoms interact with each other in a similar manner in all three compounds. Minor variations can be attributed to small differences in bond lengths and slightly different details of the final configurations and interactions with the guest atoms. The main difference between the three compounds is the interaction between the framework and guest atoms, seen in the different structures of the guest atoms pDOS's.

In Fig. (5.14) we show a representative relaxed structure around the second vacancy, the vacancy created in the middle hexagonal ring shown in Fig. (5.2). In each case the guest atoms within a range of about $5\mathring{A}$ of the approximate centre of the vacancy, are also within the dodecahedral cages, as for the first vacancy. A study of the projected density of states, does not provide us with more information.

Using the Zintl-Kleim concept described in subsection (2.1.3) and reference [134] we determine whether we expect the vacancy compounds to be semi-conducting. We view the framework vacancies each, as

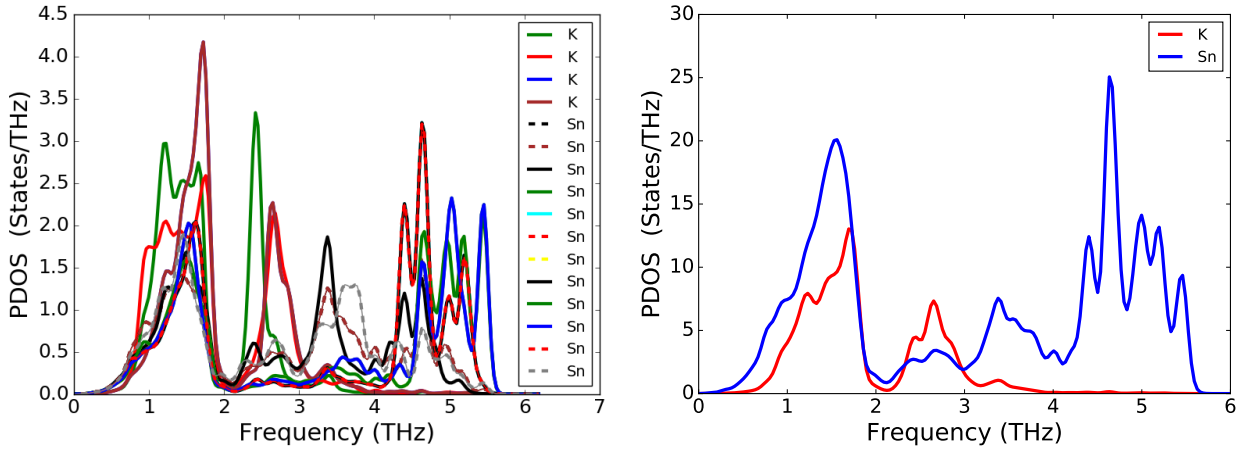


Figure 5.11: $K_8Sn_{44}\square_2$: Projected density of states for atoms near the first vacancy. (a) Individual atoms. (b) Cumulative projected density of states for K and Sn atoms near the vacancy.

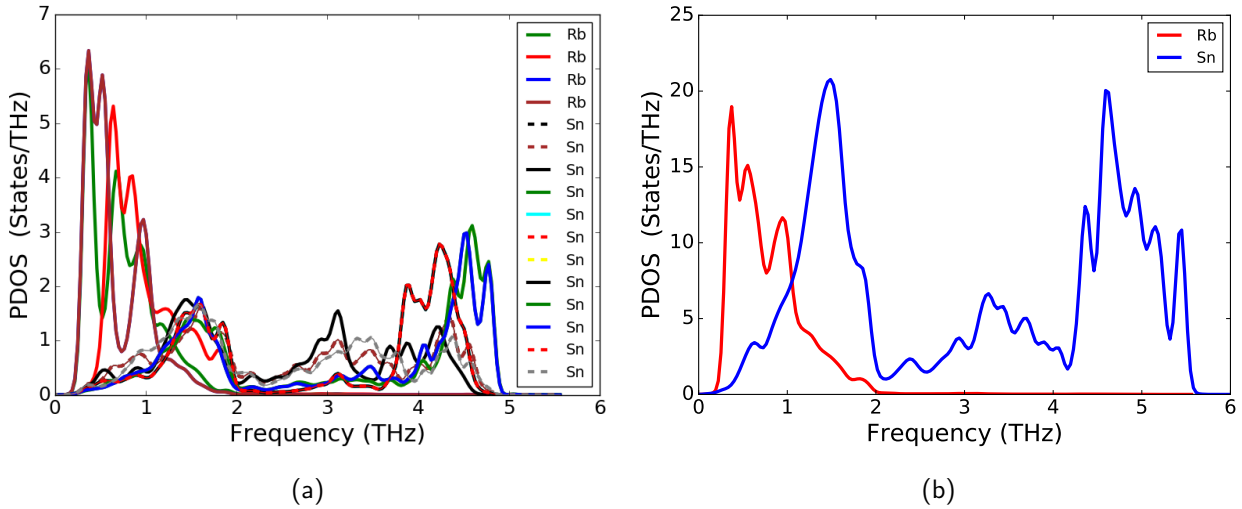


Figure 5.12: $Rb_8Sn_{44}\square_2$: Projected density of states for atoms near the first vacancy. (a) Individual atoms. (b) Cumulative projected density of states for Rb and Sn atoms near the vacancy.

being surrounded by four Sn atoms Figure (5.2) (a). Hence, the total number of 3-coordinated Sn atoms (3b-Sn) is 8, and the total number of 4-coordinated Sn atoms (4b-Sn) is 36. Applying Zintl-Kleim concept, the 3-coordinated framework atoms require 5 electrons. Therefore the total number of electrons required per framework unit is 8×5 (=40(3b-Sn)) + 36×4 (=144(4b-Sn)) = 184. On the other hand, the total number of valence electrons available per framework unit is 8×1 (8) + 44×4 (176) = 184 electrons. Meaning that the compounds are electron-balanced and therefore expected to exhibit semiconducting properties.

In summary, when we compare the fictitious stoichiometric compounds to the vacancy structures, the stability of the guest atoms in the tetrakaidecahedral cages are increased as we can see from the disappearance of negative eigenfrequencies associated with the guest atoms. This is most significant for $K_8Sn_{44}\square_2$. In all the compounds the creation of vacancies increases the interaction between the guest

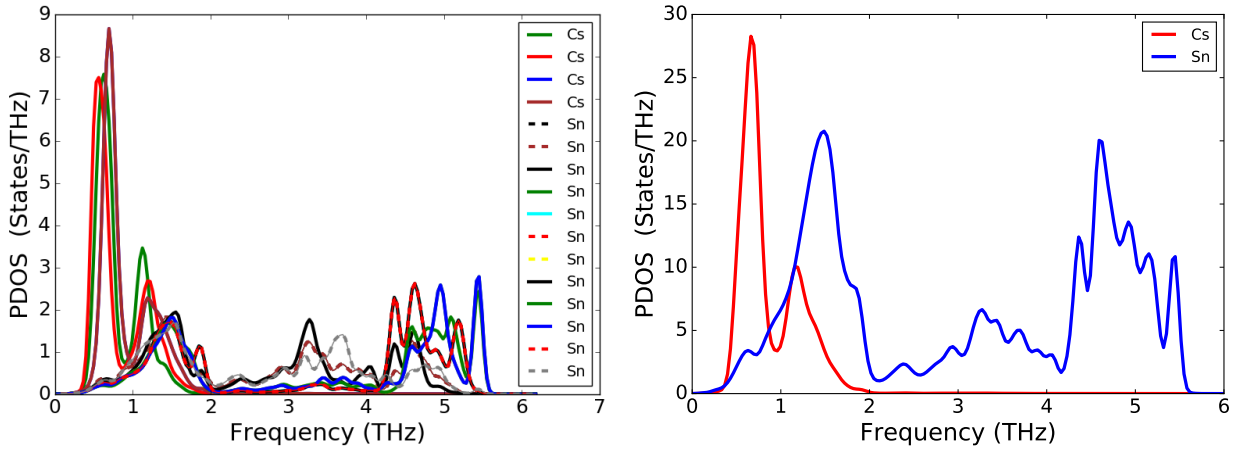


Figure 5.13: $Cs_8Sn_{44}\square_2$: Projected density of states for atoms near the first vacancy. (a) Individual atoms. (b) Cumulative projected density of states for Cs and Sn atoms near the vacancy.

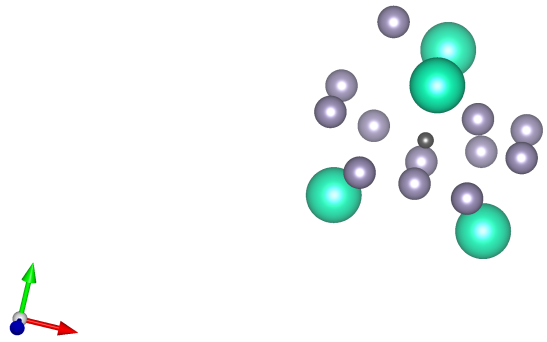


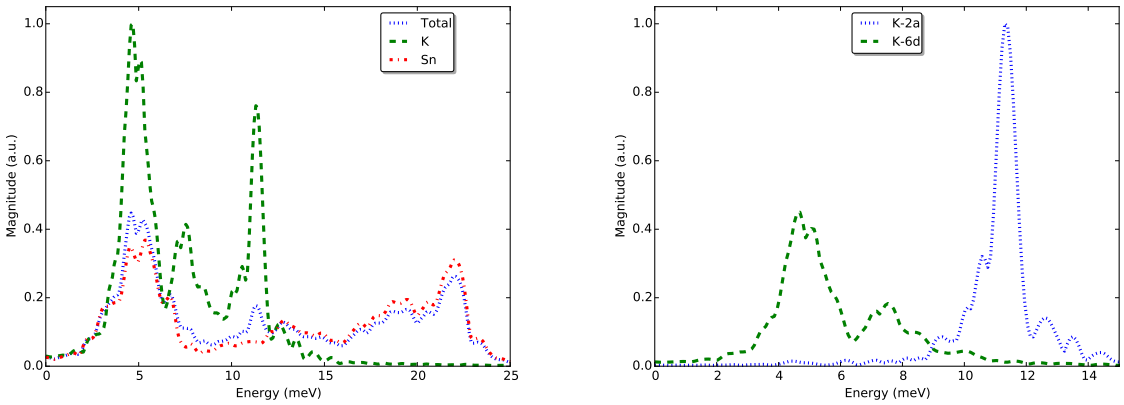
Figure 5.14: Relaxed atomic configuration around the vacancy created by removing a Sn atom from a Wyckoff c site in the middle hexagonal ring in Figure (5.2). The small dark sphere indicates the approximate position where the Sn framework atom was removed. All atoms within a radius of about 5 Åfrom the vacancy centre are shown.

atoms and the framework. Once again, this is most noticeable for $K_8Sn_{44}\square_2$. The guest atoms form an integral part of the lattice, and cannot be treated as loosely bound 'rattlers', especially for smaller guest atoms comparable to the cage size.

5.4.3 Molecular dynamics simulation

Molecular dynamics (MD) simulations were performed for the $K_8Sn_{44}\square_2$ compound at 300 K. All the simulations were run for approximately 36 ps with a time step of 1 fs. The main results from the MD calculations are the following: For the K atom, three main peaks in Fig. (5.15a) located at about 4.7

meV (1.13 THz), 7.5 meV (1.81 THz) and 11.2 meV (2.71 THz) are seen, while for the Sn atoms, two main features at about 5.0 meV (1.21 THz) and 22.0 meV (5.3 THz) are visible.

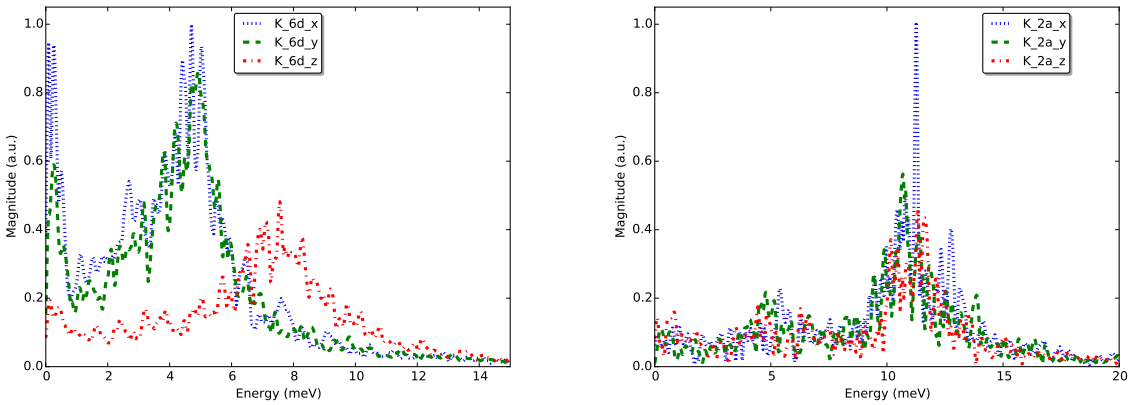


(a) Main peaks (b) Site spectra

Figure 5.15: MD phonon spectra for K_8Sn_{44}. (a) Three main peaks located at about 4.7, 7.5, and 11.2 meV showing some evidence of splitting in the lower peak. (b) Site spectra of the K atoms at a- and d-sites, showing a strong peak of 11.3 meV at the a-site and two main peaks of 4.7 and 7.5 meV at the d-site.

This is consistent with the phonon density of states shown in Figs. (5.6) and (5.11), with the peak positions and peak widths of the K atom and the Sn framework from the two studies coinciding well (Figure (5.15b)). The MD simulation shows some evidence of weak splitting in the low-energy which is found in the Sn as well as in the K spectra. This is also found in the phonon spectra, Fig. (5.11) and is suggestive of coupling between the framework and the guest atoms. On the other hand, the absence of any significant features in the Sn spectrum around 7.5 meV would suggest that the K mode at this energy does not strongly couple to the cage. However, the width of the peak indicates that the guest atom at the a-sites do couple to the framework, though not as strongly as the guest atoms at the d-sites. As there are no spectral features in the K spectrum above about 15 meV, the framework modes above this energy (i.e., at 19.0 and 22 meV) are unlikely to couple to any of the K modes. The total spectrum, except for the small peak at 11.2 meV (arising from K atoms), closely resembles that of the Sn atoms.

A plot of the site spectra Figure (5.15b), shows two main peaks at about 4.7 and 7.5 meV, obtained in the spectrum for the d-site K atoms. In contrast, the spectrum of the K atoms at the a-site on the same plot, shows a strong peak at about 11.3 meV which is higher than the highest peak from the d-site. This is consistent with the smaller size of the a cage which presents a stronger confining potential. The two peaks at the d-sites could be a reflection of anisotropic vibration in the large cage which is not symmetrical. In order to investigate this, we have calculated spectra along the principal axes of the motion from a forward Fourier Transform of the respective trajectories, shown in Fig. (5.16a). Although this is only a rough estimate of the magnitude of the spectrum, we find that the main peak for the spectrum in the direction of least displacement is distinctly located at higher energy, about 7.5 meV, consistent with our expectation. On the other hand, we find no similar splitting in the energies when the same analysis is performed for the a-site, Fig. (5.16b). Thus from the point of view of the K dynamics, the small cage is virtually isotropic. This is consistent with what we found in the phonon-projected density of states analysis in subsection (5.4.1).



(a) d-sites (b) a-sites

Figure 5.16: Directional site spectra for K_8Sn_{44}.

To further characterize the structure of the confining potentials at the a- and d- sites, we calculated the potential of mean-force (PMF) at each site. The nearest Sn atoms are about 3.8 Å from the a-sites and about 4 Å form the d sites. The main features of the PMFs are as follows: For the atoms at the d-sites, the range of the estimated PMF is -1.0 to 1.2 Å as shown in Fig. (5.17). The bottom of the well in Fig. (5.17) is broad with the overall profile of the entire potential being anisotropic and highly anharmonic.

It is important to note that in the region around 2 meV, which is relevant for the energy level splitting discussed above, the PMF in the direction of least displacement is only about 0.03 meV above the other directions. This seems to be too small to explain the 2.8 meV energy splitting obtained, suggesting that the PMF approximation may not be accurate enough to provide meaningful quantitative results. For the K atom at the Wyckoff a-site, Figure (5.16b), the range of the estimated PMF is -0.5 to 0.6 Å, hence more strongly confining compared to the d-site, Figure (5.17). A possible double-well structure is observed in the region below 2.5 meV, a feature that doesn't exist at the d-site. Whether this is a real feature of the potential at the a-site or perhaps an artefact of the simulation not being fully ergodic is difficult to establish from the present results.

The molecular dynamics results suggest that there is strong coupling at lower energies, around 5 meV, consistent with the phonon analysis in subsection (5.4.1). This suggests that the K atoms at the d sites are an integral part of the lattice.

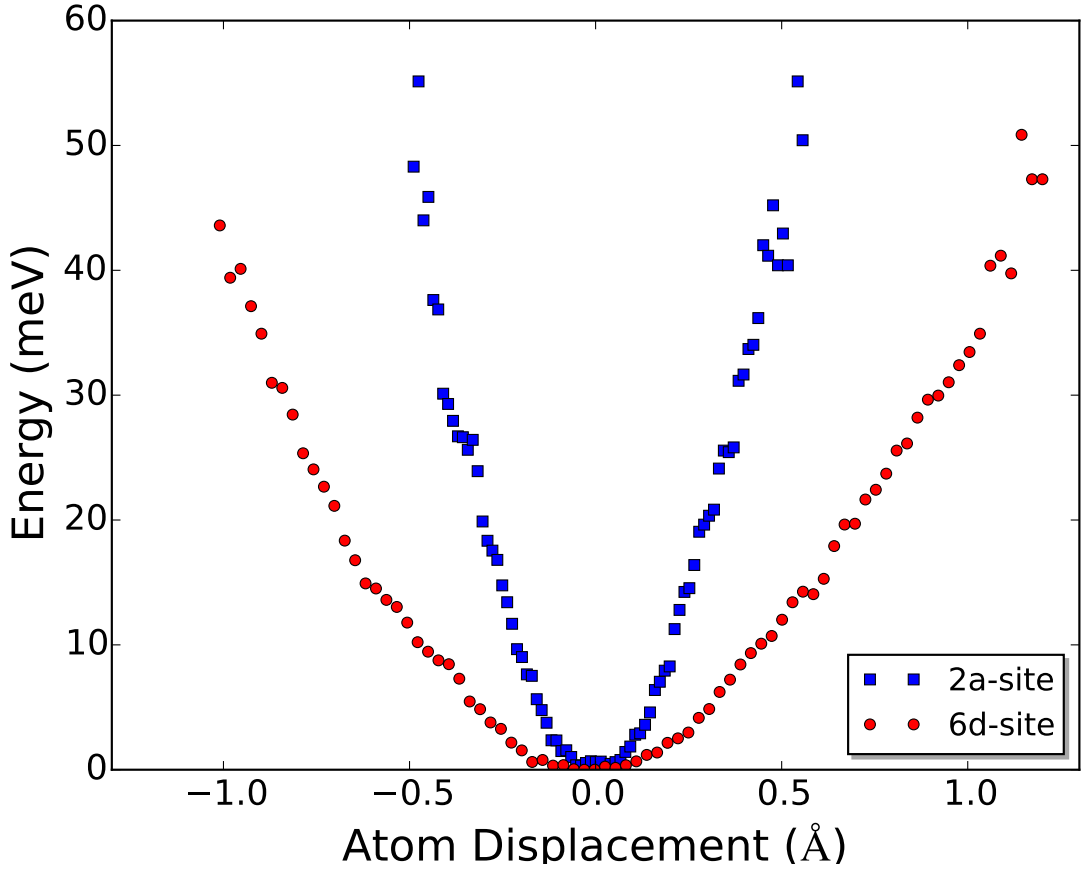


Figure 5.17: Estimated potential mean force at the a- and d-sites.

5.5 Grüneisen parameters

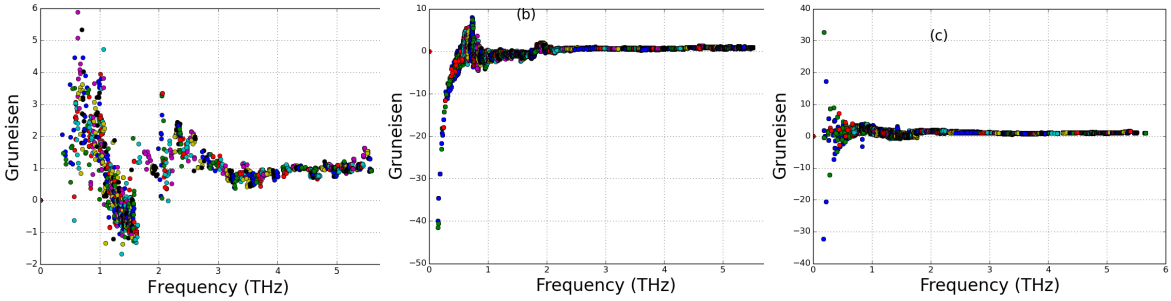
In order to resolve what may be responsible for the observed low thermal conductivity of binary type-I Sn clathrates studied, the phonon and Grüneisen dispersions were calculated using DFT phonon calculations within the quasi-harmonic approximation [147]. We know that strong anharmonicity in bonding is expected to cause low thermal conductivity in ordered crystal structures [148, 149]. The magnitude of the lattice anharmonicity can be estimated from the Grüneisen parameter γ, which portrays how the phonon frequency is altered under a small change in the geometry of the crystallographic unit cell. The Grüneisen parameter is related to the strength of phonon-phonon interactions. Assuming an isotropic change in the volume

$$\gamma(\mathbf{q},s) = -\frac{V}{\omega(\mathbf{q},s)}\left(\frac{\partial\omega(\mathbf{q},s)}{\partial V}\right) = -\left(\frac{\partial \ln\omega(\mathbf{q},s)}{\partial \ln V}\right) \tag{5.5.1}$$

The Grüneisen parameter γ is a measure of the change in pressure produced by a change in system total energy under a constant volume given by the equation:

$$\gamma \equiv V\left(\frac{\partial P}{\partial E}\right)_v \tag{5.5.2}$$

E is the internal energy $= \frac{3}{2}NkT$, P is pressure $= NkT = \frac{2}{3}E$, V is the volume, T the thermodynamic temperature, k Boltzmann constant and N is that total number of particles. Figure (5.18) shows plots of the mode Grüneisen parameters at 300 K with respect to frequency for $K_8Sn_{44}\square_2$, $Rb_8Sn_{44}\square_2$ and $Cs_8Sn_{44}\square_2$.The largest magnitude of the mode γ values are found at low frequencies, showing that the acoustic modes contribute significantly to the Grüneisen parameter. The Grüneisen parameter γ was calculated at different temperature as in equation number (5.5.2) and tabulated in Table (5.3). There is an observed increase in the γ with temperature and a decrease with the size of the rattling atom. The results show that the vibration is significant at low frequency, a consequence of the acoustic mode from the plots. Such large Grüneisen parameter reflects a strong crystal anharmonicity, corresponding to a low thermal conductivity. Zhao [148] reported anomalously high Grüneisen parameters for SnSe and suggested that the 'soft' bonding (strength of anharmonicity) in the compound is a key factor. It is known that strong anharmonicity in bonding can give rise to low lattice thermal conductivity in ordered crystal structures [149, 150, 151].



(a) (b) (c)

Figure 5.18: Plot of the Gruneisen parameter with respect to frequency for (a)K in $K_8Sn_{44}\square_2$ (b) Rb in $Rb_8Sn_{44}\square_2$ and (c) Cs in $Cs_8Sn_{44}\square_2$.

Table 5.3: Calculated Grüneisen parameter at different temperatures.

Temperature (K)	$K_8Sn_{44}\square_2$	$Rb_8Sn_{44}\square_2$	$Cs_8Sn_{44}\square_2$
300	0.902	0.963	1.012
500	0.903	0.972	1.013
700	0.904	0.974	1.013
900	0.904	0.975	1.014

5.6 Electronic Structure

5.6.1 Bandstructures and densities of states

Starting with the atomic geometry given by the optimized structures (Table (5.2)), the electronic band structure of $A_8Sn_{44}\square_2$ (A = Cs, Rb and K) calculated along the high symmetry directions of the Brillouin zone (BZ) (Figure (4.1)), is presented in Figure (5.19), (5.20) and (5.21).

The electronic structure of $K_8Sn_{44}\square_2$ displayed on (Figure (5.19)), shows a mixture of heavy and light bands near the valence band maximum (VBM) and conduction band minimum (CBM). Such combination of light and heavy bands was shown to be beneficial for achieving a high power factor and improving thermoelectric performance [152]. The presence of heavy bands, characterised by the almost flat bands (S Y Γ Z) and dispersive bands (Γ X S, U R T) respectively, is attributed to the anisotropy in the orbital interaction [153]. Heavy electron mass is present along (S Y Γ Z) as indicated by the almost flat conduction band.

The electronic band structure of Rb_8Sn_{44} is presented in Figure (5.20). The electronic band structure also is characterized with a mixture of heavy and light bands near the VBM and CBM. The presence of these heavy and light bands, characterised by the almost flat bands (X S) and dispersive bands (Γ X, S Y) respectively, is attributed to the anisotropy in the orbital interaction for this compound. Heavy electron mass is present between (X S) as indicated by the almost flat band in the conduction band as shown in Figure (5.20).

Similarly the electronic band structure of Cs_8Sn_{44} is presented in Fig. (5.21). The compound is semiconducting with a narrow LDA "quasidirect" band gap 0.15 eV with the valence band maxima (VBM) at X and conduction band minima (CBM) very close to X, comparable to the results in [86].

On going from $K_8Sn_{44}\square_2$ to $Cs_8Sn_{44}\square_2$ in Figures (5.19),(5.20) and (5.21), the dispersion in the conduction band increases, but the valence band becomes less dispersive. As may be seen in Figures (5.19),(5.20) and (5.21), we find three distinct valence band maxima which are nearly degenerate and several local conduction band minima. As already calculated, we see a gradual gap opening as the conduction band minima recedes from the Fermi level, as we move from $K_8Sn_{44}\square_2$ to $Cs_8Sn_{44}\square_2$ in Figures (5.19),(5.20) and (5.21). The electronic band structure Figure (5.21), show a mixture of heavy and light bands near the VBM and CBM. The presence of these heavy and light bands, characterised by the almost flat bands (Y Γ Z) and dispersive bands (Γ X, S Y, U R, R T), respectively, is again attributed to the anisotropy in the orbital interaction. Heavy electron mass is present along (Y Γ Z) as indicated by the almost flat band in the conduction band as shown in Figure (5.21).

A light band leads to high carrier mobility, while its combination with a heavy band leads to high thermopower.

Since the electronic states within a range of about k_BT around the Fermi level are relevant for transport

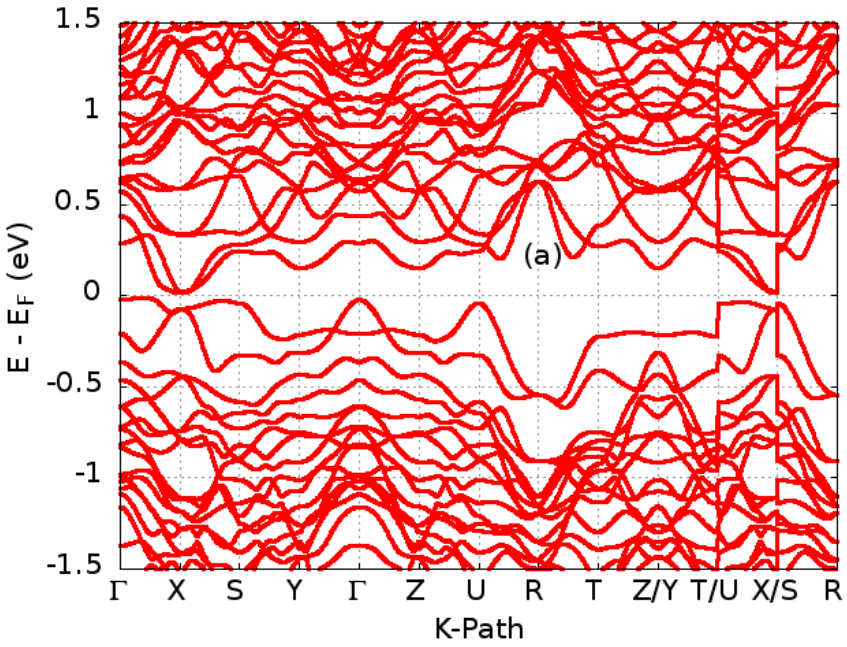


Figure 5.19: Band structure from a conventional first-principles calculations for $K_8Sn_{44}\square_2$ along different high-symmetry directions (refer to the Brillouin zone in Figure (4.1)).

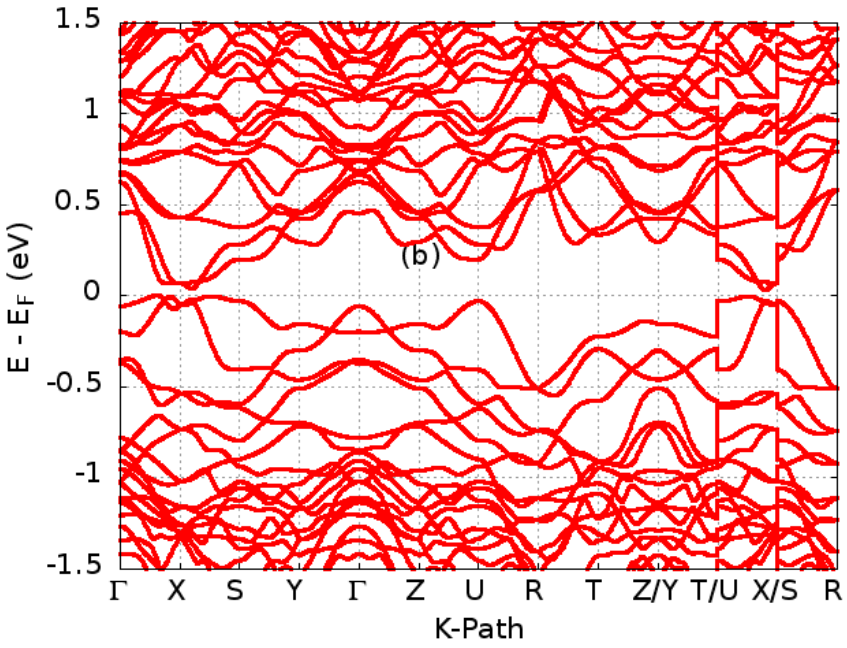


Figure 5.20: Band structure from a conventional first-principles calculations for $Rb_8Sn_{44}\square_2$ along different high-symmetry directions (refer to the Brillouin zone in Figure (4.1)).

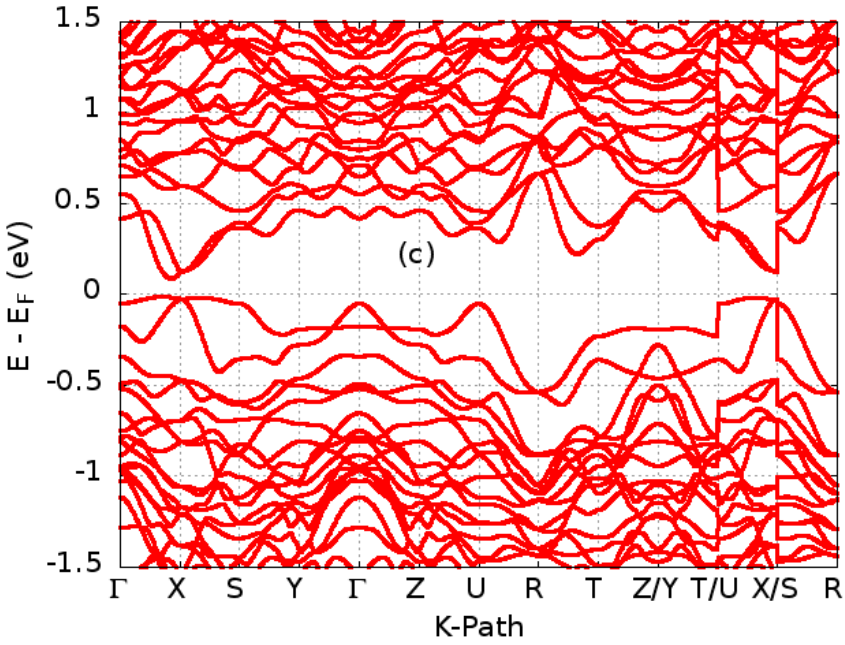


Figure 5.21: Band structure from a conventional first-principles calculations for $Cs_8Sn_{44}\square_2$ along different high-symmetry directions (refer to the Brillouin zone in Figure (4.1).

properties, we show bands around the Fermi level only. The Fermi level are important for the thermoelectric transport properties [154] hence we calculate the total (DOS) and partial density of states of these compounds (PDOS) and shown in Figures (5.22), (5.23) and (5.24). The compounds are semiconductors with a narrow indirect band gap around the Fermi level. Due to the similar crystalline structure and bonding nature, the total DOS of all the three compounds have similar shapes. As seen from the LDA calculated band structure shown in Figures (5.19), (5.20) and (5.21), the compounds are semiconductors with indirect band gaps of 0.03, 0.07 and 0.14 eV for $K_8Sn_{44}\square_2$, $Rb_8Sn_{44}\square_2$ and $Cs_8Sn_{44}\square_2$ respectively. However, the band gaps calculated with the mBJ functional [109, 110] show a small increase in each case to 0.06, 0.10, and 0.15 eV respectively. Using the "rigid-band" model we have discuss albeit qualitatively the band structure. The "rigid" band model asserts that the shape of the Fermi surface and shape of the density of states DOS of $A_8Sn_{44}\square_2$ are identical to that of the A_8Sn_{46}, assuming the shapes of A_8Sn_{46} are identical to the elemental Sn, based on previous report of [86].

Since the electronic states around the Fermi level have an important effect on the thermoelectric TE transport properties [154] of $A_8Sn_{44}\square_2$ (A = Cs, Rb and K), we calculated their electronic total (DOS) and partial density of states of these compounds (PDOS) and shown in Figures (5.22), (5.23) and (5.24). Due to the similar crystalline structure and bonding nature, the total DOS of all the three compounds has similar shape. We observe straight away that the valence and conduction band are equally dence near the band edges for the three compound, which is indicative of a near metal.

The CB from the Fermi level to 8 eV in the three compounds, is composed of p and d orbital of the guest atoms only, meaning the electrical conductivity and Seebeck coefficient are primarily determined by the guest atoms p and d orbital electrons. A large Seebeck coefficient is usually associated with a large width of the DOS [155], hence, from Figures (5.22), (5.23) and (5.24), $Cs_8Sn_{44}\square_2$ is expected to have the highest Seebeck coefficient. The width of the CB becomes narrower as we move from

$Cs_8Sn_{44}\square_2$ to $K_8Sn_{44}\square_2$. We notice an almost equal contribution by the Sn_{spd} orbital in both the CB and the VB between energy range -4 eV and +4 eV. This implies that the electron states around Fermi level is balanced and can be said to be electronically neutral. This result is in agreement with Blake [156], who suggested that the VB of type-I Sn clathrates are exclusively localized in the framework.

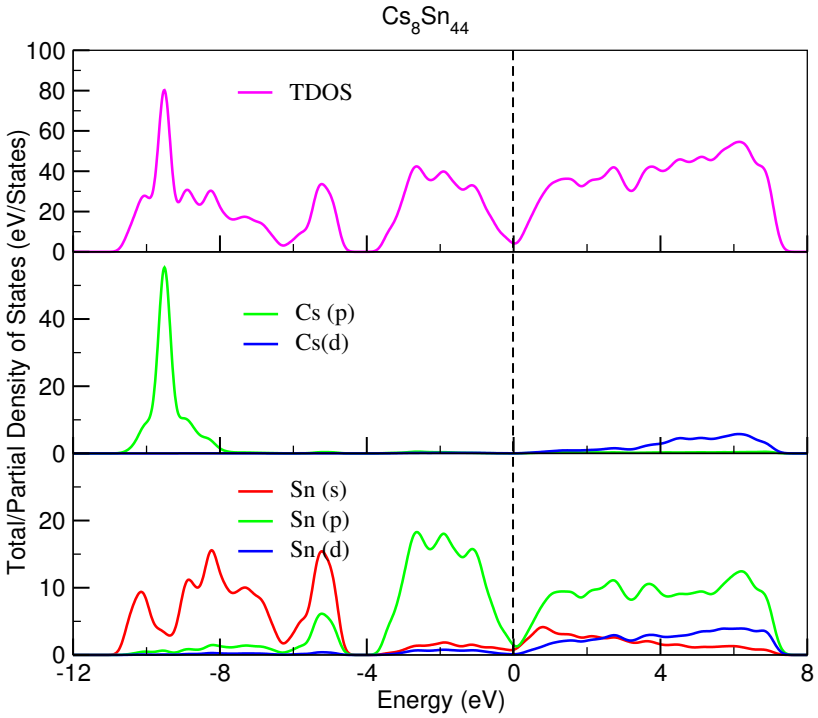


Figure 5.22: The total (TDOS) and projected density of states show the contribution of guest atoms Cs in $Cs_8Sn_{44}\square_2$. The origin of energy is the Fermi energy which is shown by a *thin dot line i.e* top of VB is set to zero.

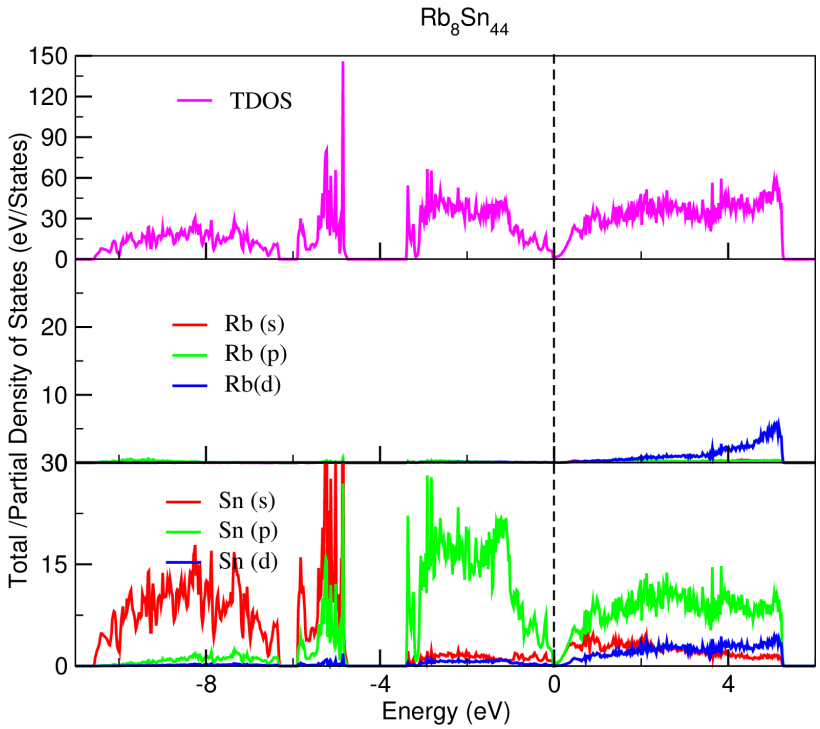


Figure 5.23: The total (TDOS) and projected density of state show the contribution of guest atoms Rb in $Rb_8Sn_{44}\square_2$. The origin of energy is the Fermi energy which is shown by a *thin dot line i.e* top of VB is set to zero.

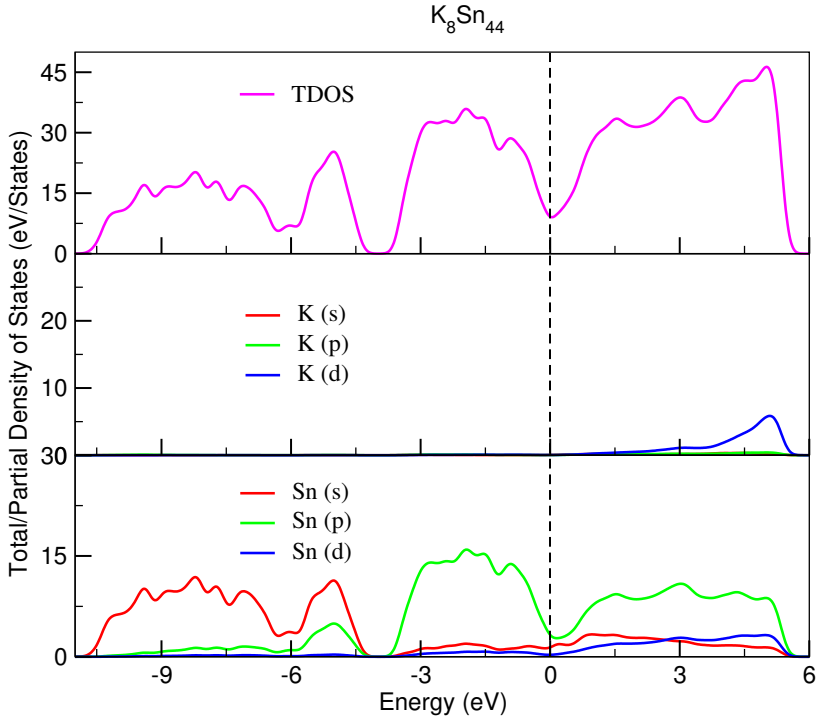
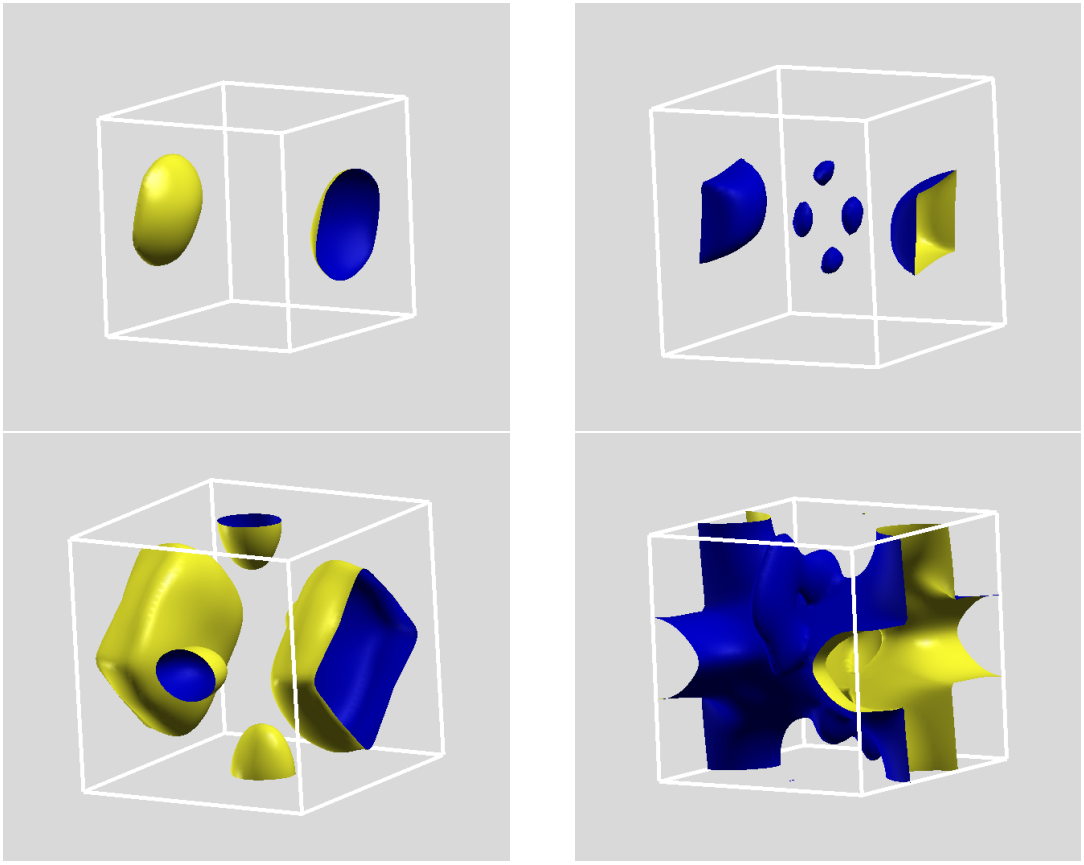


Figure 5.24: The total (TDOS) and projected density of states show the contribution of guest atoms K in $K_8Sn_{44}\square_2$. The origin of energy is the Fermi energy which is shown by a *thin dot line i.e* top of VB is set to zero.

5.6.2 Fermi surfaces

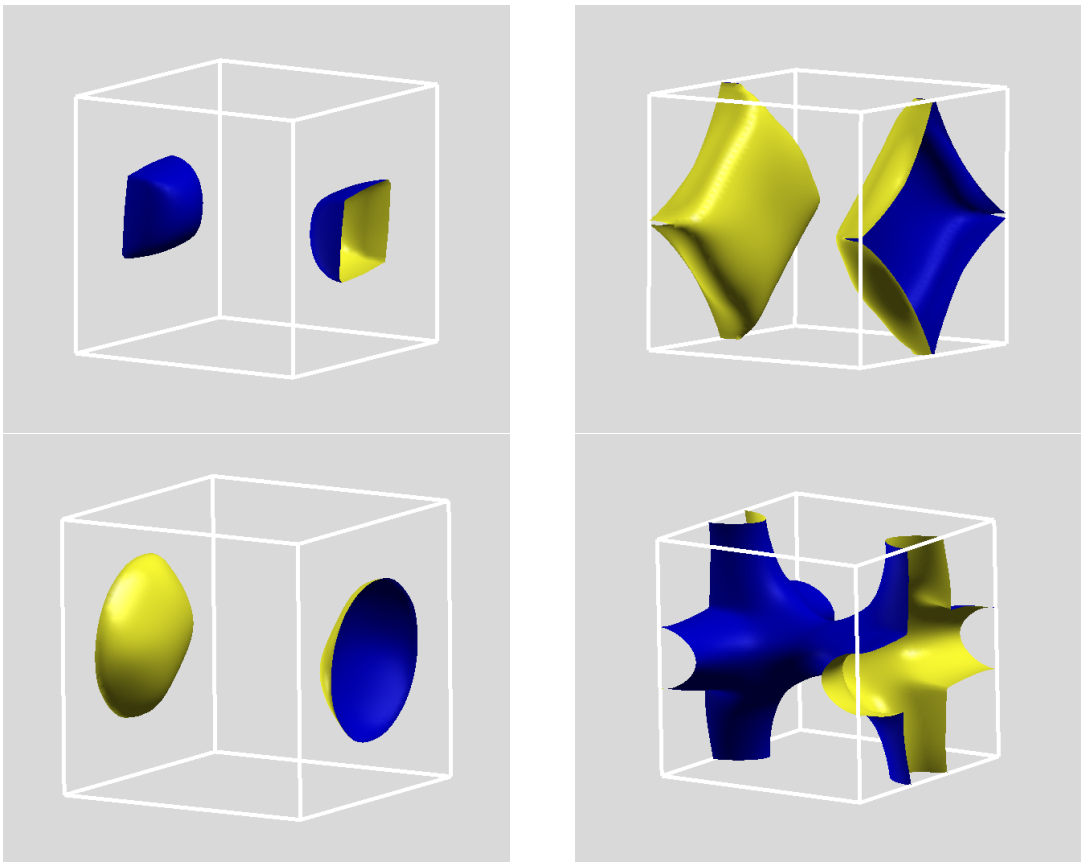
Further insight into the electronic structure is gained by plotting the Fermi surface of these compounds, as shown in Figures (5.25), (5.26) and (5.27). We note that there has not been any report, to the best of our knowledge on the Fermi surface of these these compounds.



(a) Conduction band. (b) Valence band.

Figure 5.25: Fermi surface plot for $K_8Sn_{44}\square_2$ at an isosurface value of 0.1 eV and 0.2 eV above (below) conduction (valence) band edge.

Figures (5.25a), (5.26a) and (5.27a) shows electron Fermi surface plotted for $K_8Sn_{44}\square_2$, $Rb_8Sn_{44}\square_2$ and $Cs_8Sn_{44}\square_2$. The maximum degeneracy is 3 for these compounds. This is not a particularly large degeneracy; typically degeneracies leading to a high DOS effective mass, should be at least 6 to significantly enhance the thermopower. The structure of the Fermi surface gives us a clearer visual impression of the nature of the anisotropic transport properties calculated later in this work. Looking at the Fermi surfaces, we can tell that the effective mass in the Γ X (Γ Z) direction is lower than in the Γ Y which agrees with the calculated effective mass tabulated in Table (5.4). There are important implications of this to thermoelectric material performance, as reported in section (5.11). The hole Fermi surface on the other hand is a more complex Fermi surface Figures (5.25b), (5.26b) (5.27b), which would usually result in a higher thermopower. We discuss how the n- and p-type thermopowers compare in Section

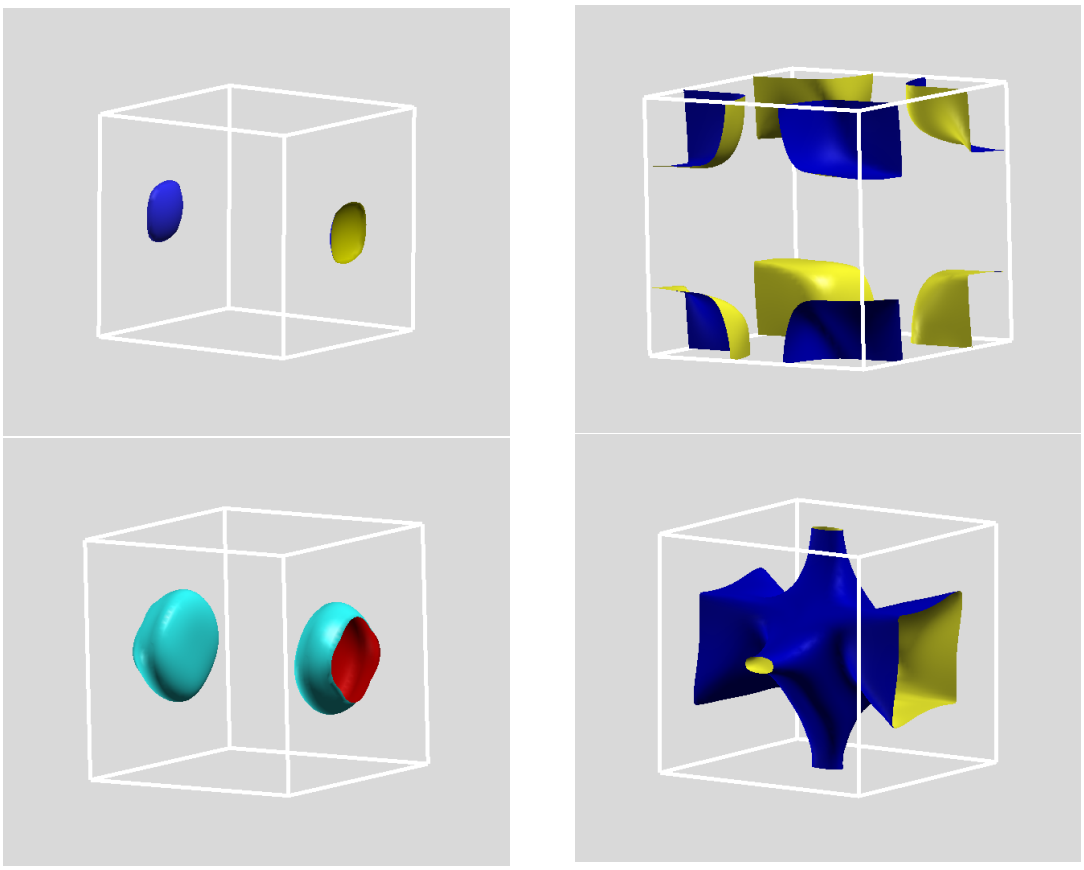


(a) Conduction band.

(b) Valence band.

Figure 5.26: Fermi surface plot for $Rb_8Sn_{44}\square_2$ at an isosurface value of 0.20 eV and 0.28 eV above (below) conduction (valence) band edge.

(5.11).



(a) Conduction band.

(b) Valence band.

Figure 5.27: Fermi surface plot for $Rb_8Sn_{44}\square_2$ at an isosurface value of 0.17 eV and 0.23 eV above (below) conduction (valence) band edge.

5.7 Anisotropic Behaviour and Effective Carrier Masses

It is well known from experiment that the transport properties of the clathrate structures show anisotropic features, and that the electrical and thermal conductivities are larger along the basal plane than along the trigonal axis [157]. In this study we corroborated the report by [158] and [159] that, type-I clathrates reveal anisotropic behaviour. We observe that our compounds have low symmetry with respect to the cubic structure symmetry we started with, and therefore would show anisotropy. We proceed therefore to calculate the effective carrier masses.

5.7.1 Effective carrier masses

Calculations of the electron effective masses (m*) were done by fitting the band structure around the conduction band minimum (CBM), and the valence band maximum (VBM) and then used the equation,

$$m_s^* = \left(\hbar^2 \frac{d^2E}{dk_s^2}\right)^{-1} \tag{5.7.1}$$

where s is a generic Cartesian direction. In its lowest approximation, using effective mass theory, the dispersion relation near the CBM can be written as [125, 126]

$$E_c(\vec{k}) = E_c + \frac{\hbar^2}{2}\left[\frac{k_x^2}{m_x^e} + \frac{k_y^2}{m_y^e} + \frac{k_z^2}{m_z^e}\right] \tag{5.7.2}$$

where E_c is the energy at the CBM, $E_c(\vec{k})$ is the approximate conduction energy at $\vec{k}$ and m_x^e, m_y^e and m_z^e are the principal electron effective masses in the x-, y- and z-directions. A similar expression applies to the dispersion near the VBM with the electron effective masses m^e replaced by the hole effective masses m^h.

In a semiconductor, the two types of charge carrier i.e, the electron and the hole can contribute to a current. The average number of electrons in the conduction band and the number of holes in the valence band, gives an indication of the density of these charge carriers and a measure of the size of current. The Seebeck coefficient is dependent on the density of states effective mass. When the density of electrons is greater than the density of holes, the semiconductor is n-type and when the density of holes is greater than the density of electrons it is p-type. We know that the distribution (with respect to energy) of electrons (holes) is given by the the density of allowed quantum states times the probability that a state is occupied by an electron (hole):

$$n(E) = g_c(E) f_F(E), p(E) = g_v(E)[1 - f_F(E)] \tag{5.7.3}$$

where $g_{c,v}$(E) is the density of quantum states in the conduction (valence) band, and f_F(E) is the Fermi-Dirac probability function. Hence, the total electron concentration per unit volume in the conduction (valence) band, can be found by integrating over the entire conduction (valence) band energy. In order to find thermal equilibrium, we need to determine the position of the Fermi energy E_F, with respect to the bottom of the conduction band energy E_c and the top of the valence band energy E_v. The Seebeck coefficient depends on the density of states effective mass m_d, which is approximately given by the expression

$$m_d = N_v^{\frac{2}{3}}(m_x m_y m_z)^{\frac{1}{3}} \tag{5.7.4}$$

where N_v is the effective density of states function (that is number of equivalent band minima). On the other hand the electrical conductivity can be expresed as a quantity which is inversely proportional to the average effective mass m^*_{cond} [125], given by:

$$m_{cond} = 3(\frac{1}{m_x^*} + \frac{1}{m_y^*} + \frac{1}{m_z^*})^{-1} \tag{5.7.5}$$

The diagonal elements of the effective mass tensor m_e^* for the electrons near the conduction band bottom are calculated using the relation in equation number (5.7.1), the effective mass of the electron is evaluated by fitting the electronic band structure near the bottom to a parabolic function [125, 126], (5.7.2).

Table 5.4: Calculated m_e^* and m_h^* effective masses in electron rest-mass units in the x-, y- and z-directions for $A_8Sn_{44}\square_2$.

	K_8Sn_{44}			Rb_8Sn_{44}			Cs_8Sn_{44}		
	x	y	z	x	y	z	x	y	z
m_e^*	0.223	2.221	0.774	0.606	1.011	0.618	3.25	0.44	0.44
m_h^*	-0.741	-0.737	-0.205	-0.701	-0.507	-0.250	-0.86	-0.46	-0.46
m_d^*	0.48(elec)	0.39(holes)		0.69(elec)	0.42(holes)		0.64(elec)	0.56(holes)	
m_{cond}^*	0.734			0.723			0.857		

Table (5.4), shows the effective mass values for $A_8Sn_{44}\square_2$ (A =K, Rb and Cs). The effective mass follows the trend observed in the dispersion of band structure. The negative value for the hole effective masses indicate that the band curves downwards as can be observed in the valence band along $\Gamma - X$ (y-direction), which leads to a large effective mass in y-direction for the $A_8Sn_{44}\square_2$ (A =K, Rb and Cs). The conductivity is inversely proportional to the effective mass [125] and our results on Table (5.4) show differences in the x-, y- and z-directions consistent with the anisotropy in the effective masses.

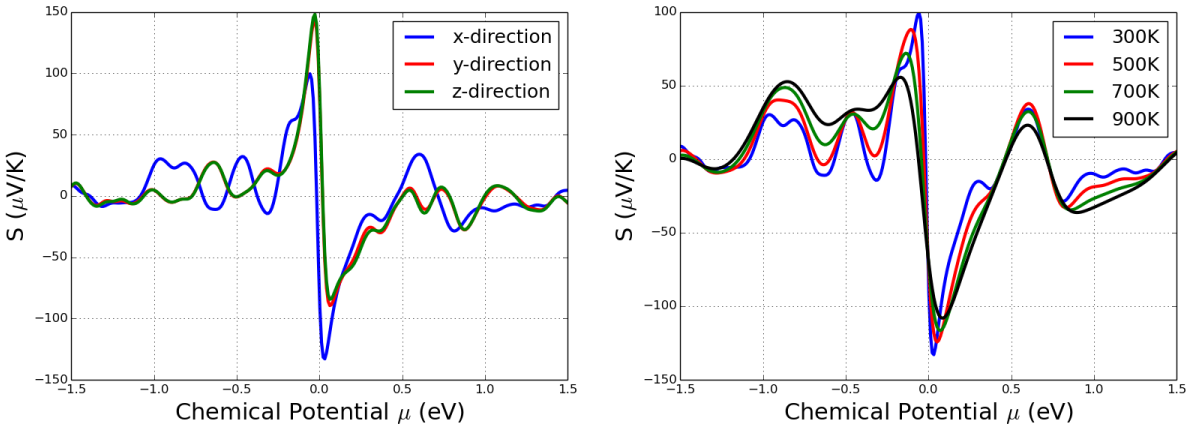
5.8 Seebeck Coefficient

The Seebeck coefficient is the ratio of the potential difference ΔV that arises due to a temperature difference ΔT. The magnitude and sign of the Seebeck coefficient are related to the electron density of states and dispersion of the electron eigenstates near the Fermi level as we can see in Eq. (3.5.2).

Clathrates exhibit disparate types of majority carriers, and therefore, Seebeck coefficients can be positive (majority carriers are holes) or negative (majority carriers are electrons). The different values of Seebeck coefficients in clathrates come from influences that may include one or a combination of, band gap, concentration of charge carriers, degree of the framework disorder, and many others. For ideal semiconductors, the higher the electrical conductivity, the lower the Seebeck coefficient is, which stems from the opposite trend of their dependence upon the concentration of charge carriers [160, 99].

The position of the chemical potential μ is important with regards to a materials' transport properties. Where μ is located within the bandstructure determines which charge carriers in the valence or conduction band take part in the electronic transport and can influence both the conductivity and Seebeck coefficient. Doping or substitution is used to manipulate the chemical potential and the corresonding charge carriers that contribute to the conductivity. The chemical potential is temperature dependent and differs from system to system depending on the distribution of the density of states of the charge carriers. The behaviour of the chemical potential with varying temperature and doping plays a crucial role in determining the thermoelectric performance of materials. In the rigid band approximation, assumed in this study, the band structure is assumed to be independent of the amount of doping and only the position of the chemical potential is affected by doping. By definition $\mu = 0$ corresponds to the top of the valence band in semiconductor [161] at 0 K for no doping. The chemical potential increases with temperature if the doping is kept fixed [162]. The simple constant relaxation time approximation is often adopted in first principles calculation, which may turn out to be a good approximation especially for bulk materials [128, 130, 129]. We have used a constant relaxation time of 10 fs in our work based on experimental result from a similar group-14 n-type polycrystalline samples of Ge clathrates of cubic structure (space group Pm-3n) [16] .

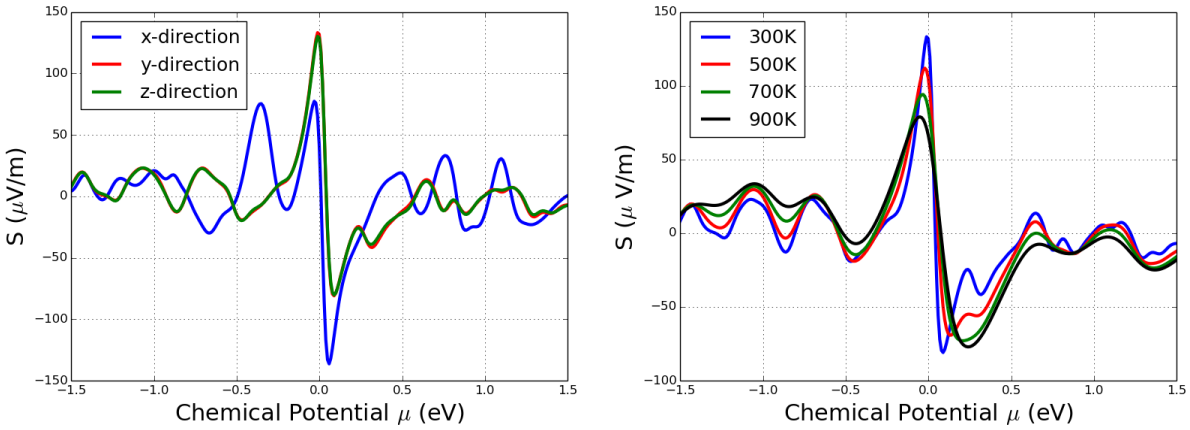
Figures (5.28a), (5.29a) and (5.30a) shows the Seebeck coefficient plotted against the chemical potential at 300 K for $A_8Sn_{44}\square_2$ (A = K, Rb and Cs). From Figure (5.28a), we see that at $\mu = 0$ eV [162] the value of the Seebeck coefficient for $K_8Sn_{44}\square_2$ is -106.8 μV/K in the x-direction. This result indicates that the majority carriers in the x-direction are electrons. A maximum value of S (-133.0 μV/K) at 300 K was obtained at a chemical potential slightly above zero. In the y-direction however, a relatively higher value of +148.2 μ V/K at $\mu = 0$ eV is found and the major carriers are holes. This reflects the anisotropy in the electronic structure of the compound and the narrow bandgap.



(a) At 300 K showing uniaxial anisotropy (b) At different temperatures

Figure 5.28: Seebeck coefficient for $K_8Sn_{44}\square_2$.

Similarly, in Figure (5.29a) for $Rb_8Sn_{44}\square_2$, at $\mu = 0$ eV, the value of the Seebeck coefficient is 45.43 μV/K in the x-y plane, and a maximum value of 133.28 μV/K in the y-direction, indicating that at 300 K and $\mu = 0$ the majority carriers are holes. We however obtained a maximum value of the Seebeck coefficient for electron majority carriers at 300 K in the x-direction to be -136.36 μV/K at a chemical potential slightly above zero. This result indicates that the un-doped compound is a hole majority carrier semiconductor with a maximum value of the Seebeck 133 μV/K at 300 K. We obtained similar



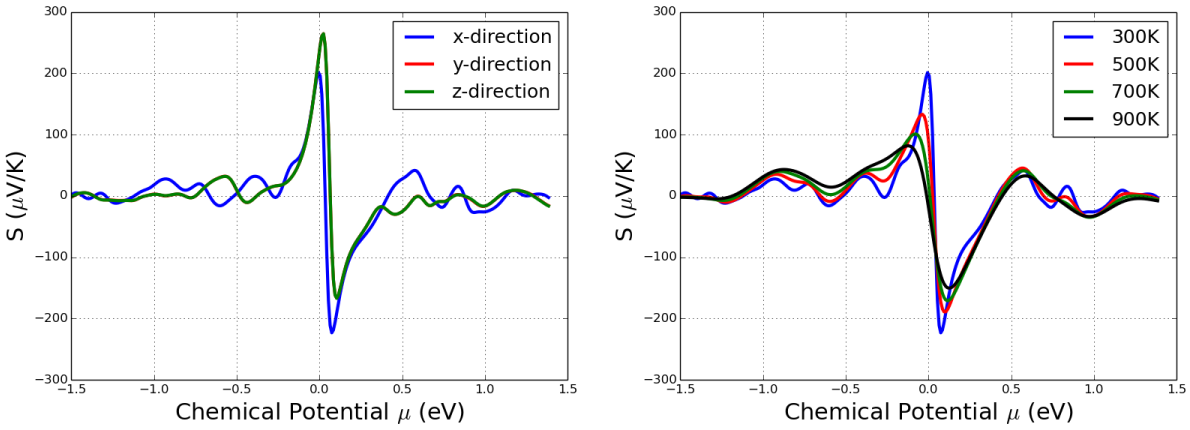
(a) At 300 K showing uniaxial anisotropy (b) At different temperatures

Figure 5.29: Seebeck coefficient for $Rb_8Sn_{44}\square_2$.

behaviour for $Cs_8Sn_{44}\square_2$. Figure (5.30a) shows the Seebeck coefficient plotted against the chemical

potential at 300 K. From the Seebeck plot, we note that at $\mu = 0$ eV, the value of the Seebeck coefficient is 199.53 μV/K in the in x-z plane, and a maximum value of 202.56 μV/K for μ slightly above 0 eV, indicating that $Cs_8Sn_{44}\square_2$ behaves like a hole majority carrier semiconductor in the x-y plane. We however obtained a maximum value of the Seebeck coefficient of 265.83 μV/K in the z-direction.

Figures (5.28b), (5.29b) and (5.30b) shows plots of Seebeck coefficient at different temperatures as a function of chemical potential for the three compounds. As may be seen from Figures (5.28b), (5.29b) and (5.30b), there is a gradual increase in the Seebeck as we move from the guest atom K to Cs. The Seebeck coefficient is comparable to the experimental results of Cohn *et al.* [21] for Cs_8Sn_{44} 304 μV/K . Table (5.5) shows extracted data of the Seebeck coefficient at calculated temperatures for electron majority carrier of $A_8Sn_{44}\square_2$, whilst Table (5.6) is data for p-type doping. Since the compounds show uni-axial anisotropy, only the results for the x-y plane and x-z plane are published. Achieving $ZT \approx 1$ requires a Seebeck coefficient S $\approx$ 200 μV/K. By combining the Wiedemann-Franz-Lorenz law equation (1.0.5) for a material of fixed doping, if we assume the thermal conductivity to be unity, the average Seebeck coefficient that would yield $ZT \approx 1$ should be about 200 μV/K. As shown from our results, $Cs_8Sn_{44}\square_2$ satisfies this criteria for an intrinsic semiconductor. Motivated by these, we proceed to study other thermoelectric properties of these compounds.



(a) At 300 K showing uniaxial anisotropy

(b) At different temperatures

Figure 5.30: Seebeck coefficient for $Cs_8Sn_{44}\square_2$.

Table 5.5: Extracted Seebeck Coefficient (S) for chemical potential at the top of the valence band of 5.62, 5.08 and 5.33 eV for $Cs_8Sn_{44}\square_2$, $Rb_8Sn_{44}\square_2$ and $K_8Sn_{44}\square_2$ respectively at calculated temperatures in the x- and y-directions.

System	Temperature	x-direction	y-direction
$K_8Sn_{44}\square_2$	300	-133	-89
	500	-124	-94
	700	-117	-96
	900	-108	-92
$Rb_8Sn_{44}\square_2$	300	-136	-81
	500	-126	-69
	700	-120	-73
	900	-111	-77
$Cs_8Sn_{44}\square_2$	300	-223	-167
	500	-189	-130
	700	-171	-112
	900	-151	-100

Table 5.6: Extracted Seebeck Coefficient (S) for a chemical potential at the bottom of the conduction band of 5.62, 5.08 and 5.33 eV for $Cs_8Sn_{44}\square_2$, $Rb_8Sn_{44}\square_2$ and $K_8Sn_{44}\square_2$ respectively at calculated temperatures in the x- and y-directions.

System	Temperature	x-direction	y-direction
$K_8Sn_{44}\square_2$	300	100	148
	500	82	118
	700	72	105
	900	56	93
$Rb_8Sn_{44}\square_2$	300	77	133
	500	84	112
	700	82	94
	900	78	79
$Cs_8Sn_{44}\square_2$	300	210	225
	500	133	184
	700	101	153
	900	82	129

5.9 Lattice Thermal Conductivity

In the Linearised Boltzmann Transport Equation (LBTE) approach under the single-mode relaxation time (SMRT) method adopted in this study [4], the lattice thermal heat conductivity, κ_l, can be expressed as

$$\kappa_l = \frac{1}{V_0} \sum_{\lambda} C_\lambda \mathbf{v}_\lambda \otimes \mathbf{v}_\lambda \tau_\lambda, \tag{5.9.1}$$

where V_0 is the volume of the unit cell, $\mathbf{v}_\lambda$ and τ_λ are the group velocity and the relaxation time of the

phonon mode λ,respectively. C_λ is the modal heat capacity defined as

$$C_\lambda = k_B \left(\frac{\hbar\omega_\lambda}{k_B T}\right) \frac{\exp\left(\frac{\hbar\omega_\lambda}{k_B T}\right)}{\left[\exp\left(\frac{\hbar\omega_\lambda}{k_B T}\right) - 1\right]^2} \tag{5.9.2}$$

Here λ is a compound mode index $(\mathbf{q}, j)$, with $\mathbf{q}$ a wave vector in the first Brillouin zone and j is a phonon band index.

In Fig. (5.31) we show the average cumulative heat capacity, that is Eq. (5.9.1) summed over all modes with frequencies less or equal to a given frequency, for $A_8Sn_{44}\square_2$, (A = Cs, Rb, K) and the framework Sn_{46} at 300 K. We scaled the entry for Sn_{46} by a factor of $\frac{1}{20}$ to get a reasonable scale for comparison. The total thermal conductivity of the fictitious framework structure is more than an order of magnitude larger than the total thermal conductivity of the vacancy systems. For the vacancy systems the thermal conductivity decreases with decreasing volume of the guest atom. Contributions to the thermal conductivity come from all frequencies, but in each case there is a major contribution from modes with frequencies below 1 THz.

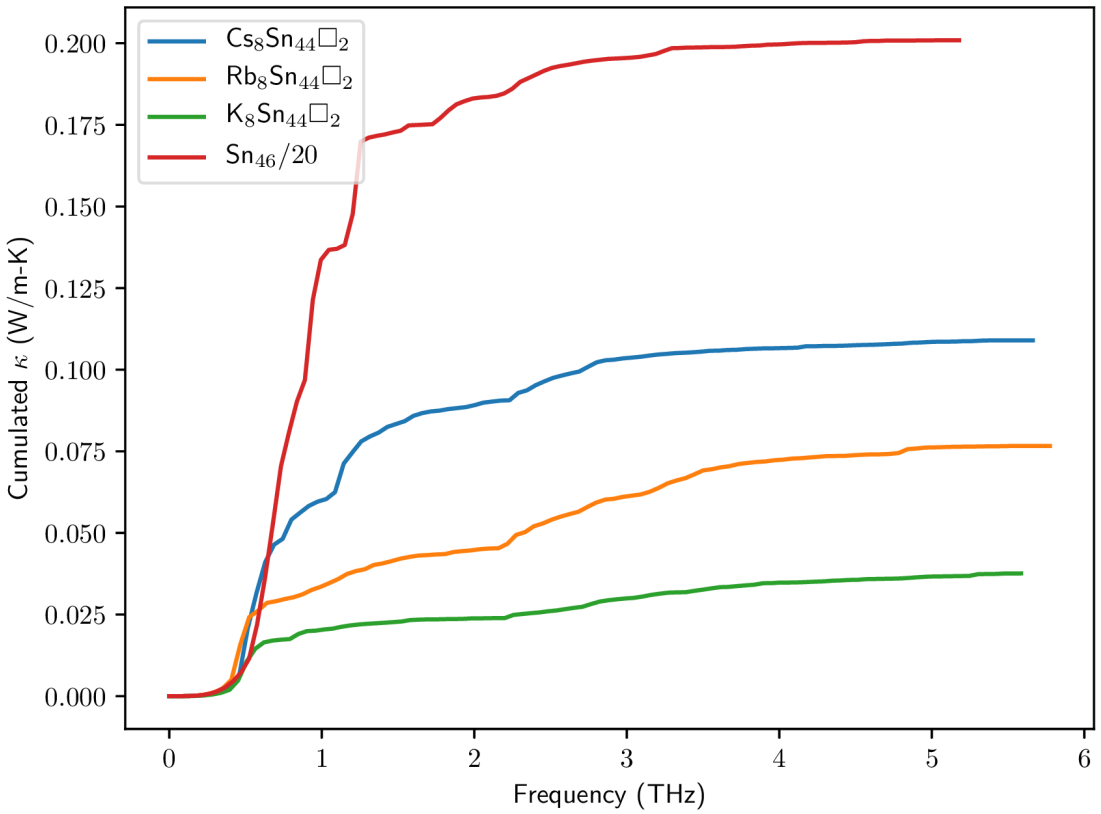


Figure 5.31: Average cumulative lattice thermal conductivity for $A_8Sn_{44}\square_2$, (A = Cs, Rb, K) and the fictitious framework Sn_{46} structure as a function of frequency at 300 K.

The modal heat capacity, Eq. (5.9.2), is temperature and frequency dependent, but is only indirectly dependent on the phonon structure through ω_λ. For the compounds under investigation, the frequency

distributions are similar and this term will not account for the difference in the values of κ_l as determined by Eq. (5.9.1). The two terms that are expected to show a difference between the framework and vacancy compounds are the group velocities $\mathbf{v}_\lambda$ and the relaxation times τ_λ

The group velocity is given by

$$v_\lambda(\alpha) = \frac{\partial \omega_\lambda}{\partial q_\alpha}, \tag{5.9.3}$$

where α is a Cartesian coordinate. The group velocities depend on the dispersion of the eigenfrequencies ω_λ and unless these are significantly different, there may not be significant changes from compound to compound. We have noticed from the projected densities of states that the frequency range for the framework remains very similar for all the vacancy compounds and the framework. This suggests that the group velocity distribution may not be significantly different for the compounds we are interested in. In Fig. (5.32), apart from a few high valued group velocities for the framework, the distribution of the group velocities are similar for all four systems. There is some indication that the group velocities in the low frequency region, below about 1.8 THz, is lower on average for the vacancy compounds in comparison to the fictitious framework system. Note that in the region 1.2 to 1.8 THz, and above 4 THz, the group velocities are small, as expected for flat bands.

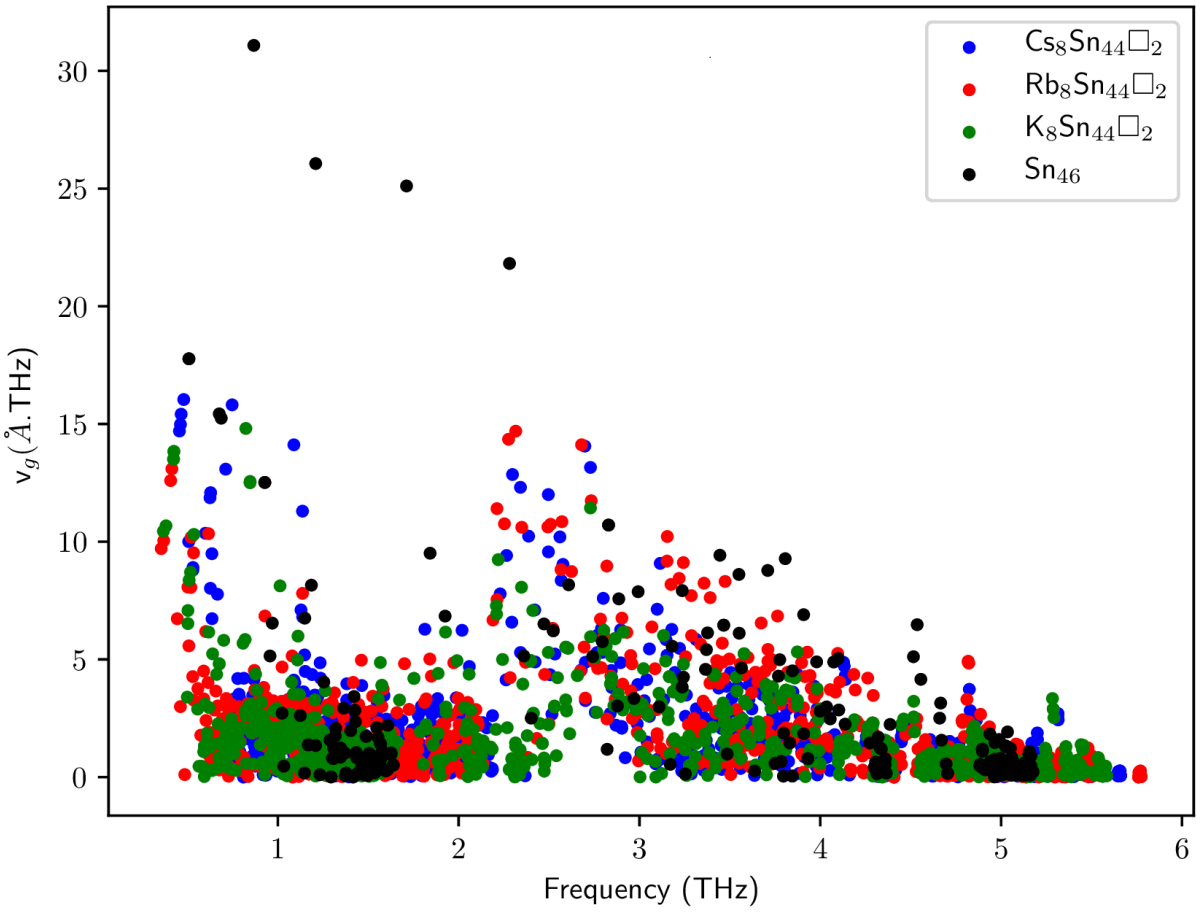


Figure 5.32: The magnitude of the group velocities, v_g, for $A_8Sn_{44}\square_2$, (A = Cs, Rb, K) and the framework Sn_{46} as a function of frequency.

The relaxation times, in the LBTE, SMRT approximation used in this study [4], depend on phonon

scattering only. In Fig. (5.33), we show representative relaxation times for $A_8Sn_{44}\square_2$, (A = Cs, Rb, K) and the framework. We immediately see that it is the difference in relaxation time that is responsible for the difference in thermal conductivities. The relaxation times for the Sn_{46} framework system is more than an order of magnitude larger than the corresponding relaxation times for the vacancy systems at each frequency. The relaxation times decrease, at each frequency, on average from $Cs_8Sn_{44}\square_2$ to $Rb_8Sn_{44}\square_2$ to $K_8Sn_{44}\square_2$. It seems that the distribution of the magnitudes of the group velocities on their own, do not account for the difference in the behaviour of the thermal conductivities of the vacancy systems compared to the framework. This is consistent with the observation that the lattice thermal heat conductivities decrease in the same order and suggests that the phonon scattering increases in the same order and is consistent with the deduction in Section (5.4) that the interaction between the framework and vacancy-guest atom complex increases from the Cs, Rb to K vacancy compounds.

The modal life times, τ_λ, are given by

$$\tau_\lambda(\omega) = \frac{1}{2\pi\Gamma_\lambda(\omega)} \tag{5.9.4}$$

where $\Gamma_\lambda(\omega)$ is the imaginary part of the self-energy, calculated using many body perturbation theory. Up to second order in the lowest an-harmonic term in the lattice Hamiltonian, $\Gamma_\lambda(\omega)$ is given by

$$\begin{aligned}\Gamma_\lambda(\omega) &= \frac{18\pi}{\hbar^2}\sum_{\lambda'\lambda''}\left|\Phi_{-\lambda\lambda'\lambda''}\right|'^2\left\{\left(n_{\lambda'}+n_{\lambda''}+1\right)\delta\left(\omega-\omega_{\lambda'}-\omega_{\lambda''}\right)\right.\\ &\left.+\left(n_{\lambda'}-n_{\lambda''}\right)\left(\delta\left(\omega+\omega_{\lambda'}-\omega_{\lambda''}\right)-\delta\left(\omega-\omega_{\lambda'}+\omega_{\lambda''}\right)\right)\right.\end{aligned} \tag{5.9.5}$$

$\Phi_{-\lambda\lambda'\lambda''}$ represents the strength of interaction between the three phonons labelled by $-\lambda, \lambda'$ and λ''. Here $-\lambda \equiv (-\mathbf{q}, j)$ and the occupation numbers $n_\lambda = \frac{1}{\exp(\frac{\hbar\omega_\lambda}{k_B T})-1}$. From Eq. (5.9.5) we notice that the line widths $\Gamma_\lambda(\omega)$ can have contributions from modes with different frequencies and different wavevectors[4]. Stronger phonon scattering leads to larger line widths which in turn leads to shorter relaxation times. Fig. (5.33) therefore suggests that the phonon scattering strength, represented by $\Phi_{-\lambda\lambda'\lambda''}$, is dramatically enhanced in the vacancy structure compared to the scattering strength in the Sn_{46} framework. It also indicates that the scattering strength in $K_8Sn_{44}\square_2$ is the strongest. This is consistent with our conclusion that the framework-vacancy-guest-atom interaction is the most obvious in $K_8Sn_{44}\square_2$ phonon spectrum.

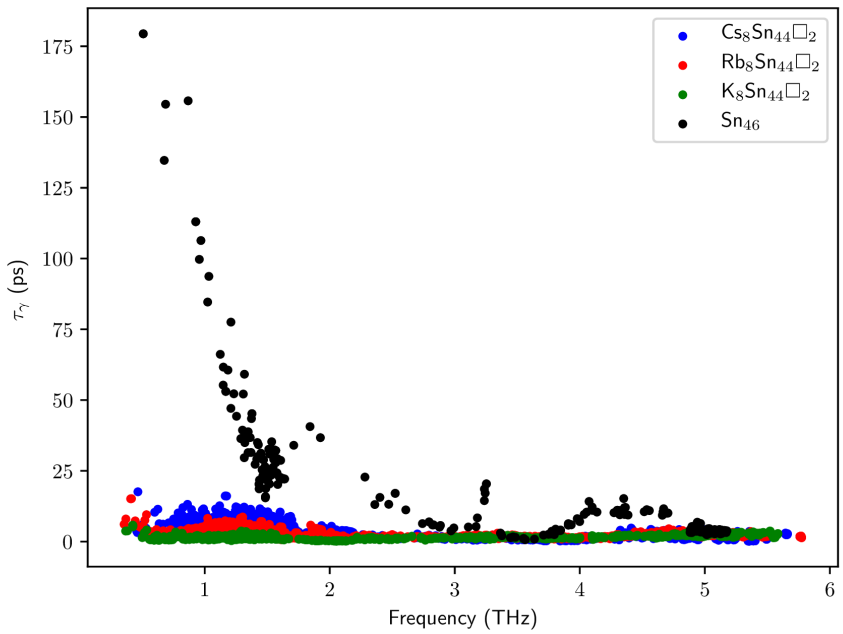


Figure 5.33: Modal relaxation times, τ_λ, for $A_8Sn_{44}\square_2$, (A = Cs, Rb, K) and the framework Sn_{46} as a function of frequency at 300 K.

5.9.1 Anisotropy in the thermal conductivity.

Figures (5.34), (5.35) and (5.36) shows the average cumulative lattice thermal conductivity κ_l for $K_8Sn_{44}\square_2$ and $Rb_8Sn_{44}\square_2$ and $Cs_8Sn_{44}\square_2$ at 300 K on the left and the temperature dependence of the average lattice thermal conductivity on the right. The introduction of vacancies into the prototype binary clathrate I Sn structure reduces the symmetry. This is reflected in the anisotropy of the lattice conductivity tensor. The insets in Fig. (5.34), (5.35) and (5.36), show the graph of the calculated lattice thermal conductivity anisotropy η, defined by: [163, 164]

$$\eta = \frac{\kappa_{ly} - \kappa_{lx}}{\kappa_{ly}} \tag{5.9.6}$$

where κ_{ly} and κ_{lx} are the lattice conductivities in the respective x- and y-directions. As can be seen from Figure (5.34), lattice thermal conductivities (κ_{lx} and κ_{ly}) decrease with an increase of temperature. Our result also shows an approximate 1/T dependence, typical of crystalline insulators.

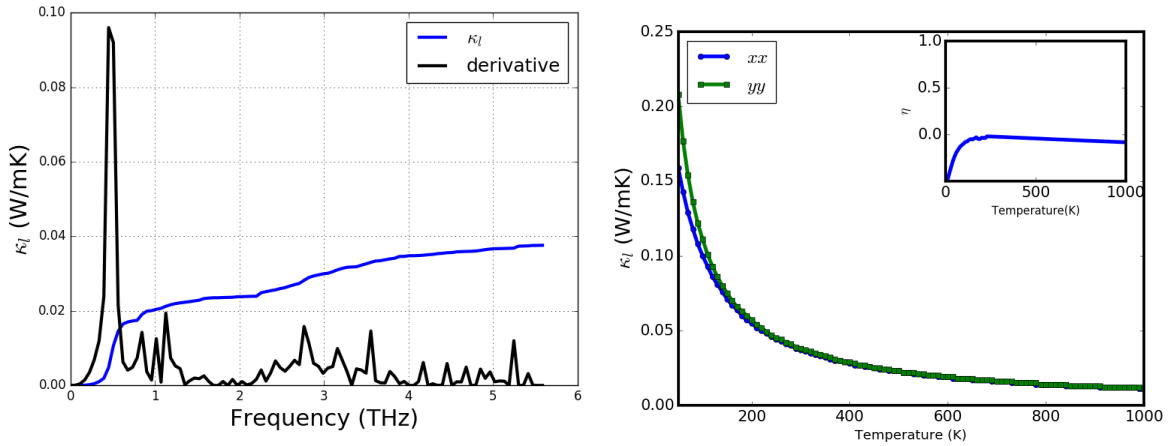
At 300 K the average thermal conductivities are 0.038, 0.077 and 0.11 W/mK for $K_8Sn_{44}\square_2$ and $Rb_8Sn_{44}\square_2$ and $Cs_8Sn_{44}\square_2$ respectively The calculated values are an oder of magnitude smaller than the experimentally estimated values about 1.0 W/mK at 300 K for $Cs_8Sn_{44}\square_2$ [21] and even lower than the value for Bi_2Te_3 (about 1.28 W/mK at 300 K). The estimated lattice thermal conductivities were approximated by using electrical resistivities and the Wiedemann-Franz law to estimate the electrical thermal conductivity contribution to the total thermal conductivity for poly-crystalline samples.

Lower values of κ_l were found in the x-direction for $K_8Sn_{44}\square_2$, and were therefore adopted for calculating the figure of merit ZT. In addition, Figure (5.34) (b) shows that κ_l decreases sharply from 0.16 W/mk at 10 K to 0.03 W/mK at 500 K, but decreases slowly to 0.02 W/mK at 1000 K for x-direction. The same trend is observed in the y- and z-direction. Although the sharp decrease here is from 0.22 W/mK to 0.03 W/mK between the same temperature range, while it decreases to 0.02 W/mK at 1000 K. As already noted the lattice conductivities decreases with increase in temperature, following the universal $\frac{1}{T}$ relation. The value of κ_{l_y} obtained is larger than that of κ_{l_x} at low temperatures between (0 K and 50 K), but no significant difference beyond this temperature. The anisotropic factor η calculated is 0.17 for $K_8Sn_{44}\square_2$ at 300 K. This ratio indicates that anisotropy in this material is low, but significant in the stability of the compound.

Figure (5.34) (b) show in the inset a graph of the anisotropic factor plotted against temperature with a flat plateau from 500 K. This implies the material can only be synthesized around this temperature [152]. Using the same description, Figure (5.35) (b), indicate that the κ_l for $Rb_8Sn_{44}\square_2$, decreases sharply from 0.4 W/mk at 0 K to 0.12 W/mK at 200 K, but decreases slowly to 0.02 W/mK at 1000 K in the x-direction. The same trend is observed in the y- and z-direction. Figure (5.36) (b), shows the plot of lattice thermal conductivity κ_l as a function of temperature for $Cs_8Sn_{44}\square_2$. Result indicate that κ_l decreases sharply from 0.65 W/mk at 0 K to 0.15 W/mK at 200 K, but decreases slowly to 0.023 W/mK at 1000 K for x-direction. The same trend is observed in the y- and z-direction.

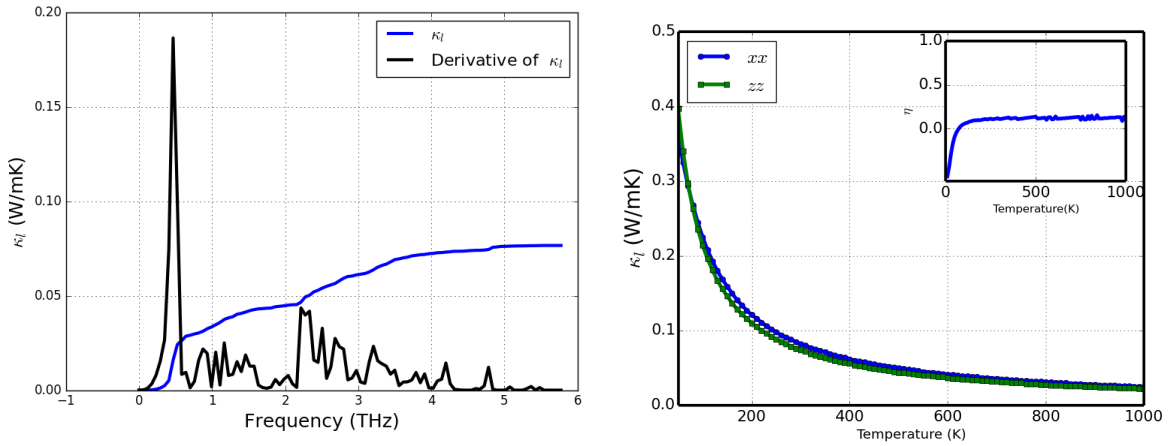
The lattice thermal conductivities of the three compounds were found to be very low compared to values expected for good thermoelectric materials. For instance the average calculated room temperature κ_l of 0.038, 0.077 and 0.11 W/mK for $K_8Sn_{44}\square_2$ and $Rb_8Sn_{44}\square_2$ and $Cs_8Sn_{44}\square_2$, respectively, are all considerably smaller than the out-of-plane and inplane values of 6.78 (0.79) W/mK for layered of $SnSe_2$ [165], which qualifies these materials as potential thermoelectric materials.

Typically the acoustic modes make the major contribution to the the thermal conductivity and the contribution from optical modes is relatively small [166]. For the Sn_{46} framework, the acoustic cut



(a) (b)

Figure 5.34: Plots of lattice thermal conductivity κ_l as a function of frequency at 300 K indicating major contribution to κ_l between 0 THz and 0.7 THz for (a) $K_8Sn_{44}\square_2$ (b) κ_l as a function of temperature with insert showing materials anisotropic factor plotted against temperature displaying the region of stability.



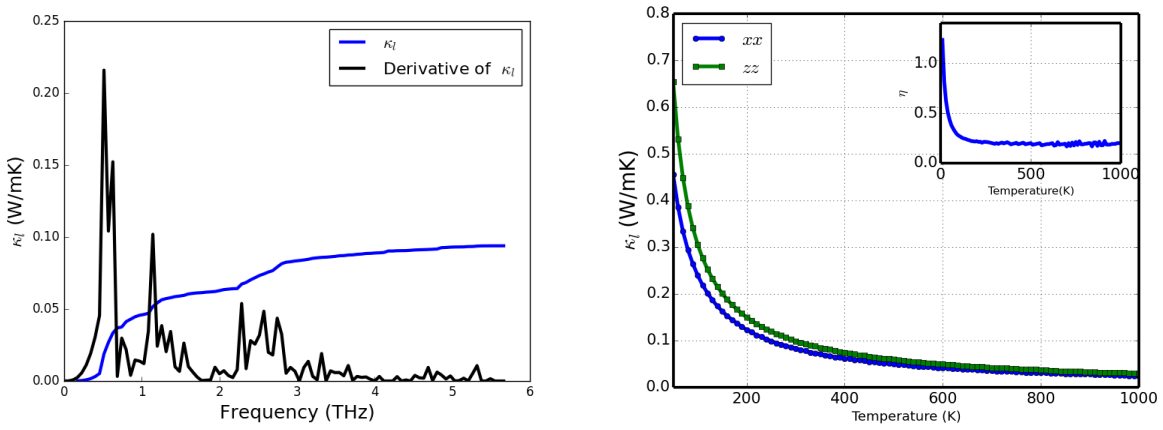
(a) (b)

Figure 5.35: Plots of lattice thermal conductivity κ_l as a function of frequency at 300 K indicating major contribution to κ_l between 0 THz and 0.5 THz for (a) $Rb_8Sn_{44}\square_2$ (b) κ_l as a function of temperature with insert showing materials anisotropic factor plotted against temperature displaying the region of stability.

off, taken as the highest frequency of the lowest band, is about 1.03 THz and the acoustic mode contribution to the total thermal conductivity is about 70%. Figures (5.34), (5.35) and (5.36) (a) show an initial sharp increase in the cumulative superconductivity as a function of frequency. The derivative of the cumulative values give an indication of the frequency ranges where the major contributions to the conductivities are found. The acoustic mode cut-offs for $K_8Sn_{46}\square_2$, $Rb_8Sn_{44}\square_2$ and $Cs_8Sn_{44}\square_2$ are approximately 0.61 THz, 0.34 THz and 0.55 THz, respectively. The contributions to the conductivities that can be associated with acoustic phonons are approximately 44%, 3% and 20% for the K, Rb and

Cs compounds, respectively. This is a very low contribution, especially for $Rb_8Sn_{44}\square_2$. For all three compounds there are contributions to the thermal conductivity over the whole frequency spectrum as can be seen from the finite values of the derivative of the cumulative thermal conductivities.

For all three vacancy compounds the vacancy-guest atom complexes have depressed the contribution to the thermal conductivity that comes from the acoustic modes. This is very noticeable for $Rb_8Sn_{44}\square_2$, with a striking 3% only from the acoustic modes.



(a) (b)

Figure 5.36: Plots of lattice thermal conductivity κ_l as a function of frequency at 300 K indicating major contribution to κ_l between 0 - 0.5 THz and 1 - 0.5 THz for (a) $Cs_8Sn_{44}\square_2$ (b) κ_l as a function of temperature with insert showing materials anisotropic factor plotted against temperature displaying the region of stability.

Our research question was to identify specifically what may be responsible for the lower thermal conductivity observed in binary type-I Sn clathrates with a view to engineering this material for better performance as thermoelectric material. We took our investigation further by plotting the cumulative lattice thermal conductivity at different temperatures as shown in Figures (5.34), (5.35) and (5.36) (b). Figures (5.37) and (5.38) show the plots of the derivative of the cumulative lattice thermal conductivity superimposed on the phonon partial density of states for the three compounds. The derivative of the cumulative κ_l does not follow the trends in the phonon density of states. For $Rb_8Sn_{44}\square_2$ and $Cs_8Sn_{44}\square_2$, the lower frequency, acoustic mode, contributions coincide with a high density of states in the guest atoms phonon spectra, but this is not the case for $K_8Sn_{44}\square_2$, where the acoustic mode contribution comes from a region where there is very little contribution from the guest atom phonon spectrum. For all three compounds there are relatively large contributions from optical modes in the 2-3 THz range, whereas the framework phonon spectra show relatively low densities of states. Only for $K_8Sn_{44}\square_2$ the guest atoms in the dodecahedral sites show a relatively high pDOS. Apart from the similarity in contributions in the 2-3 THz range, there is no obvious trend that changes as we go from $K_8Sn_{44}\square_2$ to $Rb_8Sn_{44}\square_2$ to $Cs_8Sn_{44}\square_2$.

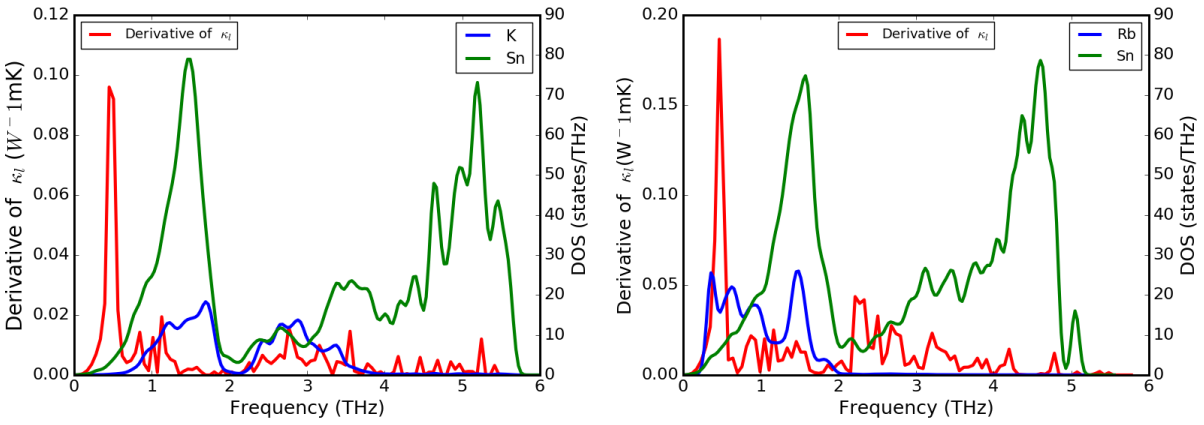


Figure 5.37: Plots of derivative of lattice thermal conductivity vibrations superimposed on the pDOS for (a)$K_8Sn_{44}\square_2$ (b) $Rb_8Sn_{44}\square_2$ as a function of frequency.

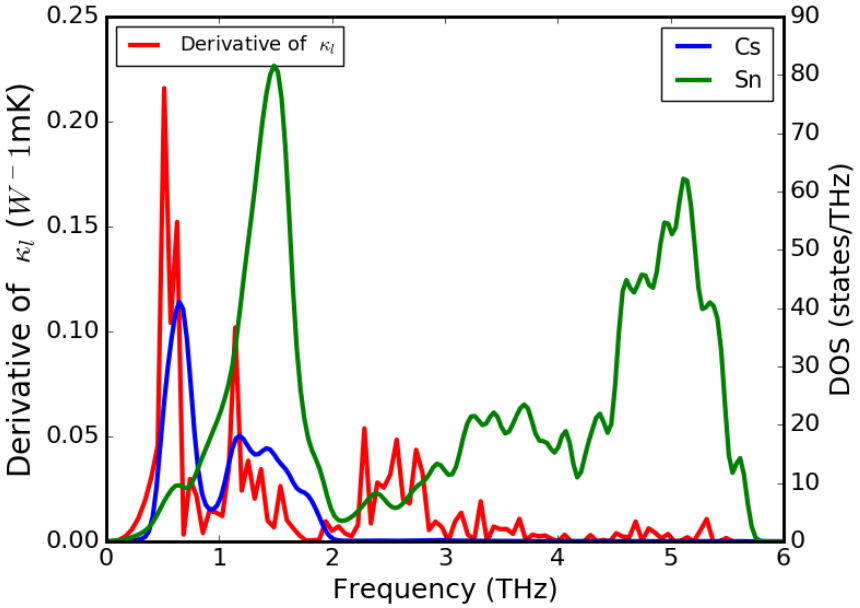
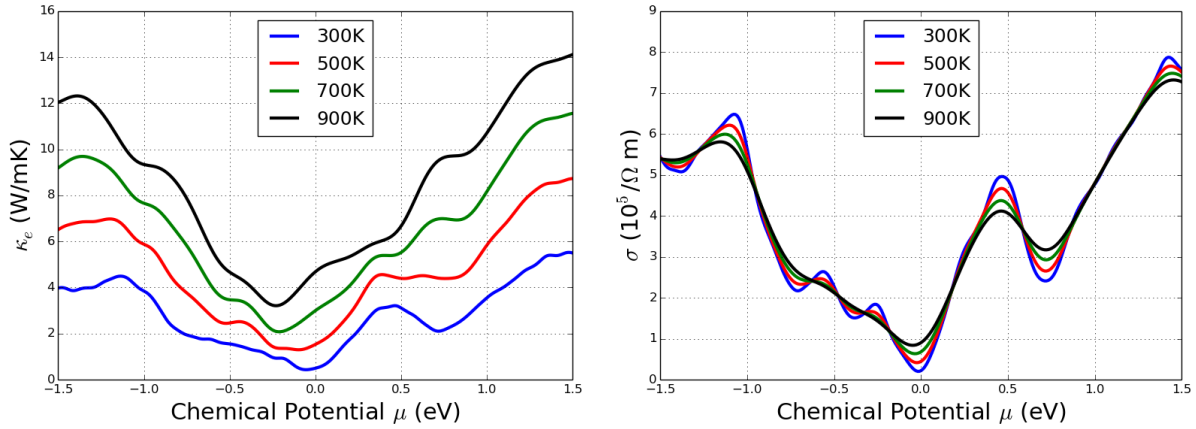


Figure 5.38: Plots of derivative of lattice thermal conductivity vibrations superimposed on the pDOS for $Cs_8Sn_{44}\square_2$ as a function of frequency.

5.10 Electronic Thermal Conductivity

In the linearised Boltzman Transport equations in the constant relaxation time approximation, Eq. (3.5), the electrical conductivity and the electronic thermal conductiviy are linear in the relaxation time. As constant relaxation time we used 10 fs in our work, based on experimental results for similar group-14 n-type polycrystalline samples of cubic Ge clathrates structures with symmetry space group $Pm\bar{3}n$ [16].

In Figures (5.39a), (5.40a) and (5.41a) below, we show the results for the electronic thermal conductivity κ_e as a function of the chemical potential (μ) at varying temperatures. Figure (5.39a) show that the κ_e increases with temperature, e.g. at $\mu = 1.5$ eV, κ_e increases from 5.60 W/mK (at 300 K) to 14.30 W/mK (at 900 K), in Figure (5.40a) κ_e increases with temperature at $\mu = 1.5$ eV, from 3.50 W/mK (at 300 K) to 9.50 W/mK (at 900 K) and in Figure (5.41a), κ_e increases with temperature at $\mu = 1.5$ eV, from 3.20 W/mK (at 300 K) to 9.80 W/mK (at 900 K), for the compounds $K_8Sn_{44}\square_2$, $Rb_8Sn_{44}\square_2$ and $Cs_8Sn_{44}\square_2$, respectively. Figures (5.39a), (5.40a) and (5.41a), also reveal a decrease in κ_e from 5.60 W/mK to 3.20 W/mK (at 300 K) and 14.30 W/mK to 9.20 W/mK (at 900 K), as we progress from the compounds $K_8Sn_{44}\square_2$, $Rb_8Sn_{44}\square_2$ and $Cs_8Sn_{44}\square_2$ respectively.



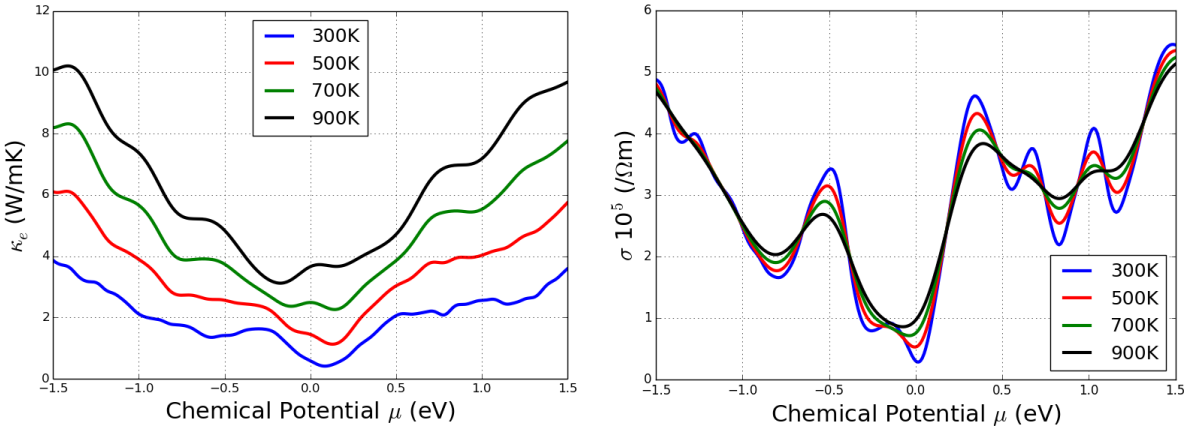
(a) κ_e with respect to chemical potential at the top of the valence band for $K_8Sn_{44}\square_2$.

(b) σ as a function of the chemical potential at different temperatures for $K_8Sn_{44}\square_2$.

Figure 5.39: κ_e and σ plotted as functions of the chemical potential for different temperatures. The origin of μ shifted to zero

In Figure (5.39b), we show the electrical conductivity σ, as a function of the chemical potential at different temperatures. Results show that σ is almost independent of temperature, which may be attributed to the compounds having equal contribution of majority hole(electron) carriers. The maximum value of the electrical conductivity of 79 $\times$ 10^4 Ω^{-1} m^{-1} occurs at 300 K which is higher for reported values (49.70 $\times$ 10^4 Ω^{-1} m^{-1}) of a similar $SnSe_2$ [165]. Electrical conductivity decreases from 79 $\times$ 10^4 Ω^{-1} m^{-1} (at 300K) to 73 $\times$ 10^4 Ω^{-1} m^{-1} (at 900 K) at $\mu = 1.5$ eV for the$K_8Sn_{44}\square_2$. Similarly, Figure (5.40b), show maximum value of the electrical conductivity of 58.96 $\times$ 10^4 Ω^{-1} m^{-1} occurs at μ = i.5 eV $Rb_8Sn_{44}\square_2$. Electrical conductivity decreases from 59 $\times$ 10^4 Ω^{-1} m^{-1} (at 300K) to 54 $\times$ 10^4 Ω^{-1} m^{-1} (at 900 K) at $\mu = 1.5$ eV. For the $Cs_8Sn_{44}\square_2$ Figure (5.41b), we observe maximum value of the electrical conductivity of 55.83 $\times$ 10^4 Ω^{-1} m^{-1} occurs at μ = -1.5 eV. Electrical conductivity decreases from 56 $\times$ 10^4 Ω^{-1} m^{-1} (at 300 K) to 53 $\times$ 10^4 Ω^{-1} m^{-1} (at 900 K)at μ = -1.5 eV.

We note that for materials p-type doping, the electrical conductivity does not show any clear trend,

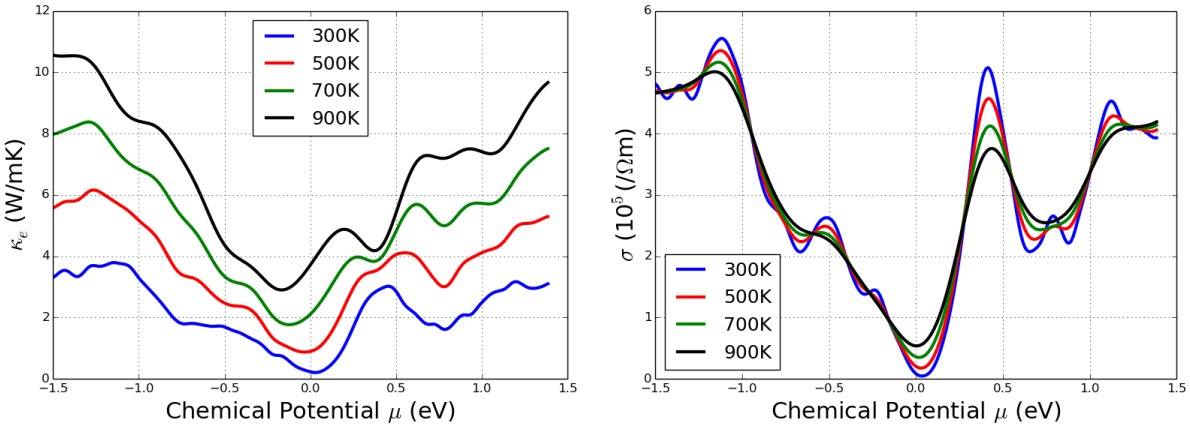


(a) κ_e with respect to chemical potential at the top of the valence band for $Rb_8Sn_{44}\square_2$.

(b) σ as a function of the chemical potential at different temperatures for $Rb_8Sn_{44}\square_2$.

Figure 5.40: κ_e and σ plotted as functions of the chemical potential for different temperatures. The origin of μ shifted to zero

although it decreases from from 65 $\times$ 10^4 Ω^{-1} m^{-1} to 55 $\times$ 10^4 Ω^{-1} m^{-1} (at 300 K) from $K_8Sn_{44}\square_2$ to $Cs_8Sn_{44}\square_2$. For materials n-type doping, the electrical conductivity does show any clear trend, as it decreases from from 79 $\times$ 10^4 Ω^{-1} m^{-1} to 40 $\times$ 10^4 Ω^{-1} m^{-1} (at 300 K) from $K_8Sn_{44}\square_2$ to $Cs_8Sn_{44}\square_2$. At different regions p- or n-type doping, the electrical conductivity can be viewed as almost constant.



(a) κ_e with respect to chemical potential at the top of the valence band for $Cs_8Sn_{44}\square_2$.

(b) σ as a function of the chemical potential at different temperatures for $Cs_8Sn_{44}\square_2$.

Figure 5.41: κ_e and σ plotted as functions of the chemical potential for different temperatures. The origin of μ shifted to zero

5.11 Thermoelectric Power Factor

The plot of the thermoelectric power factor ($S^2\sigma$), Figure (5.42), (5.43) and (5.44) shows a variation of power factor as a function of chemical potential. A full range of the plot Figure (5.42) shows that the power factor is highest for n-type doping K_8Sn_{44} from 81 $\times$ 10^{-5} W $m^{-1}K^{-2}$ at (300 K) to 180 $\times$ 10^{-5} W $m^{-1}K^{-2}$ at (900 K). Figure (5.43) shows two distinct regions indicating that the material is both active as a p-type as well as an n-type semiconductor. The n-type however has a higher power factor at higher temperatures (20 $\times$ 10^{-4} W/mK^2) than the p-type (12 $\times$ 10^{-4} W/mK^2). The power factor shows a distinct upper region from the graph Figure (5.44) with a power factor of 27 $\times$ 10^{-4} W/mK^2 n-type semiconductor within the range of a chemical potential of 5.62 eV and 6.12 eV. These are not values that can be realistically achieved with doping.

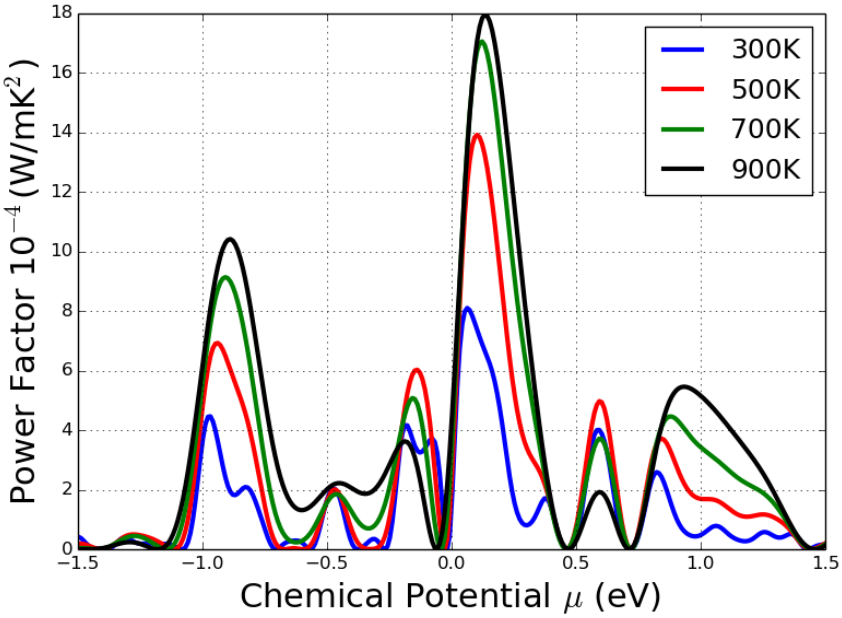


Figure 5.42: Variation of Power factor with respect to chemical potential at the top of the valence band as a function of temperature for $K_8Sn_{44}\square_2$. The origin of μ shifted to zero

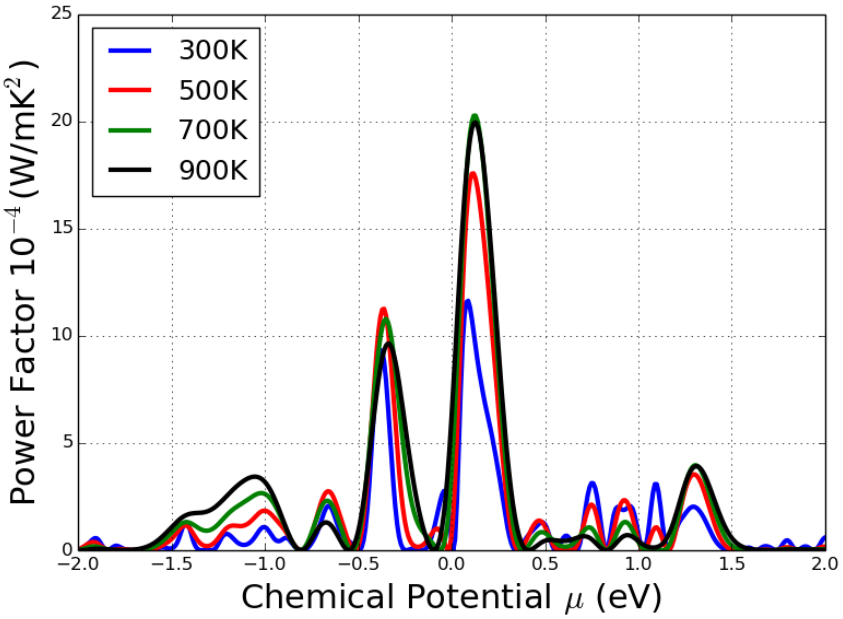


Figure 5.43: Variation of Power factor with respect to chemical potential at the top of the valence band as a function of temperature for $Rb_8Sn_{44}\square_2$. The origin of μ shifted to zero

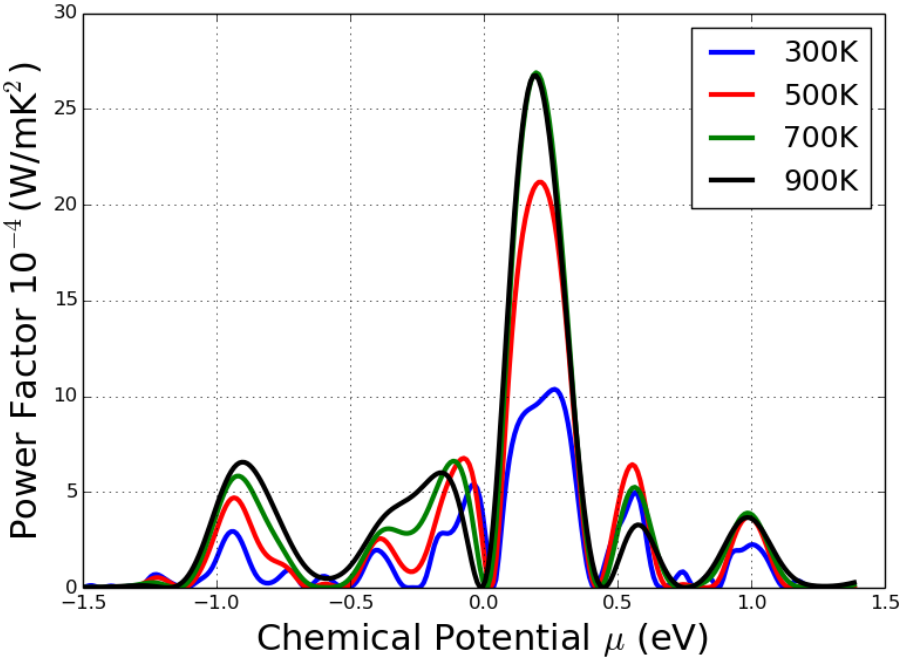
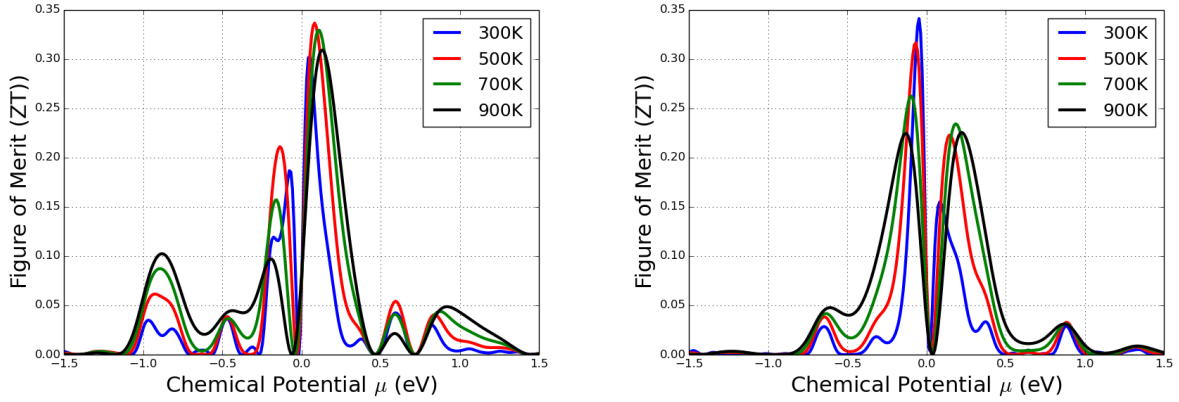


Figure 5.44: Variation of Power factor with respect to chemical potential at the top of the valence band as a function of temperature for $Cs_8Sn_{44}\square_2$. The origin of μ shifted to zero



(a) ZT in the x-direction

(b) ZT in the z-direction

Figure 5.45: Plots of figure of merit (ZT) as a function of chemical potential for $K_8Sn_{44}\square_2$ showing anisotropic behaviour. The origin of μ shifted to zero

5.12 Figure of Merit

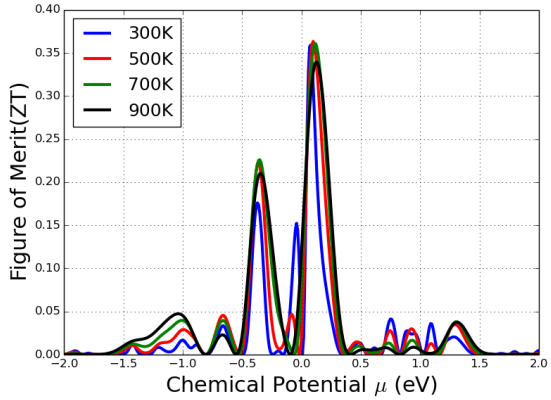
We calculated the figure of merit ZT, where κ is $\kappa_e + \kappa_l$, using the equation (1.0.3). A figure of merit larger than one is an indication that the material may be a good candidate as a component in a thermoelectric device.

A summary of our results is hereby presented for the three compounds. Figures (5.45a), (5.46a) and (5.47a) display the figure of merit ZT for $K_8Sn_{44}\square_2$, $Rb_8Sn_{44}\square_2$ and $Cs_8Sn_{44}\square_2$ system. The ZT increases with temperature in $K_8Sn_{44}\square_2$ (0.22 to 0.34), $Rb_8Sn_{44}\square_2$ (0.34 to 0.37) and $Cs_8Sn_{44}\square_2$ (0.48 to 0.52) for n-type in the x-direction. In the same manner, in Figures (5.45b), (5.46b) and (5.47b), the ZT increases with temperature in $K_8Sn_{44}\square_2$ (0.16 to 0.24), $Rb_8Sn_{44}\square_2$ (0.14 to 0.18) and $Cs_8Sn_{44}\square_2$ (0.25 to 0.34) for n-type in the z-direction.

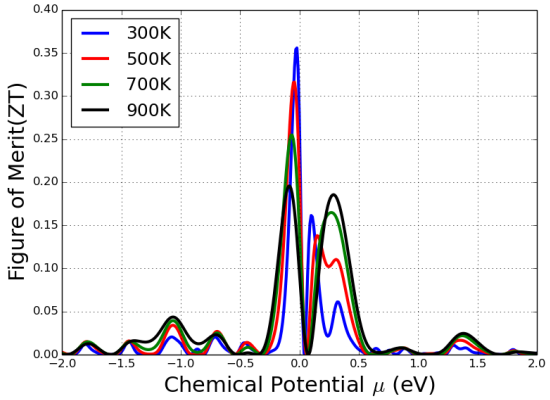
From the Figures (5.45a), (5.46a) and (5.47a), the ZT increases in $K_8Sn_{44}\square_2$ (0.10 to 0.22), $Rb_8Sn_{44}\square_2$ (0.18 to 0.23) and $Cs_8Sn_{44}\square_2$ (0.18 to 0.45) for n-type in the x-direction. Furthermore, in Figures (5.45b), (5.46b) and (5.47b), the ZT increases with temperature in $K_8Sn_{44}\square_2$ (0.23 to 0.34), $Rb_8Sn_{44}\square_2$ (0.20 to 0.35) and $Cs_8Sn_{44}\square_2$ (0.38 to 0.58) for the z-direction.

Therefore, these compounds can be used in thermoelectric devices. Results from Figure (5.45a) , (5.46a) and (5.47a), also show that the ZT in x-direction for the three compounds increases from $K_8Sn_{44}\square_2$ to $Cs_8Sn_{44}\square_2$ for both n-type and p-type material. Whereas there is decrease in ZT between the n-and p-type (0.22 to 0.10 for $K_8Sn_{44}\square_2$) Figure (5.45a), we observe increase in the ZT in the y-direction between the n- and p-type (0.16 to 0.23 for$K_8Sn_{44}\square_2$) Figure (5.45b). This result further elucidate our confirmation that the material is anisotropic. The plots of dimensionless figure of merit (ZT) as a function of chemical potential at varying temperature for $Rb_8Sn_{44}\square_2$ is shown in Figure (5.47). Result indicate that the ZT in out of plane direction (x-direction) is high for n-type with a value of 0.52 Figure (5.47a) contraste with 0.57 for in-plane direction (y/z -direction) Figure (5.47b). This result further elucidate our comfirmation that the material is anisotropic.

Figure (5.48) shows the calculated ZT for the three compounds. Cs_8Sn_{44} exhibits larger optimal ZTs compared to Rb_8Sn_{44} and K_8Sn_{44} with 2.34, 0.76 and 0.75 in the x-direction for n-type respectively. However Cs_8Sn_{44} and Rb_8Sn_{44} are optimized for n-type in the x-direction whereas K_8Sn_{44} si optimized

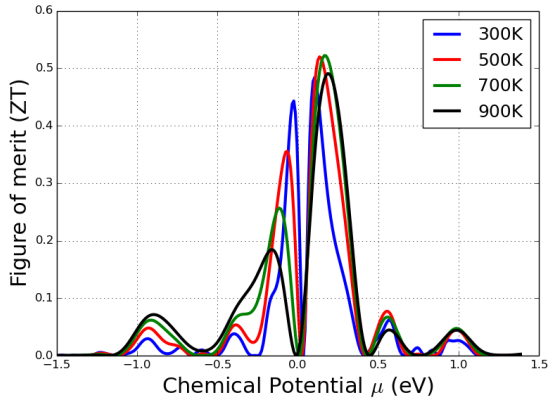


(a) ZT in the x-direction

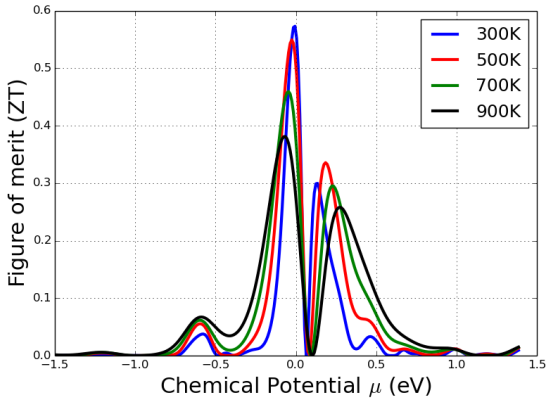


(b) ZT in the y-direction

Figure 5.46: Plots of figure of merit (ZT) as a function of chemical potential for $Rb_8Sn_{44}\square_2$ showing anisotropic behaviour. The origin of μ shifted to zero



(a) ZT in the x-direction



(b) ZT in the y-direction

Figure 5.47: Plots of figure of merit (ZT) as a function of chemical potential showing anisotropic behaviour. The origin of μ shifted to zero

Table 5.7: Dimensionless figure of merit (ZT) calculated at varying temperatures for n-type in the x- and y-directions for the three compounds

	K_8Sn_{44} ZT		Rb_8Sn_{44} ZT		Cs_8Sn_{44} ZT	
Temperature (K)	x-direction	y-direction	x-direction	y-direction	x-direction	y-direction
300.00	0.75	0.34	0.76	0.27	2.34	1.14
500.00	0.68	0.33	0.66	0.21	1.44	0.63
700.00	0.61	0.41	0.64	0.23	1.13	0.47
900.00	0.54	0.39	0.53	0.26	0.88	0.38

for p-type and in the y-direction. There is also a noticeable trend in reduction of ZT as the temperature increases, which infer that these materials are optimized at lower temperatures.

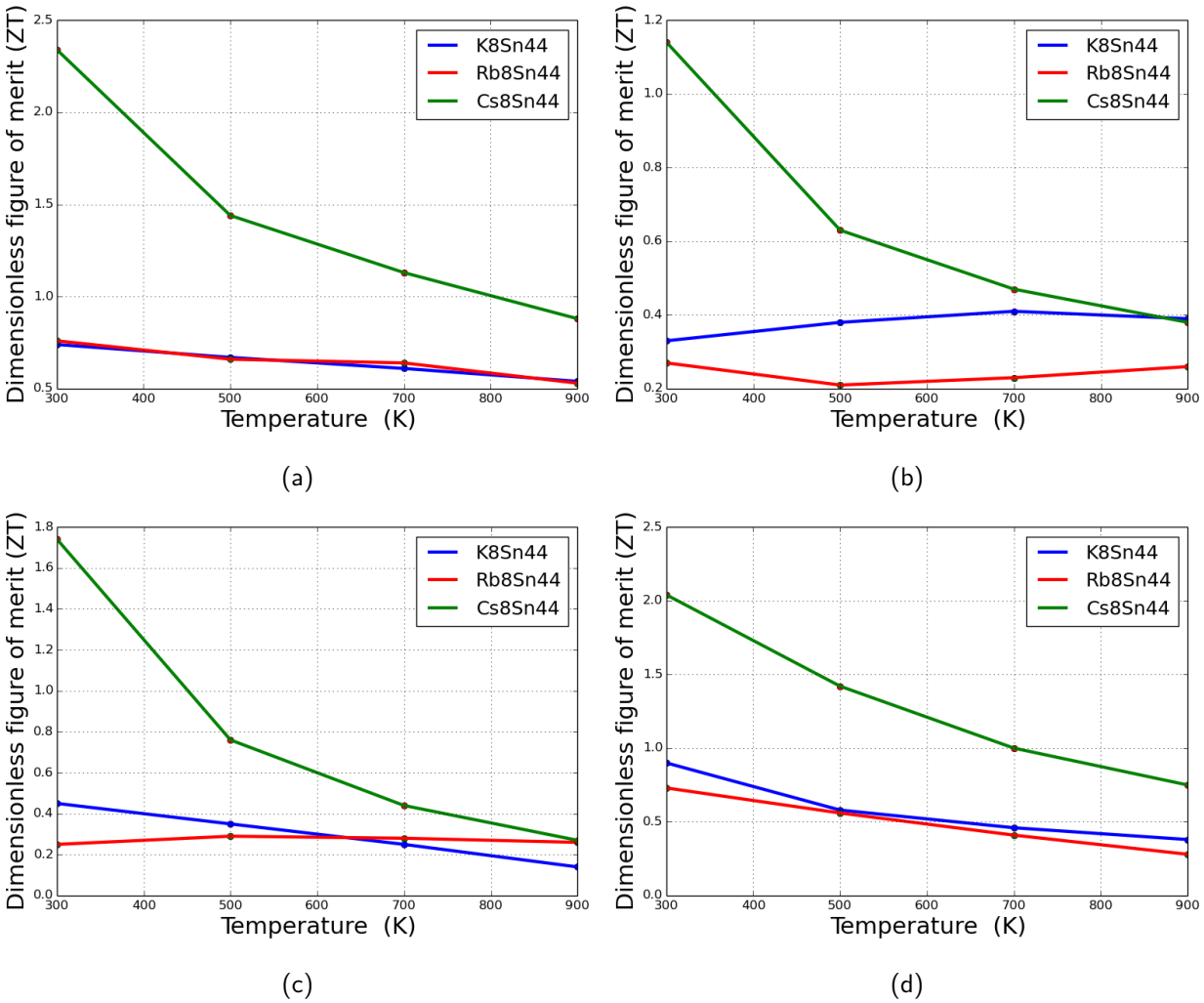


Figure 5.48: Plots of Calculated ZT for Cs_8Sn_{44}, Rb_8Sn_{44} and K_8Sn_{44} at varying temperatures for (a)n-type x-direction (b)n-type y-direction (c)p-type x-direction (d)p-type y-direction

6

Summary and Conclusion

In this thesis I have employed DFT first principle calculations to study the structural, electronic and transport properties of the binary type-I Sn clathrates including its vibrational properties.

In this work, I have used several functionals apart from LDA (commonly reported) to optimize the structure of the binary type-I Sn clathrates and included a calculation for the bandgap from a semi local (potential) functional mBJ, which frequently gives gaps in good agreement with experiment. The opening of the bandgap in these compounds is not significant. The optimized equilibrium structures with the LDA gave reasonable results and the thermoelectric calculations were based on LDA.

Chapter 5 is dedicated to discussion of the various results obtained and interpretation from it. From our results, the understanding of the effects of guest atoms on the thermal conductivity of binary type-I Sn clathrates was elucidated. For example the role of the guest atom vibration was compared to vibration of the entire system. Although the guest atom contribution to the lowering of the thermal conductivity is significant, the framework atoms contribution cannot be ignored. The various method I employed to understand the properties of these materials has helped to clarify what is responsible for the low thermal conductivity of this class of materials. This results I believe has partly answered my research question on what may be responsible for the low thermal conductivity in this binary type-I Sn clathrates.

We highlight the following as being significant in this thesis:

- Vacancies stabilise the stoichiometric compounds and remove the dynamical instability of K and Rb in the stoichiometric compounds.
- We used a relative study to analyse the influence of the guest-atom-vacancy complex on the thermal conductivity.
- The guest-atom-vacancy complex suppresses the acoustic mode frequencies.
- The guest-atom-vacancy complex marginally reduces the group velocities at low frequencies.
- The guest-atom-vacancy complex reduces the phonon life times at all frequencies and this is the main factor for the reduction in thermal conductivity in the vacancy compounds.
- Anomalously large mode Grüneisen parameters at low frequencies were calculated.
- $Cs_8Sn_{44}\square_2$ has an estimated figure of merit greater than 2 and is a potential thermoelectric material.

It is clear that there are still some outstanding questions which has not been addressed in this thesis. For example our study was limited to the high temperature modification, which from literature is a smaller cell. The $A_8Sn_{44}\square_2$ clathrate crystal structure have been structurally characterized as temperature dependent clathrate hydrate. Our calculation was limited to the smaller cell because of computational cost and facility to calculate and simulate a supercell of this already large primitive compound. The accurate modelling of phonon dispersion is required to adequately report its effect on heat suppression. Secondly, there are additional factors including lattice disorder and point defects, which cannot be decoupled from the rattling effect. We only focused on the rattling effect of the guest atoms in our study.

Appendix A

Density Functional Theory

One of the most challenging problems in computational materials physics is to describe the structure and electronic structure of a many-atom, many-electron system. The interactions between atoms and electrons are governed by the laws of quantum mechanics. The problem is to derive the properties of many-atom, many-electron systems from the quantum mechanical laws. Various electronic structure methods have been developed in the past. The most widely used method for structural and electronic structure calculations is Density Functional Theory [DFT]. In this part we introduce the concept of density functional theory and some of its approximations. Density functional theory is the theory of correlated many atom systems, which is based on the electronic density $n\mathbf{r}$ [89]. This is based on observation made by Hohenberg and Kohn in 1964 [167], that all the properties of a system can be obtained by the ground state charge density. It is one of the most reliable theories for predicting useful properties of materials. DFT provides explanations of phenomena observed in atoms, molecules, nano-structures and solids.

Many-body problem

The study and the analysis of the electronic structure of matter is done by solving the Schrödinger equation of many-atom systems. Considering the wave function Psi of a many-atom system, the general form of the Schrödinger equation can be written as follows (excluding spin for simplicity of notation):

$$\hat{\mathcal{H}}\Psi(\mathbf{R}_1, ..., \mathbf{R}_N; \mathbf{r}_1, ..., \mathbf{r}_N) = E\Psi(\mathbf{R}_1, ..., \mathbf{R}_N; \mathbf{r}_1, ..., \mathbf{r}_N) \tag{A.0.1}$$

where E is the energy of the system, $\mathbf{R}_i$ and $\mathbf{r}_i$ are respectively the positions of the nuclei and the positions of the electrons. N and n are respectively the number of nuclei and electrons of the system. The Hamiltonian operator $\hat{H}$ is given by:

$$\hat{\mathcal{H}} = \hat{T}_n + \hat{V}_n n + \hat{T}_e + \hat{V}_e e + \hat{V}_e n \tag{A.0.2}$$

In (A.0.2), $\hat{T}_n$, $\hat{T}_e$, $\hat{V}_n n$, $\hat{V}_e e$, $\hat{V}_e n$ represents the kinetic energy of the nuclei, kinetic energy of electrons, Potential energy of neutron-neutron, electron-electron, and electron-neutron interactions respectively.

$$\hat{T}_n = \sum_i^N -\frac{\hbar^2}{2M_i}\nabla^2_{\mathbf{R}_i} \tag{A.0.3}$$

where $\mathbf{R}_i$ represents the position of the atom i with mass M_i. The second term represents the interaction energy of the nuclei with charges $(Z_i e)$

$$\hat{V}_{nn} = \sum_{i<j}^{N} \frac{Z_i Z_j e^2}{|\mathbf{R}_i - \mathbf{R}_j|}. \tag{A.0.4}$$

The remaining terms in (A.0.2) are respectively the electronic kinetic energy, the electron-electron interaction energy and the electron-nuclei interaction energy operators:

$$\hat{T}_e = \sum_{i}^{N} -\frac{\hbar^2}{2m} \nabla^2_{\mathbf{r}_i} \tag{A.0.5}$$

$$\hat{V}_{ee} = \sum_{i<j}^{N} \frac{e^2}{|\mathbf{r}_i - \mathbf{r}_j|} \tag{A.0.6}$$

$$\hat{V}_{en} = \sum_{i=1}^{N} \sum_{j=1}^{N} \frac{Z_i e^2}{|\mathbf{R}_i - \mathbf{r}_j|}. \tag{A.0.7}$$

The standard step to solve (A.0.1) is the Born-Oppenheimer approximation in which the wave function of many-atom systems can be written as the product of the following form:

$$\Psi(\mathbf{R}_i, \mathbf{r}_j) = \Psi_n(\mathbf{R}_i)\Psi_e(\mathbf{R}_i, \mathbf{r}_j), \tag{A.0.8}$$

where $\Psi_n(\mathbf{R}_i)$ in (A.0.8) represents the wave function of the nuclei and $\Psi_e(\mathbf{R}_i, \mathbf{r}_j)$ is the electronic wave function. Substituting (A.0.8) in (A.0.2) we obtain the following equations

$$\hat{\mathcal{H}}_e \Psi_e(\mathbf{R}_i, \mathbf{r}_j) = (\hat{T}_e + \hat{V}_{ee} + \hat{V}_{en})\Psi_e(\mathbf{R}_i, \mathbf{r}_j) \tag{A.0.9}$$

which gives

$$\hat{\mathcal{H}}_e \Psi_e(\mathbf{R}_i, \mathbf{r}_j) = E^e \Psi_e(\mathbf{R}_i, \mathbf{r}_j) \tag{A.0.10}$$

and

$$\hat{\mathcal{H}}_n \Psi_n(\mathbf{R}_i) = (\hat{T}_n + \hat{V}_{nn} + E^e)\Psi_n(\mathbf{R}_i) \tag{A.0.11}$$

from which we get

$$\hat{\mathcal{H}}_n \Psi_n(\mathbf{R}_i) = E^n \Psi_n(\mathbf{R}_i). \tag{A.0.12}$$

If we consider the potential of the nuclei in (A.0.9) as static, and let $\hat{V}_{en} = \hat{V}_{ext}$, we get the time independent electronic Hamiltonian

$$\hat{\mathcal{H}} = \hat{T}_{ee} + \hat{V}_{ee} + \hat{V}_{ext}. \tag{A.0.13}$$

Let

$$\hat{\mathcal{H}} = \hat{F} + \hat{V}_{ext}, \tag{A.0.14}$$

where $\hat{F}$ is the sum of the kinetic and mutual Coulomb interaction energy operator and $\hat{V}_{ext}$ the external potential energy which describes the attraction between the electrons and nuclei.

Electronic density

Let $\mathbf{r}_i$ be the position of electron i, with spin coordinate $\sigma_i = \uparrow$ or $\downarrow$ and N the total number of electrons. The wave function of a many-electron system describes the quantum mechanical behaviour of that system and depends on the position and spin coordinates $\Psi_e(\mathbf{r}_1\sigma_1, \mathbf{r}_2\sigma_2, \ldots, \mathbf{r}_N\sigma_N)$. This wave function satisfies two conditions: firstly it must be orthonormal

$$\langle\Psi_e|\Psi_e\rangle = \sum_{\sigma_1\ldots\sigma_N} \int d\mathbf{r}_1 \int \mathbf{r}_2 \ldots \int d\mathbf{r}_N |\Psi_e(\mathbf{r}_1\sigma_1, \mathbf{r}_2\sigma_2, \ldots, \mathbf{r}_N\sigma_N)|^2 = 1, \tag{A.0.15}$$

and secondly it must be antisymmetric,

$$\Psi_e(\ldots, \mathbf{r}_i\sigma_i, \ldots, \mathbf{r}_j\sigma_j, \ldots) = -\Psi_e(\ldots, \mathbf{r}_j\sigma_j, \ldots, \mathbf{r}_i\sigma_i, \ldots). \tag{A.0.16}$$

In an electronic system, the electronic density $n(\mathbf{r})$ for a given state is defined as the number of electrons per unit volume at the point $\mathbf{r}$ for that state. The total number of electrons is given by

$$\int n(\mathbf{r}) d^3r = N, \tag{A.0.17}$$

The density can be expressed as the expectation value of the density

$$n(\mathbf{r}) = \sum_{i=1}^{N} \delta(\mathbf{r} - \mathbf{r}_i) \tag{A.0.18}$$

so that the relation between $n(\mathbf{r})$ and many-electron wave function is

$$n(\mathbf{r}) = N \sum_{\sigma_2\ldots\sigma_N} \int d\mathbf{r}_2 \int d\mathbf{r}_3 \ldots \int d\mathbf{r}_N |\Psi_e(\mathbf{r}_2\sigma_2, \mathbf{r}_3\sigma_3, \ldots, \mathbf{r}_N\sigma_N)|^2. \tag{A.0.19}$$

The expression on the right hand side looks similar to the wave-function normalization integration (A.0.15), but without one of the spatial integrals, and thus one coordinate is left free.
We define the electron spin density $n_\sigma(\mathbf{r})$ so that $n_\sigma(\mathbf{r})d^3r$ is the probability of finding the electron with spin σ in volume element d^3 at $\mathbf{r}$. Integrating over the coordinates and spin of the (N-1) other electrons we have

$$n_\sigma(\mathbf{r}) = \frac{1}{(N-1)!} \sum_{\sigma_2\ldots\sigma_N} \int d^3\mathbf{r}_2 \ldots \int d^3r_N N! |\Psi(\mathbf{r}\sigma, \mathbf{r}_2\sigma_2, \ldots, \mathbf{r}_N\sigma_N)|^2. \tag{A.0.20}$$

Combining (A.0.15) and (A.0.20) yields

$$\sum_\sigma \int d\mathbf{r} n_\sigma(\mathbf{r}) = \int (n_\uparrow(\mathbf{r}) + n_\downarrow(\mathbf{r})) = N. \tag{A.0.21}$$

Hartree-Fock Approximation

The Hartree-Fock (HF) approximation can be viewed as a variational method in which the wave functions of many-electron system have the form of an antisymetrised product of one-electron wave functions. This restriction leads to an effective Schrödinger equation for individual one-electron wave functions called orbitals with a potential determined by the orbitals occupied by the other electrons [168].

Let $\Psi^H(\mathbf{r})$ be a many-electron wave function for non-interacting electrons called Hartree wave function and given by

$$\Psi^H(\mathbf{r}_i) = \Phi_1(\mathbf{r}_1)\Phi_2(\mathbf{r}_2)\dots\Phi_N(\mathbf{r}_N) \tag{A.0.22}$$

with the index i running over all electrons and $\Phi_i(\mathbf{r}_i)$ are the one-electron wave functions. The total energy of the system is given by

$$E^H = \langle\Psi^H|\hat{\mathcal{H}}|\Psi^H\rangle \tag{A.0.23}$$

$$E^H = \sum_i \langle\Phi_i| - \frac{\hbar^2}{2m}\nabla^2_{\mathbf{r}} + \hat{V}_{ext}(\mathbf{r})|\Phi_i\rangle + \frac{e^2}{2}\sum_{ij(j\neq i)}\langle\Phi_i(\mathbf{r}_i)\Phi_j(\mathbf{r}')|\frac{1}{|\mathbf{r}-\mathbf{r}'|}|\Phi_i(\mathbf{r})\Phi_j(\mathbf{r}')\rangle. \tag{A.0.24}$$

On using a variational argument, we arrive at the single-electron Hartree equation

$$\left[-\hbar^2\frac{\nabla^2_{\mathbf{r}}}{2m} + \hat{V}_{ext}(\mathbf{r}) + e^2\sum_{j\neq i}\langle\Phi_j(\mathbf{r}')|\frac{1}{|\mathbf{r}-\mathbf{r}'|}|\Phi_j(\mathbf{r}')\rangle\right]\Phi_i(\mathbf{r}) = \epsilon_i\Phi_i(\mathbf{r}) \tag{A.0.25}$$

where ϵ_i are Lagrange multipliers introduced to take into account the normalization of the single-electron wave functions Φ_i. We define the Hartree potential as

$$V_i^H(\mathbf{r}) = e^2\sum_{j\neq i}\langle\Phi_j(\mathbf{r}')|\frac{1}{|\mathbf{r}-\mathbf{r}'|}|\Phi_j(\mathbf{r}')\rangle. \tag{A.0.26}$$

Since the Hartree wave function does not obey the Pauli Exclusion Principle [169], we incorporate the Fermionic nature of electrons in the many-body wave function so that we can build a wave function which is antisymmetrized for the Hartree wave function, this latter wave function changes sign when the coordinates of two electrons are interchanged. This is known as the Hartree Fock (HF) approximation. In order to describe the Hartree-Fock wave functions, we combine the Hartree version wave function to form a properly antisymmetrized wave function for the system [123]. For simplicity we will neglect the spin of electrons and keep only the spatial degrees of freedom. We then obtain the Hartree Fock wave function as

$$\Psi^{HF}(\mathbf{r}_i) = \frac{1}{\sqrt{N!}}\begin{vmatrix}\Phi_1(\mathbf{r}_1) & \Phi_1(\mathbf{r}_2) & \cdots & \Phi_N(\mathbf{r}_N)\\ \Phi_2(\mathbf{r}_1) & \Phi_2(\mathbf{r}_2) & \cdots & \Phi_N(\mathbf{r}_N)\\ \vdots & \vdots & & \vdots\\ \Phi_N(\mathbf{r}_1) & \Phi_N(\mathbf{r}_2) & \cdots & \Phi_N(\mathbf{r}_N)\end{vmatrix}.$$

The total energy with the Hartree-Fock wave function is given by

$$\begin{aligned}E^{HF} &= \langle\Psi^{HF}|\hat{\mathcal{H}}|\Psi^{HF}\rangle\\ &= \sum_i\langle\Phi_i| - \frac{\hbar^2}{2m}\nabla^2_{\mathbf{r}} + \hat{V}_{ext}(\mathbf{r})|\Phi_i\rangle\\ &+ \frac{e^2}{2}\sum_{ij(j\neq i)}\langle\Phi_i\Phi_j|\frac{1}{|\mathbf{r}-\mathbf{r}'|}|\Phi_i\Phi_j\rangle\\ &- \frac{e^2}{2}\sum_{ij(j\neq i)}\langle\Phi_i\Phi_j|\frac{1}{|\mathbf{r}-\mathbf{r}'|}|\Phi_j\Phi_i\rangle\end{aligned} \tag{A.0.27}$$

Minimising the energy a variational calculation gives

$$\left[-\frac{\hbar^2}{2m}\nabla^2\mathbf{r} + V_{ext}(\mathbf{r}) + V_i^H(\mathbf{r})\right]\Phi_i(\mathbf{r}) - e^2\sum_{j\neq i}\langle\Phi_j|\frac{1}{|\mathbf{r}-\mathbf{r}'|}|\Phi_i\rangle\Phi_j(\mathbf{r}) = \epsilon_i(\mathbf{r})\Phi_i(\mathbf{r}). \tag{A.0.28}$$

Equation (A.0.28) has an extra term in first term compare to the Hartree (A.0.25). This term describes exchange between electrons. Now construct a single-electron exchange density as

$$n_i^x(\mathbf{r},\mathbf{r}') = \sum_{j\neq i}\frac{\Phi_i(\mathbf{r})\Phi_i^*(\mathbf{r}')\Phi_j(\mathbf{r}')\Phi_j^*(\mathbf{r}')}{\Phi_i(\mathbf{r})\Phi_i^*(\mathbf{r})}. \tag{A.0.29}$$

A single-electron Hartree-Fock equation can be written as

$$\left[-\frac{\hbar^2\nabla_{\mathbf{r}}^2}{2m} + V_{ext}(\mathbf{r}) + V_i^H(\mathbf{r}) + V^x(\mathbf{r})\right]\Phi_i(\mathbf{r}) = \epsilon_i\Phi_i(\mathbf{r}) \tag{A.0.30}$$

where $V^x(\mathbf{r})$ is the exchange potential and given by

$$V_i^x(\mathbf{r}) = -e^2\int\frac{n_i^x(\mathbf{r},\mathbf{r}')}{|\mathbf{r}-\mathbf{r}'|}d\mathbf{r}' \tag{A.0.31}$$

The Hartree and the exchange potentials give the electron-electron interaction in the Hartree-Fock approximation

$$V_i^{HF} = e^2\int\frac{n(\mathbf{r}')}{|\mathbf{r}-\mathbf{r}'|}d\mathbf{r}' - e^2\int\frac{n_i(\mathbf{r}')+n_i^x(\mathbf{r},\mathbf{r}')}{|\mathbf{r}-\mathbf{r}'|}d\mathbf{r}'. \tag{A.0.32}$$

It follows that the total electron-electron interaction potential

$$V_i^{HF}(\mathbf{r}) = e^2\int\frac{n(\mathbf{r}') - n_i^{HF}(\mathbf{r},\mathbf{r}')}{|\mathbf{r}-\mathbf{r}'|}d\mathbf{r}'. \tag{A.0.33}$$

The Hartree-Fock is commonly used in chemistry and gives accurate results for a small number of electrons, but is inefficient in the study of solids.

Functional for exchange and correlation

There are basically three distinct types of approximations involved in a DFT calculation. One is conceptual, and concerns the interpretations involved of Kohn-Sham [KS] eigenvalues and orbitals as physical energies and wave functions. The second type of approximation is numerical, and concerns various methods for solving the KS equations, where you need to select a suitable basis function. The third type of approximation involves constructing an expression for the unknown exchange correlation xc functional $E_{xc}[n]$. The crucial quantity in the Kohn-Sham approach is the exchange-correlation energy which is expressed as a functional of the density $E_{xc}[n]$. In this section we present relevant approximation functionals used for our calculation, *viz.*, local density approximation [LDA] and generalized gradient approximation [GGA]. We also described in this section the hybrid functional which is a mixture of Hatree Fock exact exchange energy and an explicit density functional.

Local density approximation

Local-density approximations [LDA] are a class of approximations to the exchange correlation xc energy functional in density functional theory [DFT] that depend solely upon the value of the electronic density at each point in space (and not, for example, derivatives of the density or the Kohn−Sham orbitals). Many approaches can yield local approximations to the xc energy. However, overwhelmingly successful local approximations are those that have been derived from the homogeneous electron gas [HEG] model. In this regard, LDA is generally synonymous with functionals based on the HEG approximation, which are then applied to molecules and solids. Within the Kohn-Sham equation the exchange correlation energy is unknown, the greatest challenge in density functional theory is to find an accurate $E_{xc}[n]$. The most commonly used and successful approximation for calculating $E_{xc}[n]$ is the local density approximation (LDA). This approximation assumes that the density varies slowly. It replaces the exchange and correlation potential at each point of space by a uniform interacting electron gas. The exchange correlation energy can be expressed as:

$$E_{xc}^{LDA}[n] = \int d^3 r n(\mathbf{r}) \epsilon_{xc}^{unif}(n), \tag{A.0.34}$$

where $\epsilon_{xc}^{unif}(n)$ is the exchange correlation energy per particle of uniform electron gas of density n. The corresponding exchange correlation potential to (A.0.34) is

$$v_{xc}^{LDA}(\mathbf{r}) = \frac{\delta E_{xc}^{LDA}[n]}{\delta n(\mathbf{r})} = \left[\epsilon_{xc}^{unif} + n \frac{\partial \epsilon_{xc}^{unif}}{\partial n} \right]_{\mathbf{r}}. \tag{A.0.35}$$

The function ϵ_{xc}^{unif} can divided into two parts so that:

$$\epsilon_{xc}^{unif}(n) = \epsilon_{x}^{unif}(n) + \epsilon_{c}^{unif}(n), \tag{A.0.36}$$

where $\epsilon_{x}^{unif}(n)$ is the exchange. The accurate value of the exchange part is known from the Dirac exchange energy [170] and given by

$$\epsilon_{x}^{unif}(n) = -\frac{3}{4}\left(\frac{3}{\pi}\right)^{1/3} n^{1/3} = -\frac{3}{4}\left(\frac{9}{4\pi^2}\right)^{1/3} \frac{1}{r_s} = -\frac{0.458}{r_s} a.u., \tag{A.0.37}$$

where $r_s = (3/4\pi n)^{1/3}$ is the mean inter-electronic distance expressed in atomic units (a.u.).
Several approximations for correlation part are also available [171]. The most accurate results available have been calculated by Ceperley and Alder using the quantum Monte Carlo method in 1980 [172]. This correlation part has been parameterized by Perdew and Zunger (1981) for a spin-polarized (P) and spin-unpolarized (U) uniform electron gas. For the spin polarized electron gas the parametrized expression is of the form

$$\epsilon_c^P(n) = \begin{cases} A \ln r_s + B + C r_s \ln r_s + D r_s, & r_s \leq 1, \\ \gamma/(1 + \beta_1 \sqrt{r_s} + \beta_2 r_s), & r_s > 1. \end{cases}$$

For $r_s \leq 1$ the above expression derives from the random phase approximation, and has been calculated by Gell-Mann and Brueckner (1957). This is valid in the limit of very dense electronic systems, and fixes the values of the leading coefficents: $A^U = 0.0311. B^U = -0.048$. The relations given by Misawa in 1965 allows us to obtain the values for the fully polarized gas: $A^P = 0.015555, B^P = -0.0269$ and the remaining coefficients have been fitted to the quantum Monte Carlo results of Ceperley and Alder

(1980): $C^U = 0.002, D^U = -0.0116$, and $C^P = 0.0007, D^P = -0.0048$. The numerical values of the fitted coefficients of Perdew and Zunger are: $\gamma^U = -0.1423, \beta_1^U = 1.0529, \beta_2^U = 0.3334$ for unpolarized gas, and $\gamma^P = -0.0843, \beta_1^P = 1.3981, \beta_2^P = 0.2611$ for full polarized electron gas [173].
Another parameterization is the one proposed by Vosko *et al* [174],

$$\frac{\epsilon_c^{VWN}(r_s)}{A} = \ln\left(\frac{r_s}{F(\sqrt{r_s})}\right) + \frac{2b}{\sqrt{4c-b^2}}\tan^{-1}\left(\frac{\sqrt{4c-b^2}}{2\sqrt{r_s}+b}\right) - \frac{bx_0}{F(x_0)}\left[\ln\left(\frac{\sqrt{r_s}-x_0}{F(\sqrt{r_s})}\right) + \left(\frac{\sqrt{4c-b^2}}{2\sqrt{r_s}+b}\right)\frac{2(b-2x_0)}{\sqrt{4c-b^2}}\tan^{-1}\left(\frac{\sqrt{4c-b^2}}{2\sqrt{r_s}+b}\right)\right] \quad \text{(A.0.38)}$$

where $F(x) = x^2 + bx + c$, and A, b, c and x_0 are fitting coefficients that differ for the spin polarized and spin unpolarized cases.
The local density approximation predicts very accurately the physical properties of many systems. LDA does not work for system where the density has strong spatial variations or for weakly interacting systems such as van der Waals bonded molecules. It usually overestimates atomization energy, it overestimates correlation and underestimates exchange. LDA are important in the construction of more sophisticated approximations to the exchange-correlation energy, such as GGA or hybrid functionals, as a desirable property of any approximate exchange-correlation functional is that it reproduce the exact results of the HEG for non-varying densities. As such, LDA's are often an explicit component of such functionals.

Generalized gradient approximation

When the density increases rapidly such as in molecules, the LDA does not give a good approximation. The improvement of this approximation can be made by considering the gradient of the electron density, and so, called the generalized gradient approximation [GGA], in which the exchange correlation energy can be written as [115]

$$E_{xc}^{GGA}[n_\uparrow, n_\downarrow] = \int d^3r n(\mathbf{r})\epsilon_{xc}^{unif}\left(n_{\uparrow(r)}, n_\downarrow(r), \nabla n_\uparrow(r), \nabla n_\downarrow(r), \ldots\right) \quad \text{(A.0.39)}$$

$$= \int d^3r n(\mathbf{r})\epsilon_x^{unif} F_{xc}\left(n_{\uparrow(r)}, n_\downarrow(r), \nabla n_\uparrow(r), \nabla n_\downarrow(r), \ldots\right), \quad \text{(A.0.40)}$$

where F_{xc} is dimensionless and depends on the density and ϵ_x^{unif} is the exchange energy of the depolarize gas. The exchange correlation potential of GGA is obtained by including the derivatives regarding the gradient density so

$$v_{xc}^{GGA}(\mathbf{r}) = \frac{\delta E_{xc}^{GGA}}{\delta n(\mathbf{r})} = \left[\epsilon_{xc} + n\frac{\partial \epsilon_{xc}}{\partial n} - \nabla\left(n\frac{\partial \epsilon_{xc}}{\partial n}\right)\right]_{\mathbf{r}}. \quad \text{(A.0.41)}$$

From (A.0.41), there exists different parameterizations of F_{xc}. The parametrization realized by Perdew, Burke and Enzerhof (PBE) [115] is employed this work. Perdew, Burke, and Ernzerhof (PBE) defined the enhancement factor $F_x(n, \zeta, s)$ over the local exchange in (A.0.39) depends on the density n, magnetization density ζ (including spin), and the dimensionless density gradient $s = |\nabla n(\mathbf{r})|/(2k_F n)$. The factor can be written as

$$F_x(s) = 1 + k - \frac{k}{1 + \mu s^2/k}, \quad \text{(A.0.42)}$$

where $\mu = \beta(\pi^2/3) = 0.21951$, $\beta = 0.066725$ and $k = 0.804$. Other authors have proposed the same form, but with values of k and μ fitted empirically to a database of atomization energies . The

correlation energy takes the form of

$$E_c^{GGA} = \int n(\mathbf{r})(\epsilon_c^{unif}(n,\zeta) + H[n,\zeta,t])d^3r \tag{A.0.43}$$

with

$$H[n,\zeta,t] = (e^2/a_0)\gamma\phi^3 \ln\left\{1 + \frac{\beta}{\gamma}t^2\left[\frac{1+At^2}{1+At^2+A^2t^4}\right]\right\} \tag{A.0.44}$$

where $t = |\nabla(\mathbf{r})|/(2\phi k_s n)$ is the dimensionless density gradient, with $k_s = (4k_F/\pi a_0)$ being the Thomas Fermi screening wave number, and $\phi(\zeta) = [(1+\zeta)^{2/3} + (1-\zeta)^{2/3}]/2$ is a spin scaling factor. Here β has the same value for the exchange term $\beta = 0.066725$, and $\gamma = (1-\ln 2)/\pi^2 = 0.031091$. The function A has the form of

$$A = \frac{\beta}{\gamma}\left[\exp\{-\epsilon^{unif}/(\gamma\phi^3 e^2/a_0)\} - 1\right]^{-1}. \tag{A.0.45}$$

The correlation correction term H satisfies the following conditions:

(a) In slowing varying limit ($t \to 0$), H tends to the correct second order gradient expansion as

$$H \to (e^2/a_0)\beta\phi^3 t^2, \tag{A.0.46}$$

(b) In the rapidly varying limit ($t \to \infty$), H approaches the uniform electron gas correlation so

$$H \to -\epsilon_c^{unif}, \tag{A.0.47}$$

(c) H cancels the logarithmic singularity of ϵ_c^{unif} in the high density limit, thus forcing the correlation energy to scale to a constant under uniform scaling of the density so that

$$H \to -\frac{e^2}{a_0}\int d^3r n\gamma\phi^3 \ln\left[1 + \frac{1}{\chi s^2/\phi^2 + (\chi s^2/\phi^2)^2}\right] \tag{A.0.48}$$

where $s = |\nabla n|/2k_f n$ is dimensionless density gradient, and $\chi = (\beta/\gamma)c^2\exp(-\omega/\gamma) \simeq 0.72161$. The GGA for the exchange energy will be constructed by the following conditions:

(d) Under the uniform density, E_x must satisfy the scaling condition $\zeta = 0$, we obtain

$$E_x^{GGA} = \int d^3r n\epsilon^{unif}(n)F_x(s). \tag{A.0.49}$$

From (A.0.42), it recovers the correct uniform electron gas limit when $F_x(0) = 1$.

(e) The exchange energy obeys the spin scaling relationship

$$E_x[n_\uparrow, n_\downarrow] = (E_x[2n] + E_x[2n])/2. \tag{A.0.50}$$

(f) The LSDA linear response for ($s \to 0$) is recovered [115], thus

$$F_x(s) \to 1 + \mu s^2. \tag{A.0.51}$$

(g) It satisfies the local Lieb-Oxford bound [175]

$$E_x[n_\uparrow, n_\downarrow] \geq E_{xc}[n_\uparrow, n_\downarrow] \tag{A.0.52}$$

$$\geq -1.679e^2\int d^3r n^{4/3}. \tag{A.0.53}$$

For $F_x(s) \leq 1.804$ and $k = 0.804$. A few success stories of GGA as reported by Ziesche *et al.* [**?**] can be summarized as follows:

- The atomization energies of molecules are better in GGA than in LSD; for 20 simple molecules, the mean absolute error changes from $31.4 kcal/mol$ in LSD to $7.9 kcal/mol$ in GGA [119].
- The binding energy curves of the rare-gas dimers are more realistic in GGA than in LSD[176, 177, 178]
- While solid Fe is an fcc non-magnet in LSD, it is correctly a bcc ferromagnet in GGA [179].
- Lattice constants of alkali metals are about 4% too small in LSD, but right in GGA [180] Smaller corrections to LSD are found for Si and Ge.
- Lattice constants and bulk moduli of transition metals are better in GGA.
- Transition pressures from more open to more close-packed structures are often improved by GGA [181].
- For positron states and annihilation characteristics, the generalized gradient correction method to describe positron−electron correlation effects in solids shows systematic improvement over the LDA results.
- GGA has been successfully applied to the *ab initio* calculation of a monovacancy in Si.
- Gradient-corrected spin-polarized DFT methods have been successfully applied in the *ab initio* treatment of novel boron clusters and compounds of multi-layered boron clusters, nanotubes, boron sheets [182].
- Results for the controversially discussed p−T phase diagram of BN give an example of the high predictive power of DFT methods which include non-local corrections to the xc functional [183]. In addition to the last three points, which are related to microelectronics, Kaxiras *et al* and Heggie [184] stress the importance of approximations beyond LDA in *ab initio* calculations for device and process simulation.

  Failures: The situations in which LSD or GGA can fail badly seem to be of three types:

- When the KS non-interacting wavefunction is not a single Slater determinant, or when the non-interacting energies are nearly degenerate, the LSD and GGA exchangecorrelation holes can be unrealistic even very close to or on top of the electron [185]. Symmetry breaking, which worsens the spin densities, can improve the holes and energies in such cases. Also GGA works better for exchange and correlation together than for either alone [186].
- In an extended system, the exact hole may display a diffuse long-range tail which is not properly captured by either LSD or GGA. An example of a diffuse hole arises in the calculation of the surface energy of a metal [180].
- the ground state of one electron in the presence of two protons at very large separation: Half of the exact hole is localized on each proton, a situation which has no analog in the electron gas of uniform or slowly-varying density, and for which LSD and GGA make large self-interaction errors. A more subtle example is the long-range tail of the van der Waals interaction, which neither LSD nor GGA provide. The lattice constants of Kr and Xe crystals are too small in LDA, but too large with PBE GGA.

- Interactions between electrons in different shells e.g., between core and valence are not very well described.

. GGA improves on LDA for the quantities which are already successfully treated in LDA such as the total energies and hence binding energies, bond lengths and angles but ionisation energies based on Kohn-Sham energy eigenvalues are approximately the same as for LDA [**?**].

Hybrid functionals

Hybrid functionals are a class of approximations to the $E_{xc}[n]$ functional in DFT that incorporate a portion of exact exchange from HartreeFock theory with exchange and correlation from other sources. The exact $E_{xc}[n]$ functional is expressed in terms of the KohnSham orbitals rather than the density, so is termed an implicit density functional. One of the most commonly used versions is B3LYP, which stands for Becke, $3-$parameter, Lee-Yang-Parr. Hybrid functionals are constructed by mixing a fraction Hartree Fock [HF] exact exchange energy and an explicit density functional. The construction is motivated by predicting accurate gaps and accurate total energies [187]. This mixture can be justified by the *ab-initio* adiabatic connection formula in which the exchange correlation energy can be written as [188]

$$E_{xc} = \int_0^1 U_{xc}^{\lambda} d\lambda, \tag{A.0.54}$$

where λ is the interelectronic coupling strength parameters, U_{xc}^{λ} is the exchange correction potential energy at the intermediate coupling strength λ. This integral can be approximated using the mean-value theorem of integration as

$$E_{xc} \simeq \frac{1}{2}\left(U_{xc}^{0} + U_{xc}^{1}\right) = \frac{1}{2}\left(E_x + U_{xc}^{1}\right) \tag{A.0.55}$$

with U_{xc}^{0} is the exchange correlation potential energies of the Kohn-Sham system and U_{xc}^{1} is the exchange correlation potential energy of the full interaction real system. U_{xc}^{1} can be similarly approximated as LDA reads

$$U_{xc}^{1} \simeq U_{xc}^{LDA} = \int u_{xc}(n(\mathbf{r}))d^3r \tag{A.0.56}$$

The LDA-like functional u_{xc} is derived as an LDA approximation of potential energy [189]. Becke proposed the scheme as a method for incorporating exact exchange into DFT calculation called half-and-half theory so that the exchange correlation energy is given by

$$E_{xc}\frac{1}{2}E_x + \frac{1}{2}U_{xc}^{LDA} \tag{A.0.57}$$

which approximates (A.0.54) with $\lambda = 0$ and LDA for exchange correlation potential energy at $\lambda = 1$. The half-and-half theory is followed by three parameter of Becke such that the exchange correlation energy becomes

$$E_{xc} = E_{xc}^{LDA} + a_0\left(E_x - E_x^{LDA}\right) + a_x\left(E_x^{GGA} - E_x^{LDA}\right) + a_c\left(E_c^{GGA} - E_c^{LDA}\right), \tag{A.0.58}$$

whith a_0 , a_x, and a_c are empirical parameters. Perdew, Ernzerhof and Burke looked at the formula with $a_x = a_c = 1$ for the theoretical motivation which led to the hybrid function regarding the coupling-constant dependence for $a \simeq 0.25$. One of the most popular hybrid is the three parameters B3LYP functionals, mixing 80% of LDA with 20% of HF exchange and adding a certain amount of Becke 's correction ΔE_x^{B88}, the exchange correlation turn out to the following equation [188]

$$E_{xc}^{B3LYP} = 0.8E_x^{LDA} + 0.2E_x^{HF} + 0.72\Delta E_x^{B88} + 0.19E_c^{WN3} + 0.81E_x^{LYP}. \tag{A.0.59}$$

Here 81% of the semi-local Lee-Yang-Parr for correlation energy is used [187], the remaining part 19% of the local correlation energy is added from the Vosko-Wilk-Nusair correlation functional III (VWN3). Apart from B3LYP, several forms of the hybrid method have been proposed such as PBE0 and Heyd-Scuseria-Ernezerhof (HSE) functionals. These functionals differ on how the exact exchange energy is mixed in the energy functional [190]. The Hartree-Fock (HF) exact exchange energy E_x is given by

$$E_x^{HF} = -\frac{e^2}{2}\sum_{ij}\int\int d^3r d^3r' \frac{\phi_i^*(\mathbf{r})\phi_j^*(\mathbf{r}')\phi_i(\mathbf{r}')\phi_j(\mathbf{r})}{|\mathbf{r}-\mathbf{r}'|} \tag{A.0.60}$$

where ϕ_i are the occupied wave functions and i represents a quantum-number set comprising band and k-point indexes. The PBE0 hybrid is constructed by a rational mixing of 25% Fock exchange with 75% of well-know PBE exchange [189], and the exchange correlation energy of PBE0 takes the form of

$$E_{xc}^{PBE0} = \alpha E_x + (1-\alpha)E_x^{PBE} + E_c^{PBE} \tag{A.0.61}$$

Besides HSE has been found to give satisfactory results of energy gap on various solid systems. This is done by splitting the Coulomb operator into short-range (SR) and long-range (LR) parts [190]:

$$\frac{1}{r} = S_\mu(r) + L_\mu(r) = \frac{erfc(\mu r)}{r} + \frac{erf(\mu r)}{r} \tag{A.0.62}$$

then the HF exchange energy in (A.0.54) is calculated by the use of $S_\mu(r)$. The resulting exchange correlation energy of HSE is given as follows

$$E_{xc}^{HSE} = \alpha E_x^{SR}(\mu) + (1-\alpha)E_x^{PBE,SR}(\mu) + E^{PBE,LR}(\mu) + E_c^{PBE}. \tag{A.0.63}$$

In above equations, $r = |\mathbf{r}-\mathbf{r}'|$, and μ is the parameter that defines the range separation related to a characteristic distance $(2/\mu)$ at which the short-range interactions become negligible.

Van der Waals approximation

The van der Waals density functional [vdW-DF] [191] has attracted much attention, as it is able to describe the long-range van der Waals (vdW) forces in molecules and solids, which are described poorly by LDA as well as semilocal approximation GGA in DFT. The functional plays a role that complements well-established LDA and GGA. Furthermore, recent advances in vdW-DF methodology have shown that it is possible to perform accurate calculations of molecules, solids, and adsorption systems [192]. In static density functional theory using LDA and GGA, we can describe physical properties of many atoms, molecules and solids with good accuracy, but these approximations fail to describe the long range dispersion interactions, generally denoted as van der Waals interactions. Interaction between the layers of layered molybdenum chalcogenides are dominated by van der Waals-type interactions and are therefore important for this study. We distinguish two directions in the approaches undertaken to overcome this deficiency of DFT. Firstly we present the approach proposed by Grimme which leads to a better description of these interactions [193, 194]. To begin with, there is a term E_{Disp} added to the DFT interaction energy to obtain the total energy as

$$E_{tot} = E_{DFT} + E_{Disp} \tag{A.0.64}$$

where E_{DFT} is the DFT interaction energy computed with an approximate exchange correlation function, and E_{Disp} is the dispersion energy which is defined for periodic system as two-body interaction of the following form

$$E_{Disp} = -s_6\sum_{i=1}^{N}\sum_{j=i+1}^{N}\frac{C_6^{ij}}{\mathbf{r}_{ij}^6}f(\mathbf{r}_{ij}), \tag{A.0.65}$$

where $-s_6$ is a scaling factor and depends on the DFT used, C_6^{ij} are coefficients of dispersion and $f(\mathbf{r}_{ij})$ is the damping function. The damping function requires the specification of an atom pairwise cuttof radius $\mathbf{R}_r$ which determines in which interatomic distance region the dispersion is decreasing. The damping function can be written as

$$f(\mathbf{r}_{ij}) = \frac{1}{1 + e^{-d(\frac{\mathbf{r}_{ij}}{\mathbf{R}_r - 1})}}. \tag{A.0.66}$$

Here d is a damping parameter.
Secondly the groups of Lundqvist and Langreth have presented a density functional to treat the long-range dispersion. The key is the inclusion of a long range piece of the correlation energy, $E_c^{nl}[n]$ [195, 196], a fully nonlocal functional of the density n. In this functional, the exchange correlation energy takes the form of

$$E_{xc} = E_x^{GGA} + E_c^{LDA} + E^{nl} \tag{A.0.67}$$

where the exchange energy E_x^{GGA} uses the PBE GGA functional, and E_c^{LDA} is the LDA to the correlation energy. E_c^{nl} is the nonlocal energy term defined as

$$E_c^{nl} = \int d^3r \int d^3r' \, \phi(\mathbf{r}, \mathbf{r}')n(\mathbf{r}'). \tag{A.0.68}$$

Here ϕ is called Kernel and is given as a function of $Rf(\mathbf{r})$ and $Rf(\mathbf{r}')$, where $R = |\mathbf{r} - \mathbf{r}'|$ and $f(\mathbf{r})$ is a function of $n(\mathbf{r})$ and its gradient. In fact $f(\mathbf{r})$ is proportional to the exchange correlation energy density ϵ_{xc} of the gradient corrected LDA at the point $\mathbf{r}$ [197].

Appendix B

VASP

Bloch Theorem

In the self consistence Kohn-Sham approach, the large number of electrons in a system (macroscopic crystal) prohibits a direct solution of the Schrödinger equation. However, the solid has the periodic symmetry, and this can be accessed to reduce the size of the problem significantly using Bloch's theorem which allows the use of mapping the Schrödinger equation for an infinite periodic solid by solving the Schrödinger equation in a unit cell with a set of different boundary conditions. The wave function of one electron is symmetric, and can be written as

$$\Psi_{\mathbf{k}}(\mathbf{r}+\mathbf{R}) = e^{i\mathbf{k}\mathbf{R}}\Psi_{\mathbf{k}}(\mathbf{r}). \tag{B.0.1}$$

where **R** is the translation vector and can be written as:

$$\mathbf{R} = n_1 a_1 + n_2 a_2 + n_3 a_3 \tag{B.0.2}$$

with $n_i, i = 1, 2, 3$ are integers and a_i, are primitive lattice vectors and collect all equivalent points in space. This set of points is referred to as the Bravais lattice. The primitive unit cell is defined as the volume enclosed by the three primitive vectors:

$$\Omega = |a_1.(a_2 \times a_3)|. \tag{B.0.3}$$

The reciprocal lattice vectors are defined as:

$$a_i b_j = 2\pi\delta_{ij} \tag{B.0.4}$$

where $b_i, i = 1, 2, 3$, the volume of the reciprocal space is given by

$$|b_1.(b_2 \times b_3)| = \frac{(2\pi)^3}{|a_1.(a_2 \times a_3)|} = \frac{(2\pi)^3}{\Omega}. \tag{B.0.5}$$

Similarly to Equation (B.0.2) the vectors which connect all equivalent points in reciprocal space can be defined as

$$\mathbf{G} = m_1 b_1 + m_2 b_2 + m_3 b_3, \tag{B.0.6}$$

where $m_i, i = 1, 2, 3$. We can construct the dot product of any **R** vectors with **G**

$$\mathbf{RG} = 2\pi l, \quad l = n_1 m_1 + n_2 m_2 + n_3 m_3. \tag{B.0.7}$$

Consequently, $e^{i\mathbf{GR}} = 1$. For all $\mathbf{R}$ and $\mathbf{G}$ in the Bravais lattice, any function that has a periodicity can be written as

$$f(\mathbf{r}) = \sum_{\mathbf{G}} e^{i\mathbf{Gr}} f(\mathbf{G}) \tag{B.0.8}$$

with $f(\mathbf{G})$ Fourier transform components. Beside, Bloch's theorem assumes that when the potential in the one electron Hamiltonian has the translational periodicity of the Bravais lattice reads

$$V(\mathbf{r} + \mathbf{R}) = V(\mathbf{r}), \tag{B.0.9}$$

the one electron wave function has the same symmetry, so Equation (B.0.1) can be expressed as a product of the phase factor $\exp(i\mathbf{kr})$ multiplied by the function $u_{\mathbf{k}}(\mathbf{r})$ reads

$$\Psi_{\mathbf{k}}(\mathbf{r}) = e^{i\mathbf{kr}} u_{\mathbf{k}}(\mathbf{r}), \quad u_{\mathbf{k}}(\mathbf{r} + \mathbf{R}) = u_{\mathbf{k}}(\mathbf{r}). \tag{B.0.10}$$

The subscript $\mathbf{k}$ is an index for identifying the wave function. Bloch's theorem has two equivalent formulations whose the proof can be found in the book of solid state physics [123].

Projector augmented wave

Projector augmented wave (PAW) has been developed by P. Blöchl in 1994 [92, 93]. Since the wave functions for real materials in different regions of space have very different signatures, for example the bonding region, the wave function is fairly smooth, while close to the nucleus the wave function oscillates rapidly. The idea is to divide the wave function into parts and find a transformation on the wave functions which uses the fictitious wave functions with less oscillations close to the nucleus. It seeks to move from the Hilbert space of wave functions $\{|\Psi_n\rangle\}^4$ solutions of kohn-Sham equations to a pseudo-space (PS) of the wave function of Hilbert $\{|\tilde{\Psi}_n\rangle\}$ which are more softer by a linear transformation:

$$|\Psi_n\rangle = \mathcal{T}|\tilde{\Psi}_n\rangle. \tag{B.0.11}$$

The Kohn-Sham equations take the form

$$\mathcal{T}^\dagger \hat{\mathcal{H}}_s \mathcal{T}|\tilde{\Psi}_n\rangle = \epsilon_n \mathcal{T}^\dagger \mathcal{T}|\tilde{\Psi}_n\rangle, \tag{B.0.12}$$

since the wave function oscillates rapidly near the nuclei we can defined the projector $\mathcal{T}$ as

$$\mathcal{T} = \mathbb{I} + \sum_i \mathcal{T}_{\mathbf{R}_i} \tag{B.0.13}$$

where $\mathbb{I}$ is the identity operator, and $\mathcal{T}_{\mathbf{R}_i}$ is an operator acting within the sphere $\mathcal{S}_{\mathbf{R}_i}$ which surrounds the nuclei i at the points $\mathbf{R}_i$. Thus the wave functions $|\Psi_n\rangle$ and $|\tilde{\Psi}_n$ are identical except in the core regions. In order to define $\mathcal{T}_{\mathbf{R}_i}$, we consider two local basis centred on the nuclei i. The first basis $\{|\phi_i\rangle\}$ is related to the true wave function $|\Psi_n\rangle$ and the second $\{|\tilde{\phi}_i\rangle\}$ to $|\tilde{\Psi}_n\rangle$, therefore we are inside of $\mathcal{S}_{\mathbf{R}_i}$ and we obtain

$$|\Psi_n\rangle = \sum_i c_i|\phi_i\rangle \quad \text{and} \quad |\tilde{\Psi}_n\rangle = \sum_i \tilde{c}_i|\tilde{\phi}_i\rangle \tag{B.0.14}$$

The choice of these basis is define the local transformation the following expression of $|\phi_i\rangle$ as

$$|\phi_i\rangle = (\mathbb{I} + \mathcal{P}_{\mathbf{R}_i})\,|\tilde{\phi}_i\rangle, \tag{B.0.15}$$

therefore

$$\mathcal{T}_{\mathbf{R}_i}|\tilde{\phi}_i\rangle = |\phi_i\rangle - |\tilde{\phi}_i\rangle. \tag{B.0.16}$$

Also, there is no overlapping sphere of PAW, thus inside $\mathcal{S}_{\mathbf{R}_i}$ the wave function of the global system is given by

$$|\phi_i\rangle = \mathcal{T}|\tilde{\phi}_i\rangle = \sum_i \tilde{c}_i|\phi_i\rangle. \tag{B.0.17}$$

On using the unicity $c_i = \tilde{c}_i$, we notice that the wave functions $|\phi_n\rangle$ and $|\tilde{\phi}_n\rangle$ are the same in their basis. In addition $\mathcal{T}$ needs to be linear, it is necessary that c_i must also be linear to $|\tilde{\Psi}\rangle$ i.e there exists a family of projectors $\{|p_i\rangle\}$ such as:

$$c_i = \langle\tilde{p}_i|\tilde{\Psi}_n\rangle. \tag{B.0.18}$$

These projectors respect various properties. It turns out that the spheres of PAW do not overlap, inside of $\mathcal{S}_{\mathbf{R}_i}$ we obtain

$$|\tilde{\Psi}_n\rangle = \sum_i |\tilde{\phi}_n\rangle\langle\tilde{p}_i|\tilde{\Psi}_n\rangle. \tag{B.0.19}$$

Equation (B.0.19) leads to the closure relation reads

$$\sum_i |\tilde{\phi}_i\rangle\langle\tilde{p}_i| = \mathbb{I} \tag{B.0.20}$$

and the orthogonality gives

$$\langle\tilde{p}_i|\tilde{\phi}_j\rangle = \delta_{i,j}. \tag{B.0.21}$$

We do not have the constraint outside of the PAW sphere for the projectors and can be taken as zero in this case the local projector can be written as

$$\mathcal{T}_{\mathbf{R}_i} = \sum_i T_{\mathbf{R}_i}|\tilde{\phi}_i\rangle\langle\tilde{p}_i| \tag{B.0.22}$$

$$= \sum_i \left(|\phi_i\rangle - |\tilde{\phi}_i\rangle\right)\langle\tilde{p}_i|. \tag{B.0.23}$$

In summing considering all nucleus and boundaries conditions the global projector is given by

$$\mathcal{T} = \mathbb{I} + \sum_i \left(|\phi_i\rangle - |\tilde{\phi}_i\rangle\right)\langle\tilde{p}_i|. \tag{B.0.24}$$

In terms of wave functions and their projectors in the real space we obtain

$$\Psi_n(\mathbf{r}) = \tilde{\Psi}_n(\mathbf{r}) + \sum_i \sum_j \phi_j(\mathbf{r} - \mathbf{R}_i) - \tilde{\phi}_j(\mathbf{r} - \mathbf{R}_i)\langle\tilde{p}_j|\tilde{\Psi}_n\rangle \tag{B.0.25}$$

where $\tilde{\Psi}_n$ is obtained from Equation (B.0.12). In summary, the transformation of PAW method is given by Equation (B.0.25). The solutions of Kohn-Sham equations $\hat{\mathcal{H}}_s|\Psi_n\rangle = \epsilon_n|\Psi_n\rangle$, are functions which oscillate slowly far from the nuclei but rapidly close to the core, and they are decomposed as follows

- One part oscillates slowly with $\tilde{\Psi}_n$, solution of $\mathcal{T}^\dagger\hat{\mathcal{H}}_s\mathcal{T}|\Psi_n\rangle = \epsilon_n\mathcal{T}^\dagger\mathcal{T}|\Psi_n\rangle$ and requires a grid in Fourier space much coarser therefore a low cutoff energy.
- Another part oscillates rapidly but localized near the nuclei, which is deduced by projection on a local basis.

This method allows a gain of time for simulation and there is non loss of information on the real wave function.

Observable in the PAW method

We saw that PAW method calculates the wave function on a Fourier space in such a way that it transforms the local problem of eigenvalues of Kohn-Sham. In this part we are going to show how to obtain the observable quantities as expectation values of the pseudo-space wave functions. Let A be an operator and $\tilde{A}$ the associate pseudo-operator. The expectation value is independent on the basis and can be expressed by

$$\langle A \rangle = \sum_n f_n \langle \tilde{\Psi}_n | \tilde{A} | \tilde{\Psi}_n \rangle, \tag{B.0.26}$$

alternatively or as:

$$\langle A \rangle = \sum_n f_n \langle \tilde{\Psi}_n | \tilde{A} | \tilde{\Psi}_n \rangle \tag{B.0.27}$$

where n is the band index and f_n is the occupation of the state. The PS operator takes the form

$$\tilde{A} = \mathcal{T}^\dagger A \mathcal{T} \tag{B.0.28}$$

$$= A + \sum_{i,j} |\tilde{p}_i\rangle \left(\langle \phi_i | A | \phi_j \rangle - \langle \tilde{\phi}_i | A | \tilde{\phi}_j \rangle \right) \langle \tilde{p}_j |. \tag{B.0.29}$$

Also we can add an additional term arbritary in Equation (B.0.28) as:

$$B - \sum_{i,j} |\tilde{p}_i\rangle \langle \tilde{\phi}_i | B | \tilde{\phi}_j \rangle \langle \tilde{p}_j |, \tag{B.0.30}$$

where B is the operator localized in the PAW spheres. This latter equation does not change $\langle A \rangle$ but offers an additional degree of freedom to smooth pseudo-wave function. If we consider the projection operator $|\mathbf{r}\rangle\langle,\mathbf{r}|$ we obtain the charge density which follows the description given in Equation (B.0.28), hence the charge density is given by

$$n(\mathbf{r}) = \tilde{n}(\mathbf{r}) + n^1(\mathbf{r}) - \tilde{n}^1(\mathbf{r}), \tag{B.0.31}$$

where $\tilde{n}(\mathbf{r})$ is soft PS charge density given by

$$\tilde{n}(\mathbf{r}) = \sum_n f_n \langle \tilde{\Psi}_n | \mathbf{r} \rangle \langle \mathbf{r} | \tilde{\Psi}_n \rangle. \tag{B.0.32}$$

The quantities $\tilde{n}(\mathbf{r})$ and $\tilde{n}(\mathbf{r})$ are defined as

$$n^1(\mathbf{r}) = \sum_i \sum_{(n,j),k} f_n \langle \tilde{\Psi}_n | \tilde{p}_j \rangle \langle \phi_j | \mathbf{r} \rangle \langle \mathbf{r} | \phi_k \rangle \langle \tilde{p}_k | \tilde{\Psi}_n \rangle, \tag{B.0.33}$$

and

$$\tilde{n}^1(\mathbf{r}) = \sum_i \sum_{(n,j),k} f_n \langle \tilde{\Psi}_n | \tilde{p}_j \rangle \langle \tilde{\phi}_j | \mathbf{r} \rangle \langle \mathbf{r} | \tilde{\phi}_k \rangle \langle \tilde{p}_k | \tilde{\Psi}_n \rangle. \tag{B.0.34}$$

Equation (B.0.31) represents the charge density at point $\mathbf{r}$, it is the expectation value of the real space projection operator $|\mathbf{r}\rangle\langle\mathbf{r}|$ and described one of the physical quantity in the PAW method.

Appendix C

Boltzmann's Equation for Transport

The Boltzmann's equation of transport is the most successful and practical approach to study thermoelectric properties of materials. For a steady state, the Boltzmann's equation is given by

$$\left[\frac{\partial f_{\mathbf{k}(\mathbf{r},t)}}{\partial t}\right]_{diff} + \left[\frac{\partial f_{\mathbf{k}(\mathbf{r},t)}}{\partial t}\right]_{field} + \left[\frac{\partial f_{\mathbf{k}(\mathbf{r},t)}}{\partial t}\right]_{scatt} = 0 \tag{C.0.1}$$

where the subsripts $diff$, $field$ and $scatt$ denote the terms corresponding to diffusion, external field and scattering respectively,$f_{\mathbf{k}(\mathbf{r},t)}$ is the probability of having an electron (hole) with wave vector **k** and position **r** in space at a given time t. Note that **k**(**r**,t) is not for the equilibrum but for the steady state. At equilibrum, $f^0_{\mathbf{k}(\mathbf{r}}$ is the single particle Fermi distribution,

$$f^0_{\mathbf{k}(\mathbf{r}} = \frac{1}{\exp\left(\frac{\varepsilon_{\mathbf{k}}-\mu}{k_B T(\mathbf{r})}\right)+1}, \tag{C.0.2}$$

where $\varepsilon_{\mathbf{k}}$ is the energy corresponding to the wavevector **k**, μ is the chemical p[otential and k_B is the Boltzmann constant. The Boltzmann's equation states that the net rate of change in $f_{\mathbf{k}(\mathbf{r},t)}$ is zero for any **k** at given point in space. Applying Liouville's theorem for any **r**,

$$f_{\mathbf{k}(\mathbf{r},t)} = f_{\mathbf{k}(\mathbf{r}-t\mathbf{v}_{\mathbf{k}},0)}, \tag{C.0.3}$$

where $\mathbf{v}_{\mathbf{k}} = \partial\varepsilon_{\mathbf{k}}/\partial\mathbf{k}$. The diffusion term in (C.0.1) becomes

$$\frac{\partial f\mathbf{k}}{\partial f\mathsf{T}} = \frac{\exp(\frac{\varepsilon_{\mathbf{k}}-\mu}{k_B T})}{\left[\exp(\frac{\varepsilon_{\mathbf{k}}-\mu}{k_B T})+1\right]^2}\frac{\varepsilon_{\mathbf{k}}-\mu}{k_B T^2} = (-\frac{\partial f_{\mathbf{k}}}{\partial\varepsilon_{\mathbf{k}}})\frac{\varepsilon_{\mathbf{k}}-\mu}{T} \tag{C.0.4}$$

.

By analogy we follow a similar procedure and obtain equations for the field and scattering coefficients. Reader is directed to reference [95] for extensive information.

Band Interpolation

In solid-state physics, the band structure of a solid describes those ranges of energy, called energy bands, that an electron within the solid may have (allowed bands) and ranges of energy called band

gaps (forbidden bands), which it may not have. Band theory models the behavior of electrons in solids by postulating the existence of energy bands. It successfully uses a materials band structure to explain many physical properties of solids. Bands may also be viewed as the large-scale limit of molecular orbital theory.

Rigid Band Approximation

In rigid band approximation we model experimental compositions by taking a reference composition, for which full first-principles calculations can be made. The composition of this reference system should be chosen as close as possible to the experimental conditions. According to the rigid band approximation model the shape of the constant energy surfaces (hence the Fermi surface as well) and curve of density of states of the alloy are the same as those of the solvent metal, provided; (1) excess charge of the solute atoms localizes around them, (2) mean free path of the electrons is much greater than the lattice spacing of the alloy and (3) electron states of interest in the pure solvent are all in one energy band, which is greatly separated in energy from the other bands [198]. The only effect of the addition of the solute, given that its valence is greater than that of the solvent, is the addition of electrons to the valence band. This results to swelling the Fermi surface and filling the density of states curve to a higher energy.

Steps in transport properties calculation

We first perform a self-consistent first principles calculation on the system in order to obtain a set of Bloch energy bands from which maximally localised wannier functions are then constructed. Calculation of the Bloch states $|u_{nk}\rangle$, where u_{nk} is the set of Bloch functions obtained at each k-point, is performed using density-functional theory in the LDA approximation [114]. We computed Bloch states and the overlaps from ground state density and the maximally-localised Wannier functions (MLWF) on a $4\times4\times4$ mesh [102]. MLWFs are calculated using wannier90 program [102] and the band structure is plotted along the special k-path as shown in Figure (4.1). In order to obtain wannier functions that are able to reproduce the lowest energy conduction states as well as disentagling the valence band, we proceed as follows: We note that only the energy range k_BT around the Fermi level is relevant for transport properties, hence we carefully select the relevant bands when calculating the WFs. We also chose a frozen energy window E_{froz} roughly above the bottom of the conduction band, which is sufficient for our calculations. We thereafter calculate the MLWFs using iteractive minimization algorithm of Wannier90, employing atom-centred Gaussian-type orbitals with the number of bands for the calculation set at a reasonable number of bands [102]. Once the MLWFs are obtained, we then proceed to use them as a basis set to interpolate band velocities and calculate the transport properties using BoltzWann code [32]. The bands were interpolated on a $40\times40\times40$ mesh and the transport distribution function (TDF) calculated using a relaxation time of 10 *fs* for the system. The relaxation time of 10 *fs* was chosen from experimental results of Ge-based clathrates [128]. We could safely use this value as our system contains a group 14 element (Sn) which is common to all the binary systems studied in this work. This simple time approximation is adopted in first principles calculations which is a good approximation for bulk materials [129, 130]. The position of chemical potential (μ) plays an important role with regard to the transport properties. The position of μ in the band structure determines which electrons in the valence or conduction band take part in the electronic transport, commonly used as a criterion for noting both the conductivity and the Seebeck coefficient.

Appendix D

Phonon Calculations

We present in this part the phonon calculations [4]. The methods for *ab initio* calculations of phonon frequencies fall into two broad classes: the linear-response approach and the direct approach. In the linear-response techniques, the dynamical matrix is expressed in terms of the inverse dielectric matrix describing the response of the valence electron density to a periodic perturbation of the crystalline lattice. For semiconductors and transition metals, the realization of the linear-response approach is much more difficult, since the full dielectric matrix must be calculated in terms of the electronic eigenfunctions and eigenvalues of the perfect crystal. In the direct approach the energy of a phonon, i.e. of a periodic distortion of the crystalline lattice, is calculated as a function of the displacement amplitude in terms of the difference in the energies of the distorted and the unperturbed lattices (frozen-phonom method) [100]. The approach is restricted to phonons whose wavelength is compatible with the periodic boundary conditions applied to the supercell used in the calculations. Another variant of the direct or total-energy approach concentrates on the forces on the atoms induced by the displacements of other atoms in the supercell. From the forces calculated via the Hellmann- Feynman theorem, certain elements of the force constant matrix can be evaluated. By displacing entire planes of atoms, interplanar force constants may be calculated [100, 101], allowing for the determination of the phonon dispersion relations in certain symmetry directions. Work flow of phonopy is shown schematically on Figure (D.1).

In this method, the phonon frequencies calculation is based on the fact that the force constant matrix expresses the proportionality between displacements and forces, when the displacements are small enough for this relationship to be linear. All that has to be done, in principle, is to displace a single atom in celll while all other atoms being held fixed at their equilibrium positions. If this procedure is repeated, all the elements of the force-constant matrix can be obtained. Translational invariance implies that the number of separate calculations required to do this is at most three times the number of atoms in the primitive cell, but for most materials symmetry relations can be used to reduce this number substantially. This strategy, sometimes called the small displacement method [140, 141] is what is adopted in this work. For extensive review and procedure see [140].

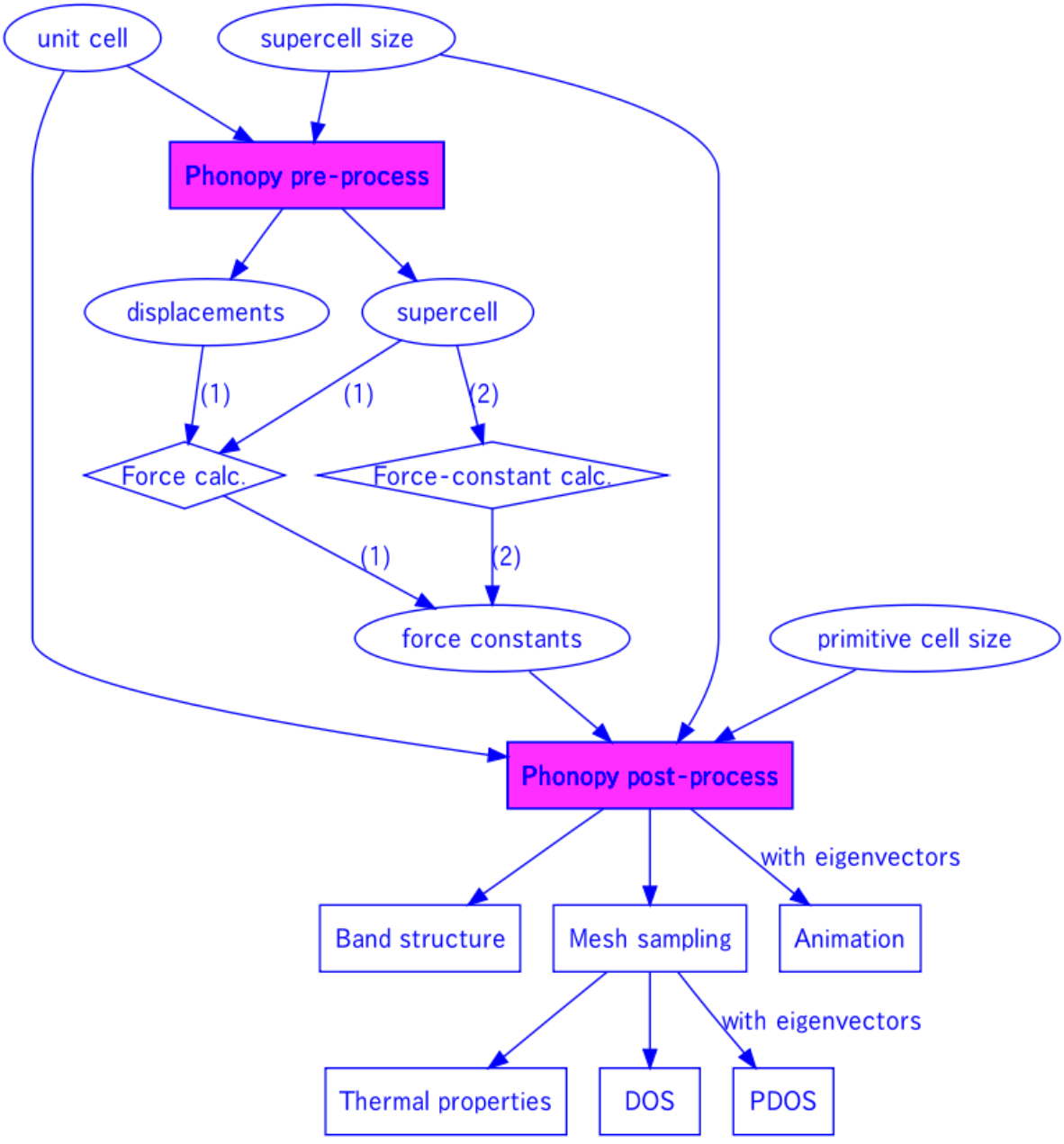


Figure D.1: Work flow of phonon calculation [4]

References

[1] C. W. Myles, J. Dong, and O. F. Sankey, "Theoretical investigation of carbon-based clathrate materials," in *APS Meeting Abstracts*, 2004.

[2] W. contributors, "Brillouin zone — wikipedia, the free encyclopedia," 2017. [Online; accessed 12-February-2018].

[3] T. Takabatake, K. Suekuni, T. Nakayama, and E. Kaneshita, "Phonon-glass electron-crystal thermoelectric clathrates: Experiments and theory," *Reviews of Modern Physics*, vol. 86, no. 2, p. 669, 2014.

[4] A. Togo and I. Tanaka, "First principles phonon calculations in materials science," *Scripta Materialia*, vol. 108, pp. 1–5, 2015.

[5] T. M. Tritt and M. Subramanian, "Thermoelectric materials, phenomena, and applications: a bird's eye view," *MRS bulletin*, vol. 31, no. 03, pp. 188–198, 2006.

[6] T. J. Seebeck, "Ueber die magnetische polarisation der metalle und erze durch temperaturdifferenz," *Annalen der Physik*, vol. 82, no. 3, pp. 253–286, 1826.

[7] J. Peltier, "Investigation of the heat developed by electric currents in homogeneous materials and at the junction of two different conductors," *Ann. Chim. Phys*, vol. 56, no. 1834, p. 371, 1834.

[8] C. Kittel, *Introduction to solid state physics*. Wiley, 2005.

[9] G. Mahan and L. Woods, "Multilayer thermionic refrigeration," *Physical Review Letters*, vol. 80, no. 18, p. 4016, 1998.

[10] G. Mahan and J. Sofo, "The best thermoelectric," *Proceedings of the National Academy of Sciences*, vol. 93, no. 15, pp. 7436–7439, 1996.

[11] G. Nolas, D. Morelli, and T. M. Trii, "Skutterudites: A phonon-glass-electron crystal approach to advanced thermoelectric energy convertion application," *Annual Review of materials Science*, vol. 29, no. 1, 1999.

[12] A. F. Ioffe, *Physics of semiconductors*. Infosearch, 1960.

[13] J. Shi, *Ab initio prediction of crystalline phases and their electronic properties: from ambien to extreme pressres*. PhD thesis, Université de Lyon, 2017.

[14] L. Lorenz, "On the thermal and electrical conductivities of metals," *Ann. Physik*, vol. 13, no. 3, pp. 422–447, 1881.

[15] A. Sommerfeld, "Zur elektronentheorie der metalle," *Naturwissenschaften*, vol. 15, no. 41, pp. 825–832, 1927.

[16] G. Nolas, J. Cohn, G. Slack, and S. Schujman, "Semiconducting ge clathrates: Promising candidates for thermoelectric applications," *Applied Physics Letters*, vol. 73, no. 2, pp. 178–180, 1998.

[17] D. M. Rowe, *CRC handbook of thermoelectrics*. CRC press, 1995.

[18] M. M. Koza, M. R. Johnson, i. Viennois, H. Mutka, L. Girard, and D. Ravot, "Breakdown of phonon glass paradigm in La-and Ce-filled $\mathrm{Fe_4Sb_{12}}$ skutterudites," *Nature Materials*, vol. 7, no. 10, p. 805, 2008.

[19] K. Mastronardi, D. Young, C.-C. Wang, P. Khalifah, R. Cava, and A. Ramirez, "Antimonides with the half-heusler structure: new thermoelectric materials," *Applied physics letters*, vol. 74, no. 10, pp. 1415–1417, 1999.

[20] D.-Y. Chung, L. Iordanidis, K.-S. Choi, and M. G. Kanatzidis, "Complex chalcogenides as thermoelectric materials: a solid state chemistry approach," *BULLETIN-KOREAN CHEMICAL SOCIETY*, vol. 19, pp. 1283–1293, 1998.

[21] J. Cohn, G. Nolas, V. Fessatidis, T. Metcalf, and G. Slack, "Glasslike heat conduction in high-mobility crystalline semiconductors," *Physical Review Letters*, vol. 82, no. 4, pp. 779(1)–(5), 1999.

[22] A. Kaltzoglou, *Synthesis, Characterization and Physical Properties of Semiconducting Clathrate Compounds*. PhD thesis, Universität München, 2009.

[23] G. K. Madsen, K. Schwarz, P. Blaha, and D. J. Singh, "Electronic structure and transport in type-i and type-viii clathrates containing strontium, barium, and europium," *Physical Review B*, vol. 68, no. 12, p. 125212, 2003.

[24] M. Christensen, S. Johnsen, and B. B. Iversen, "Thermoelectric clathrates of type I," *Dalton Transactions*, vol. 39, no. 4, pp. 978–992, 2010.

[25] M. Christensen, A. B. Abrahamsen, N. B. Christensen, F. Juranyi, N. H. Andersen, K. Lefmann, J. Andreasson, C. R. Bahl, and B. B. Iversen, "Avoided crossing of rattler modes in thermoelectric materials," *Nature materials*, vol. 7, no. 10, pp. 811–815, 2008.

[26] J. Dong, O. F. Sankey, and C. W. Myles, "Theoretical study of the lattice thermal conductivity in Ge framework semiconductors," *Physical review letters*, vol. 86, no. 11, pp. 2361(1)–(5), 2001.

[27] R. P. Hermann, F. Grandjean, and G. J. Long, "Einstein oscillators that impede thermal transport," *American journal of physics*, vol. 73, no. 2, pp. 110–118, 2005.

[28] J. H. Roudebush, E. S. Toberer, H. Hope, G. Jeffrey Snyder, and S. M. Kauzlarich, "Crystal structure, characterization and thermoelectric properties of the type-I clathrate $\mathrm{Ba_{8-y}Sr_yAl_14Si_{32}}$ $(0.6 \leqslant \mathrm{y} \leqslant 1.3)$ prepared by aluminum flux," *Journal of Solid State Chemistry*, vol. 184, no. 5, pp. 1176–1185, 2011.

[29] K. Suekuni, M. Avila, K. Umeo, and T. Takabatake, "Cage-size control of guest vibration and thermal conductivity in $\mathrm{Sr_8Ga_{16}Si_{30-x}Ge_x}$," *Physical Review B*, vol. 75, no. 19, pp. 195210(1)–(6), 2007.

[30] Shimizu, Hiroyasu, Imai, Takahiko and Kume, Tetsuji and Sasaki, Shigeo and Kaltzoglou, Andreas and Fässler, F. Thomas, "Raman spectroscopy study of type-I clathrates $A_8Sn_{44}\square_2$ (A= Rb, Cs) and $Rb_8Hg_4Sn_{42}$", *journal Chemical Physics Letters*, volume 464, number 1-3, pages 54–57, year 2008.

[31] N. de Koker, "Thermal conductivity of mgo periclase from equilibrium first principles molecular dynamics," *Physical review letters*, vol. 103, no. 12, p. 125902, 2009.

[32] G. Pizzi, D. Volja, B. Kozinsky, M. Fornari, and N. Marzari, "Boltzwann: A code for the evaluation of thermoelectric and electronic transport properties with a maximally-localized wannier functions basis," *Computer Physics Communications*, vol. 185, no. 1, pp. 422–429, 2014.

[33] M. Beekman and G. Nolas, "Inorganic clathrate-ii materials of group 14: synthetic routes and physical properties," *Journal of Materials Chemistry*, vol. 18, no. 8, pp. 842–851, 2008.

[34] K. A. Kovnir and A. V. Shevelkov, "Semiconducting clathrates: synthesis, structure and properties," *Russian chemical reviews*, vol. 73, no. 9, p. 923, 2004.

[35] J. S. Kasper, P. Hagenmuller, M. Pouchard, and C. Cros, "Clathrate structure of silicon Na_8Si_{46} and Na_xSi_{136} ($x \leq 11$)," *Science*, vol. 150, no. 3704, pp. 1713–1714, 1965.

[36] E. Reny, P. Gravereau, C. Cros, and M. Pouchard, "Structural characterisations of the Na_xSi_{136} and Na_8Si_{46} silicon clathrates using the rietveld method," *Journal of Materials Chemistry*, vol. 8, no. 12, pp. 2839–2844, 1998.

[37] H.-o. Horie, T. Kikudome, K. Teramura, and S. Yamanaka, "Controlled thermal decomposition of nasi to derive silicon clathrate compounds," *Journal of Solid State Chemistry*, vol. 182, no. 1, pp. 129–135, 2009.

[38] M. Baitinger, B. Böhme, A. Ormeci, and Y. Grin, "Solid state chemistry of clathrate phases: crystal structure, chemical bonding and preparation routes," in *The Physics and Chemistry of Inorganic Clathrates*, pp. 35–64, Springer, 2014.

[39] J. Gallmeier, H. Schäfer, and A. Weiss, "Notizen: Eine käfigstruktur als gemeinsames bauprinzip der verbindungen K_8E_{46} (E = Si, Ge, Sn)," *Zeitschrift für Naturforschung B*, vol. 24, no. 6, pp. 665–671, 1969.

[40] H.-G. von Schnering, "Zintl-phasen: prinzipien von struktur und bindung," *Nova Acta Leopoldina Halle*, vol. 59, pp. 168–182, 1985.

[41] Y. N. Grin, L. Melekhov, K. Chuntonov, and S. Yatsenko, "Crystal structure of Cs_8Sn_{46}," *Kristallografiya*, vol. 32, no. 2, pp. 497–498, 1987.

[42] T. Iwamoto, "Past, present and future of the clathrate inclusion compounds built of cyanometallate hosts," *Journal of inclusion phenomena and molecular recognition in chemistry*, vol. 24, no. 1-2, pp. 61–132, 1996.

[43] A. Müller, H. Reuter, and S. Dillinger, "Supramolecular inorganic chemistry: small guests in small and large hosts," *Angewandte Chemie International Edition in English*, vol. 34, no. 21, pp. 2328–2361, 1995.

[44] S. M. Kauzlarich, S. R. Brown, and G. J. Snyder, "Zintl phases for thermoelectric devices," *Dalton Transactions*, no. 21, pp. 2099–2107, 2007.

[45] T. Harman, "Special techniques for measurement of thermoelectric properties," *Journal of Applied Physics*, vol. 29, no. 9, pp. 1373–1374, 1958.

[46] J. Straehle, S. Rath, T. Hans, T. Metzger, T. Nissel, R. Huebener, and S. Kemmler-Sack, "Prospects for peltier cooling of the cuprate superconductors," in *Thermoelectrics, 1998. Proceedings ICT 98. XVII International Conference on*, pp. 491–494, IEEE, 1998.

[47] G. Nolas, G. Slack, D. Morelli, T. Tritt, and A. Ehrlich, "The effect of rare-earth filling on the lattice thermal conductivity of skutterudites," *Journal of Applied Physics*, vol. 79, no. 8, pp. 4002–4008, 1996.

[48] B. Sales, B. Chakoumakos, D. Mandrus, and J. Sharp, "Atomic displacement parameters and the lattice thermal conductivity of clathrate-like thermoelectric compounds," *Journal of Solid State Chemistry*, vol. 146, no. 2, pp. 528–532, 1999.

[49] D. T. Morelli, G. P. Meisner, B. Chen, S. Hu, and C. Uher, "Cerium filling and doping of cobalt triantimonide," *Physical Review B*, vol. 56, no. 12, p. 7376, 1997.

[50] B. Sales, D. Mandrus, B. Chakoumakos, V. Keppens, and J. Thompson, "Filled skutterudite antimonides: Electron crystals and phonon glasses," *Physical Review B*, vol. 56, no. 23, p. 15081, 1997.

[51] J. S. Tse, C. I. Ratcliffe, B. M. Powell, V. F. Sears, and Y. P. Handa, "Rotational and translational motions of trapped methane. incoherent inelastic neutron scattering of methane hydrate," *The Journal of Physical Chemistry A*, vol. 101, no. 25, pp. 4491–4495, 1997.

[52] E. Shoko, V. K. Peterson, and G. J. Kearley, "Toward a mechanism of rattler coupling in the β-pyrochlores AOS_2O_6(A= K, Rb, Cs)," *Journal of materials science*, vol. 49, no. 15, pp. 5468–5480, 2014.

[53] S. Christensen, L. Bjerg, A. Kaltzoglou, and M. Juranyi, Fanni, "Guest host interaction and low energy host structure dynamics in tin clathrates," *Journal of Applied Physics*, vol. 113, no. 8, pp. 084902(1)–(8), 2013.

[54] G. A. Slack, "Design concepts for improved thermoelectric materials," in *MRS Proceedings*, vol. 478, p. 47, Cambridge Univ Press, 1997.

[55] J. Tse, Z. Li, and K. Uehara, "Phonon band structures and resonant scattering in na8si46 and cs8sn44 clathrates," *EPL (Europhysics Letters)*, vol. 56, no. 2, p. 261, 2001.

[56] N. Blake, S. Latturner, J. Bryan, *et al.*, "Band structures and thermoelectric properties of the clathrates $Ba_8Ga_{16}Ge_{30}$, $Sr_8Ga_{16}Ge_{30}$, $Ba_8Ga_{16}Si_{30}$, and $Ba_8In_{16}Sn_{30}$ (vol 115, pg 8060, 2001)," *Journal of Chemical Physics*, vol. 116, no. 21, pp. 9545–9547, 2002.

[57] Wikipedia, "Zintl phase — wikipedia, the free encyclopedia," 2014. [Online; accessed 17-April-2015].

[58] A. J. Jacobson and L. F. Nazar, "Intercalation chemistry," *Encyclopedia of Inorganic and Bioinorganic Chemistry*, 2011.

[59] G. Kavei, "Weight of seebeck coefficient and thermal conductivity on thermoelectric pellets, a review,"

[60] H. VONSCHNERING, "Zintl phases-principles of structure and bonding," *BOLETIN DE LA SOCIEDAD CHILENA DE QUIMICA*, vol. 33, no. 1, pp. 41–57, 1988.

[61] J. Emsley, "The elements, clarendon," *Oxford*, vol. 52, no. 96, p. 210, 1989.

[62] F. R. Wagner, V. Bezugly, M. Kohout, and Y. Grin, "Charge decomposition analysis of the electron localizability indicator: a bridge between the orbital and direct space representation of the chemical bond," *Chemistry-A European Journal*, vol. 13, no. 20, pp. 5724–5741, 2007.

[63] R. F. Bader, *Atoms in molecules*. Wiley Online Library, 1990.

[64] Y. Saiga, B. Du, S. Deng, K. Kajisa, and T. Takabatake, "Thermoelectric properties of type-VIII clathrate $Ba_8Ga_{16}Sn_{30}$ doped with Cu," *Journal of Alloys and Compounds*, vol. 537, pp. 303–307, 2012.

[65] A. Saramat, G. Svensson, A. Palmqvist, C. Stiewe, E. Müller, D. Platzek, S. Williams, D. Rowe, J. Bryan, and G. Stucky, "Large thermoelectric figure of merit at high temperature in czochralski-grown clathrate $ba_8ga_{16}ge_{30}$," *Journal of Applied Physics*, vol. 99, no. 2, p. 023708, 2006.

[66] Y. Kono, N. Ohya, T. Taguchi, K. Suekuni, T. Takabatake, S. Yamamoto, and K. Akai, "First-principles study of type-I and type-VIII $Ba_8Ga_{16}Sn_{30}$ clathrates," *Journal of Applied Physics*, vol. 107, no. 12, p. 123720, 2010.

[67] L. Møllnitz, N. P. Blake, and H. Metiu, "Effects of morphology on the electronic and transport properties of sn-based clathrates," *The Journal of Chemical Physics*, vol. 117, no. 3, pp. 1302–1312, 2002.

[68] X. Yan, E. Bauer, P. Rogl, and S. Paschen, "Structural and thermoelectric properties of $ba_8cu_5si_xge_{4(1-x)}$ clathrates," *Physical Review B*, vol. 87, no. 11, p. 115206, 2013.

[69] X. Tang, P. Li, S. Deng, and Q. Zhang, "High temperature thermoelectric transport properties of double-atom-filled clathrate compounds $Yb_xBa_{8-x}Ga_{16}Ge_{30}$," *Journal of Applied Physics*, vol. 104, no. 1, p. 013706, 2008.

[70] N. L. Okamoto, K. Kishida, K. Tanaka, and H. Inui, "Effect of in additions on the thermoelectric properties of the type-i clathrate compound $ba_8ga_{16}ge_{30}$," *Journal of applied physics*, vol. 101, no. 11, p. 113525, 2007.

[71] X. Shi, J. Yang, S. Bai, J. Yang, H. Wang, M. Chi, J. R. Salvador, W. Zhang, L. Chen, and W. Wong-Ng, "On the design of high-efficiency thermoelectric clathrates through a systematic cross-substitution of framework elements," *Advanced Functional Materials*, vol. 20, no. 5, pp. 755–763, 2010.

[72] M. Falmbigl, A. Grytsiv, P. Rogl, P. Heinrich, E. Royanian, and E. Bauer, "Tuning of band gap and thermoelectric properties of type-i clathrate $Ba_8Ni_xZn_yGe_{46-x-y-z}Sn_z$," *Journal of Alloys and Compounds*, vol. 567, pp. 65–72, 2013.

[73] X. Hou, Y. Zhou, L. Wang, W. Zhang, W. Zhang, and L. Chen, "Growth and thermoelectric properties of $Ba_8Ga_{16}Ge_{30}$ clathrate crystals," *Journal of Alloys and Compounds*, vol. 482, no. 1, pp. 544–547, 2009.

[74] M. Falmbigl, A. Grytsiv, P. Rogl, X. Yan, E. Royanian, and E. Bauer, "Influence of sn-substitution on the thermoelectric properties of the clathrate type-i, $ba_8zn_xge_{46-x-y-z}sn_y$," *Dalton Transactions*, vol. 42, no. 8, pp. 2913–2920, 2013.

[75] W.-Q. Cao, Y.-G. Yan, X.-F. Tang, and S.-K. Deng, "The effects of in isoelectronic substitution for ga on the thermoelectric properties of $Sr_8Ga_{16-x}In_xGe_{30}$ type-I clathrates," *Journal of Physics D: Applied Physics*, vol. 41, no. 21, p. 215105, 2008.

[76] S. Deng, X. Tang, P. Li, and Q. Zhang, "High temperature thermoelectric transport properties of p-type $Ba_8Ga_{16}Al_{30}Ge_{30-x}$ type-I clathrates with high performance," *Journal of Applied Physics*, vol. 103, no. 7, p. 073503, 2008.

[77] J. Xu, J. Wu, H. Shao, S. Heguri, Y. Tanabe, Y. Liu, G.-Q. Liu, J. Jiang, H. Jiang, and K. Tanigaki, "Structure and thermoelectric properties of the n-type clathrate $Ba_8Cu_{5.1}Ge_{40.2}Sn_{0.7}$," *Journal of Materials Chemistry A*, vol. 3, no. 37, pp. 19100–19106, 2015.

[78] S.-k. Jeung, "Optimization of type-i clathrates for thermoelectric properties," Master's thesis, University of Waterloo, 2012.

[79] V. Kuznetsov, L. Kuznetsova, A. Kaliazin, and D. Rowe, "Preparation and thermoelectric properties of $A_8^{II}B_{16}^{III}B_{30}^{IV}$ clathrate compounds," *Journal of Applied Physics*, vol. 87, no. 11, pp. 7871–7875, 2000.

[80] A. V. Shevelkov, "Thermoelectric power generation by clathrates," in *Thermoelectrics for Power Generation-A Look at Trends in the Technology*, InTech, 2016.

[81] P. Vinet, J. H. Rose, J. Ferrante, and J. R. Smith, "Universal features of the equation of state of solids," *Journal of Physics: Condensed Matter*, vol. 1, no. 11, p. 1941, 1989.

[82] P. Vinet, J. R. Smith, J. Ferrante, and J. H. Rose, "Temperature effects on the universal equation of state of solids," *Physical Review B*, vol. 35, no. 4, p. 1945, 1987.

[83] A. F. Guillermet, V. Ozoliņš, G. Grimvall, and M. Körling, "Phase stabilities in the pt-w system: Thermodynamic and electronic-structure calculations," *Physical Review B*, vol. 51, no. 16, p. 10364, 1995.

[84] P. O. Egbele, E. Shoko, and D. P. Joubert, "Structural and thermoelectric properties of the type-I Sn clathrates $Cs_8Sn_{(46-n)}$ (n= 0, 2) from density functional theory (DFT)," *MRS Advances*, pp. 1–7, 2018.

[85] A. Kaltzoglou, S. D. Hoffmann, and T. F. Fässler, "Order-disorder phase transition in type-I clathrate $Cs_8Sn_{44}\square_2$," *European Journal of Inorganic Chemistry*, vol. 2007, no. 26, pp. 4162–4167, 2007.

[86] C. W. Myles, J. Dong, and O. F. Sankey, "Structural and electronic properties of tin clathrate materials," *Physical Review B*, vol. 64, no. 16, p. 165202, 2001.

[87] J.-A. Dolyniuk, B. Owens-Baird, J. Wang, J. V. Zaikina, and K. Kovnir, "Clathrate thermoelectrics," *Materials Science and Engineering: R: Reports*, vol. 108, pp. 1–46, 2016.

[88] M. S. Suleiman, M. P. Molepo, and D. P. Joubert, "A theoretical investigation of structural, electronic and optical properties of bulk copper nitrides," *arXiv preprint arXiv:1211.0179*, 2012.

[89] K. Leung, S. B. Rempe, and O. A. von Lilienfeld, "Ab initio molecular dynamics calculations of ion hydration free energies," *The Journal of chemical physics*, vol. 130, no. 20, p. 204507, 2009.

[90] J. M. Haile, *Molecular dynamics simulation: elementary methods*. John Wiley & Sons, Inc., 1992.

[91] W. Kohn, "W. kohn and lj sham, phys. rev. 140, a1133 (1965).," *phys. Rev.*, vol. 140, p. A1133, 1965.

[92] P. E. Blöchl, "Projector augmented-wave method," *Physical Review B*, vol. 50, no. 24, p. 17953, 1994.

[93] G. Kresse and D. Joubert, "From ultrasoft pseudopotentials to the projector augmented-wave method," *Physical Review B*, vol. 59, no. 3, p. 1758, 1999.

[94] Y. Zhou and G. H. Miller, "Green- kubo formulas for mutual diffusion coefficients in multicomponent systems," *The Journal of Physical Chemistry*, vol. 100, no. 13, pp. 5516–5524, 1996.

[95] K. Hess, "Boltzmann transport equation," in *The Physics of Submicron Semiconductor Devices*, pp. 33–43, Springer, 1988.

[96] A. Togo, F. Oba, and I. Tanaka, "First-principles calculations of the ferroelastic transition between rutile-type and CaCl 2-type Si$O_2 at high pressures," Physical Review B, vol. 78, no. 13, p. 134106, 2008.$

[97] W. Li, L. Lindsay, D. Broido, D. A. Stewart, and N. Mingo, "Thermal conductivity of bulk and nanowire $Mg_2Si_xSn_{1-x}$ alloys from first principles," *Physical Review B*, vol. 86, no. 17, p. 174307, 2012.

[98] S. Wang, Z. Wang, W. Setyawan, N. Mingo, and S. Curtarolo, "Assessing the thermoelectric properties of sintered compounds via high-throughput ab-initio calculations," *Physical Review X*, vol. 1, no. 2, p. 021012, 2011.

[99] G. J. Snyder and E. S. Toberer, "Complex thermoelectric materials," *Nature materials*, vol. 7, no. 2, pp. 105–114, 2008.

[100] J. T. Devreese and P. Van Camp, *Electronic Structure, dynamics, and quantum structural properties of condensed matter*, vol. 121. Springer Science & Business Media, 2013.

[101] K. Kunc and R. M. Martin, "Ab initio force constants of gaas: A new approach to calculation of phonons and dielectric properties," *Physical Review Letters*, vol. 48, no. 6, p. 406, 1982.

[102] A. A. Mostofi, J. R. Yates, Y.-S. Lee, I. Souza, D. Vanderbilt, and N. Marzari, "wannier90: A tool for obtaining maximally-localised wannier functions," *Computer physics communications*, vol. 178, no. 9, pp. 685–699, 2008.

[103] G. Ackland, M. Warren, and S. Clark, "Practical methods in ab initio lattice dynamics," *Journal of Physics: Condensed Matter*, vol. 9, no. 37, p. 7861, 1997.

[104] L. E. Bell, "Cooling, heating, generating power, and recovering waste heat with thermoelectric systems," *Science*, vol. 321, no. 5895, pp. 1457–1461, 2008.

[105] A. Ward and D. Broido, "Intrinsic phonon relaxation times from first-principles studies of the thermal conductivities of si and ge," *Physical Review B*, vol. 81, no. 8, p. 085205, 2010.

[106] Y. Pei, H. Wang, and G. J. Snyder, "Band engineering of thermoelectric materials," *Advanced materials*, vol. 24, no. 46, pp. 6125–6135, 2012.

[107] R. M. Martin, *Electronic structure: basic theory and practical methods*. Cambridge university press, 2004.

[108] R. Armiento, *The many-Electron energy in density functional theory*. PhD thesis, Ph. D. Thesis, KTH School of Engineering Sciences, Stockholm, Sweden. (consultada: 19 de Mayo de 2011), 2005.

[109] A. D. Becke and E. R. Johnson, "A simple effeective potential for exchange," 2006.

[110] F. Tran and P. Blaha, "Accurate band gaps of semiconductors and insulators with a semilocal exchange-correlation potential," *Physical review letters*, vol. 102, no. 22, p. 226401, 2009.

[111] W. A. Harrison, *Electronic structure and the properties of solids: the physics of the chemical bond*. Courier Corporation, 2012.

[112] J. M. Ziman, "Electrons in metals: A short guide to the fermi surface," *Contemporary Physics*, vol. 4, no. 2, pp. 81–99, 1962.

[113] G. Kresse and J. Furthmuller, "Vasp the guide," *Computational Physics, Faculty of Physics, Universit*^{2}*at Wien, Sensengasse*, vol. 8, 2001.

[114] W. Kohn and L. J. Sham, "Self-consistent equations including exchange and correlation effects," *Physical review*, vol. 140, no. 4A, p. A1133, 1965.

[115] J. P. Perdew, K. Burke, and M. Ernzerhof, "Generalized gradient approximation made simple," *Physical review letters*, vol. 77, no. 18, p. 3865, 1996.

[116] M. De La Pierre, R. Orlando, L. Maschio, K. Doll, P. Ugliengo, and R. Dovesi, "Performance of six functionals (lda, pbe, pbesol, b3lyp, pbe0, and wc1lyp) in the simulation of vibrational and dielectric properties of crystalline compounds. the case of forsterite mg2sio4," *Journal of computational chemistry*, vol. 32, no. 9, pp. 1775–1784, 2011.

[117] M. Dion, H. Rydberg, E. Schröder, D. C. Langreth, and B. I. Lundqvist, "Van der waals density functional for general geometries," *Phys. Rev. Lett.*, vol. 92, p. 246401, Jun 2004.

[118] J. P. Perdew, "Density-functional approximation for the correlation energy of the inhomogeneous electron gas," *Physical Review B*, vol. 33, no. 12, p. 8822, 1986.

[119] J. P. Perdew, A. Ruzsinszky, G. I. Csonka, O. A. Vydrov, G. E. Scuseria, L. A. Constantin, X. Zhou, and K. Burke, "Restoring the density-gradient expansion for exchange in solids and surfaces," *Physical Review Letters*, vol. 100, no. 13, p. 136406, 2008.

[120] P. Hohenberg, "P. hohenberg and w. kohn, phys. rev. 136, b864 (1964).," *Phys. Rev.*, vol. 136, p. B864, 1964.

[121] R. O. Jones and O. Gunnarson, "The density functional formalism, its applications and prospects," *Reviews of Modern Physics*, vol. 61, no. 3, p. 689, 1989.

[122] B. Alder and D. Ceperly, "ground state of the electron gas by a stochastic method," *Physical Review Letters*, vol. 45, no. 7, p. 56, 1980.

[123] E. Kaxiras, *Atomic and electronic structure of solids*. Cambridge University Press, 2003.

[124] J. Calloway and G. G. Johnson, "Energy band theory," *Physics Today*, vol. 17, p. 61, 1964.

[125] M. Suzuki, T. Uenoyama, and A. Yanase, "First-principles calculations of effective-mass parameters of aln and gan," *Physical Review B*, vol. 52, no. 11, p. 8132, 1995.

[126] P. Drude, "Zur elektronentheorie der metalle," *Annalen der Physik*, vol. 306, no. 3, pp. 566–613, 1900.

[127] R. Godby and R. Needs, "Metal-insulator transition in kohn-sham theory and quasiparticle theory," *Physical review letters*, vol. 62, no. 10, p. 1169, 1989.

[128] B. Khan, H. R. Aliabad, N. Razghandi, M. Maqbool, S. J. Asadabadi, and I. Ahmad, "Structural and thermoelectric properties of pure and la, y doped homno 3 for their use as alternative energy materials," *Computer Physics Communications*, vol. 187, pp. 1–7, 2015.

[129] G. K. Madsen, "Automated search for new thermoelectric materials: the case of liznsb," *Journal of the American Chemical Society*, vol. 128, no. 37, pp. 12140–12146, 2006.

[130] S. Ambrosch-Draxl, C. Thonhauser, T. Badding, and J. Sofo, "Transport coefficients from first-principles calculation," *Phys. Rev. B*, vol. 68, pp. 125210–1, 2003.

[131] T. Róg, K. Murzyn, K. Hinsen, and G. R. Kneller, "nmoldyn: a program package for a neutron scattering oriented analysis of molecular dynamics simulations," *Journal of computational chemistry*, vol. 24, no. 5, pp. 657–667, 2003.

[132] M. P. Allen and D. J. Tildesley, *Computer simulation of liquids*. Oxford university press, 1989.

[133] A. Kaltzoglou, T. Fässler, M. Christensen, S. Johnsen, B. Iversen, I. Presniakov, A. Sobolev, and A. Shevelkov, "Effects of the order–disorder phase transition on the physical properties of A_8Sn_{40} ($A = Rb, Cs$)," *Journal of Materials Chemistry*, vol. 18, no. 46, pp. 5630–5637, 2008.

[134] J.-T. and J. D. Corbett, "Zintl phases in alkali-metal-tin systems: K8sn25 with condensed pentagonal dodecahedra of tin. two A_8Sn_{44} phases with a defect clathrate structure," *Inorganic Chemistry*, vol. 33, no. 25, pp. 5721–5726, 1994.

[135] H. von Schnering, "R kroener, m baitinger, k peters, r nesper, yu grin," *Z. Kristalogr.-New Cryst. Struct*, vol. 215, p. 205, 2000.

[136] J. Gallmeier, H. Schäfer, and A. Weiss, "Cage structure as a common building principle of compounds k 8 e 46 (e= si, ge, sn)," *Z. Naturforsch. B*, vol. 24, no. 6, pp. 665–667, 1969.

[137] J. C. Grossman, L. Mitas, and K. Raghavachari, "Structure and stability of molecular carbon: importance of electron correlation," *Physical review letters*, vol. 75, no. 21, p. 3870, 1995.

[138] A. Zupan, P. Blaha, K. Schwarz, and J. P. Perdew, "Pressure-induced phase transitions in solid Si, SiO_2, andFe: Performance of local-spin-density and generalized-gradient-approximation density functionals," *Physical Review B*, vol. 58, no. 17, p. 11266, 1998.

[139] S. Bobev and S. C. Sevov, "Clathrates of group 14 with alkali metals: an exploration," *Journal of Solid State Chemistry*, vol. 153, no. 1, pp. 92–105, 2000.

[140] G. Kresse, J. Furthmüller, and J. Hafner, "Ab initio force constant approach to phonon dispersion relations of diamond and graphite," *EPL (Europhysics Letters)*, vol. 32, no. 9, p. 729, 1995.

[141] G. Kresse and J. Furthmüller, "Efficient iterative schemes for ab initio total-energy calculations using a plane-wave basis set," *Physical review B*, vol. 54, no. 16, p. 11169, 1996.

[142] Y. Guyot, B. Champagnon, E. Reny, C. Cros, M. Pouchard, P. Melinon, A. Perez, and I. Gregora, "Raman scattering of silicon clathrates," *Physical Review B*, vol. 57, no. 16, p. R9475, 1998.

[143] A. Demkov, O. Sankey, S. Daftuar, and J. Gryko, "The physics of semiconductors," *Edited by: David, J. Lokwood*, vol. 3, p. 2205, 1994.

[144] G. S. Nolas, B. C. Chakoumakos, B. Mahieu, G. J. Long, and T. Weakley, "Structural characterization and thermal conductivity of type-i tin clathrates," *Chemistry of materials*, vol. 12, no. 7, pp. 1947–1953, 2000.

[145] J. Yang, G. P. Meisner, C. J. Rawn, H. Wang, B. C. Chakoumakos, J. Martin, G. S. Nolas, B. L. Pedersen, and J. K. Stalick, "Low temperature transport and structural properties of misch-metal-filled skutterudites," *Journal of Applied Physics*, vol. 102, p. 083702, oct 2007.

[146] J. Yang, W. Zhang, S. Q. Bai, Z. Mei, and L. D. Chen, "Dual-frequency resonant phonon scattering in $Ba_xR_yCo_4Sb_{12}$ ($R = La, Ce, and Sr$)," *Applied Physics Letters*, vol. 90, p. 192111, may 2007.

[147] D. R. Clarke, "Materials selection guidelines for low thermal conductivity thermal barrier coatings," *Surface and Coatings Technology*, vol. 163, pp. 67–74, 2003.

[148] L.-D. Zhao, S.-H. Lo, Y. Zhang, H. Sun, G. Tan, C. Uher, C. Wolverton, V. P. Dravid, and M. G. Kanatzidis, "Ultralow thermal conductivity and high thermoelectric figure of merit in SnSe crystals," *Nature*, vol. 508, no. 7496, p. 373, 2014.

[149] C.-w. Zhang and S.-s. Yan, "First-principles study of ferromagnetism in two-dimensional silicene with hydrogenation," *The Journal of Physical Chemistry C*, vol. 116, no. 6, pp. 4163–4166, 2012.

[150] D. Morelli, V. Jovovic, and J. Heremans, "Intrinsically minimal thermal conductivity in cubic $I-V-VI_2$ semiconductors," *Physical review letters*, vol. 101, no. 3, p. 035901, 2008.

[151] M. D. Nielsen, V. Ozolins, and J. P. Heremans, "Lone pair electrons minimize lattice thermal conductivity," *Energy & Environmental Science*, vol. 6, no. 2, pp. 570–578, 2013.

[152] D. S. Parker, A. F. May, and D. J. Singh, "Benefits of carrier-pocket anisotropy to thermoelectric performance: The case of p-type agbise 2," *Physical Review Applied*, vol. 3, no. 6, p. 064003, 2015.

[153] Z. Aksamija and I. Knezevic, "Lattice thermal conductivity of graphene nanoribbons: Anisotropy and edge roughness scattering," *Applied Physics Letters*, vol. 98, no. 14, p. 141919, 2011.

[154] S. G. Louie and M. L. Cohen, "Electronic structure of a metal-semiconductor interface," *Physical Review B*, vol. 13, no. 6, p. 2461, 1976.

[155] X. Shi and J. Sun, "Dependence of seebeck coefficient on the density of states in organic semiconductors," *IEEE Electron Device Letters*, vol. 38, no. 12, pp. 1728–1731, 2017.

[156] N. P. Blake, S. Latturner, J. D. Bryan, G. D. Stucky, and H. Metiu, "Band structures and thermoelectric properties of the clathrates $Ba_8Ga_{16}Ge_{30}$, $Sr_8Ga_{16}Ge_{30}$, $Ba_8Ga_{16}Si_{30}$, and $Ba_8In_{16}Sn_{30}$," *The Journal of Chemical Physics*, vol. 115, no. 17, pp. 8060–8073, 2001.

[157] B. Ryu and M.-W. Oh, "Computational simulations of thermoelectric transport properties," *Journal of the Korean Ceramic Society*, vol. 53, no. 3, pp. 273–281, 2016.

[158] Y. Takasu, T. Hasegawa, N. Ogita, M. Udagawa, M. Avila, K. Suekuni, and T. Takabatake, "Off-center rattling and anisotropic expansion of type-i clathrates studied by raman scattering," *Physical review letters*, vol. 100, no. 16, p. 165503, 2008.

[159] S. Stefanoski, J. Martin, and G. S. Nolas, "Low temperature transport properties and heat capacity of single-crystal Na_8Si_{46}, " *Journal of Physics: Condensed Matter*, volume 22, number 48, pages 485404, year 2010.

[160] A. Ioffe, "Semiconductor thermoelements and thermoelectric refrigeration," *Infosearch, London*, p. 39, 1957.

[161] G. H. Fecher, E. Rausch, B. Balke, A. Weidenkaff, and C. Felser, "Half-heusler materials as model systems for phase-separated thermoelectrics," *physica status solidi (a)*, vol. 213, no. 3, pp. 716–731, 2016.

[162] A. Jayaraman, A. Bhat Kademane, and M. Molli, "Dft study on the carrier concentration and temperature-dependent thermoelectric properties of antimony selenide," *Indian Journal of Materials Science*, vol. 2016, 2016.

[163] G. Busch, C. Fröhlich, F. Hulliger, and E. Steigmeier, "Struktur, elektrische und thermoelektrische eigenschaften von $SnSe_2$," *Helv. Phys. Acta*, vol. 34, no. 4, pp. 359–368, 1961.

[164] Z. Chen and C. Dames, "An anisotropic model for the minimum thermal conductivity," *Applied Physics Letters*, vol. 107, no. 19, p. 193104, 2015.

[165] Y. Ding, B. Xiao, G. Tang, and J. Hong, "Transport properties and high thermopower of snse2: A full ab-initio investigation," *The Journal of Physical Chemistry C*, 2016.

[166] S. T. John, S. Desgreniers, M. R. Ferguson, and Y. Kawazoe, "Structural stability and phase transitions in K_8Si_{46} clathrate under high pressure," *Physical review letters*, vol. 89, no. 19, pp. 195507(1)–4, 2002.

[167] A. D. Becke, "Density-functional exchange-energy approximation with correct asymtotic behaviour," *Physical review A*, vol. 38, no. 6, p. 3098, 1988.

[168] J. Thijssen, *Computational physics*. Cambridge University Press, 2007.

[169] P. Murdin, "Pauli exclusion principle," *Encyclopedia of Astronomy and Astrophysics*, vol. 1, p. 4896, 2000.

[170] P. Dirac, "Note on exchange phenomena in the thomas atom," in *Proceedings of the Cambridge Philosophical Society*, vol. 26, p. 376, 1930.

[171] U. von Barth and L. Hedin, "A local exchange-correlation potential for the spin polarized case," *Journal of Physics C: Solid State Physics*, vol. 5, no. 13, p. 1629, 1972.

[172] D. Ceperley and B. Alder, "Ground state of the electron gas by a stochastic method," *Physical Review Letters*, vol. 45, no. 7, pp. 566–569, 1980.

[173] J. Kohanoff, *Electronic structure calculations for solids and molecules: theory and computational methods*. Cambridge University Press, 2006.

[174] S. Vosko and L. Wilk, "Influence of an improved local-spin-density correlation-energy functional on the cohesive energy of alkali metals," *Physical Review B*, vol. 22, no. 8, p. 3812, 1980.

[175] J. Perdew, "Electronic structure of solids 91, edited by *Ziesche, P. and Eschrig, H.*(berlin: Akademie-verlag) p. 11;*Perdew, JP and Wang, Y.*, 1992," *Phys. Rev. B*, vol. 45, no. 13, p. 244, 1991.

[176] Y. Zhang, W. Pan, and W. Yang, "Describing van der waals interaction in diatomic molecules with generalized gradient approximations: The role of the exchange functional," *The Journal of chemical physics*, vol. 107, no. 19, pp. 7921–7925, 1997.

[177] D. C. Patton and M. R. Pederson, "Application of the generalized-gradient approximation to rare-gas dimers," *Physical Review A*, vol. 56, no. 4, p. R2495, 1997.

[178] D. C. Patton, D. V. Porezag, and M. R. Pederson, "Simplified generalized-gradient approximation and anharmonicity: Benchmark calculations on molecules," *Physical Review B*, vol. 55, no. 12, p. 7454, 1997.

[179] P. Bagno, O. Jepsen, and O. Gunnarsson, "Ground-state properties of third-row elements with nonlocal density functionals," *Physical Review B*, vol. 40, no. 3, p. 1997, 1989.

[180] M. Levy, "Density-functional exchange correlation through coordinate scaling in adiabatic connection and correlation hole," *Physical Review A*, vol. 43, no. 9, p. 4637, 1991.

[181] D. Hamann, "Generalized gradient theory for silica phase transitions," *Physical Review Letters*, vol. 76, no. 4, p. 660, 1996.

[182] I. Boustani and A. Quandt, "Nanotubules of bare boron clusters: Ab initio and density functional study," *EPL (Europhysics Letters)*, vol. 39, no. 5, p. 527, 1997.

[183] K. Albe and W. Möller, "Modelling of boron nitride: Atomic scale simulations on thin film growth," *Computational Materials Science*, vol. 10, no. 1, pp. 111–115, 1998.

[184] M. Z. Bazant, E. Kaxiras, and J. F. Justo, "Environment-dependent interatomic potential for bulk silicon," *Physical Review B*, vol. 56, no. 14, p. 8542, 1997.

[185] T. Ziegler, V. Tschinke, and A. Becke, "A theoretical study on the strength of multiple metal-metal bonds in binuclear complexes and transition-metal dimers by a non-local density functional method," *Polyhedron*, vol. 6, no. 4, pp. 685–693, 1987.

[186] T. Ziegler, "Approximate density functional theory as a practical tool in molecular energetics and dynamics," *Chemical Reviews*, vol. 91, no. 5, pp. 651–667, 1991.

[187] J. Hafner, "Ab-initio simulations of materials using vasp: Density-functional theory and beyond," *Journal of computational chemistry*, vol. 29, no. 13, pp. 2044–2078, 2008.

[188] M. P. Molepo, *Computational study of the structural phase transitions and pressure dependent electronic structure of ZnO*. PhD thesis, University of the Witwatersrand, 2012.

[189] J. Paier, M. Marsman, K. Hummer, G. Kresse, I. C. Gerber, and J. G. Ángyán, "Screened hybrid density functionals applied to solids," *The Journal of chemical physics*, vol. 124, p. 154709, 2006.

[190] S. Park, B. Lee, S. H. Jeon, and S. Han, "Hybrid functional study on structural and electronic properties of oxides," *Current Applied Physics*, vol. 11, no. 3, pp. S337–S340, 2011.

[191] M. Dion, H. Rydberg, E. Schröder, D. C. Langreth, and B. I. Lundqvist, "Van der Waals density functional for general geometries," *Physical review letters*, vol. 92, no. 24, p. 246401, 2004.

[192] G. Román-Pérez and J. M. Soler, "Efficient implementation of a van der Waals density functional: application to double-wall carbon nanotubes," *Physical review letters*, vol. 103, no. 9, p. 096102, 2009.

[193] S. Grimme, J. Antony, S. Ehrlich, and H. Krieg, "A consistent and accurate *ab initio* parametrization of density functional dispersion correction (DFT-D) for the 94 elements H-Pu," *The Journal of chemical physics*, vol. 132, no. 15, p. 154104, 2010.

[194] S. Grimme, "Semiempirical GGA-type density functional constructed with a long-range dispersion correction," *Journal of computational chemistry*, vol. 27, no. 15, pp. 1787–1799, 2006.

[195] H. Rydberg, M. Dion, N. Jacobson, E. Schröder, P. Hyldgaard, S. Simak, D. C. Langreth, and B. I. Lundqvist, "Van der waals density functional for layered structures," *Physical review letters*, vol. 91, no. 12, p. 126402, 2003.

[196] U. Zimmerli, M. Parrinello, and P. Koumoutsakos, "Dispersion corrections to density functionals for water aromatic interactions," *The Journal of chemical physics*, vol. 120, p. 2693, 2004.

[197] K. Lee, É. D. Murray, L. Kong, B. I. Lundqvist, and D. C. Langreth, "Higher-accuracy van der waals density functional," *Physical Review B*, vol. 82, no. 8, p. 081101, 2010.

[198] T.-H. Wang and T. Searle, "A rigid band model for recombination in a-si alloys," *Journal of non-crystalline solids*, vol. 198, pp. 280–283, 1996.